Title: Phanerozoic atmosphere and ocean conditions estimated by a continuous climate and multi-box ocean model

Authors: Alexander J. Krause[a,b*], Mingyu Zhao[c], Andrew S. Merdith[d] and Benjamin J.W. Mills[b]

[a]School of Physical, Chemical and Environmental Sciences, Cardiff University, Main Building, Park Place, Cardiff, CF10 3AT, UK, [b]School of Earth, Environment and Sustainability, University of Leeds, Woodhouse Lane, Leeds, LS2 9JT, UK, [c]State Key Laboratory of Lithospheric and Environmental Coevolution, Institute of Geology and Geophysics, Chinese Academy of Sciences, Beijing 100029, China, [d]School of Physics, Chemistry and Earth Sciences, University of Adelaide, Adelaide, SA, Australia

*Corresponding author: krausea@cardiff.ac.uk

Phanerozoic atmosphere and ocean conditions estimated by a continuous climate and multi-box ocean model

Alexander J. Krause[a,b*], Mingyu Zhao[c], Andrew S. Merdith[d] and Benjamin J.W. Mills[b]

[a]School of Physical, Chemical and Environmental Sciences, Cardiff University, Main Building, Park Place, Cardiff, CF10 3AT, UK

[b]School of Earth, Environment and Sustainability, University of Leeds, Woodhouse Lane, Leeds, LS2 9JT, UK

[c]State Key Laboratory of Lithospheric and Environmental Coevolution, Institute of Geology and Geophysics, Chinese Academy of Sciences, Beijing 100029, China

[d]School of Physics, Chemistry and Earth Sciences, University of Adelaide, Adelaide, SA, Australia

*Corresponding author: krausea@cardiff.ac.uk

Keywords: Phanerozoic, biogeochemistry, modelling, oxygen, pH, climate, carbon

Abstract

The Phanerozoic Eon has witnessed marked fluctuations in Earth's climate and the concentrations of elements conducive to life. Understanding what has driven these changes to the Earth system over such a long timeframe has traditionally used 'box models' which split the Earth into a small number of chemical reservoirs, with many models utilising a single, combined ocean-atmosphere reservoir. This simplification allowed for very efficient long-term computation, but limited the realistic representation of many important processes.

Here, we present AMMONITE: the Atmosphere and Minimal Multi-box Ocean model for Numerical Integration Through Earth history. The model uses an efficient 5-box ocean scheme with a minimal representation of thermohaline circulation, shelf sea processes, carbonate chemistry and productivity-remineralization cycling. We use AMMONITE to replace the single-box atmosphere-ocean in the existing SCION Earth Evolution Model, forming a new biogeochemical model of the Earth

system which can run continuously over Phanerozoic time and dynamically links 3D emulated climate, 2D surface processes and a multi-box ocean. SCION-AMMONITE makes predictions of many facets of the Earth system which will help with understanding habitability over deep time, including a new detailed estimation of the pH and oxygen content of the ocean. In contrast to earlier SCION model outputs, SCION-AMMONITE suggests that O_2 concentrations in the atmosphere and deep ocean were very low in the early Paleozoic, owing to lower predicted sulfate levels, better consideration of the large Precambrian sulfide reservoir, and reduced strength of global oxygen-stabilizing feedbacks as a result of phosphorus limitation in a spatially structured ocean.

1. Introduction

Understanding the chemical evolution of the atmosphere and oceans over geologic timescales is a research area of broad multi- and inter-disciplinary interest (Holland, 1984), and is a key component when it comes to deciphering the 'when and why' of biological evolution and extinction. Much of our knowledge of how the Earth has changed through the Eons comes from the accumulation of geological and geochemical data, which, based upon experimental work and/or on modern-day observations, have become proxy records for key variables such as atmospheric CO_2 and O_2, oceanic SO_4^{2-}, Mg/Ca ratios etc. (see e.g. Lowenstein, Kendall and Anbar, 2014; Foster, Royer and Lunt, 2017; Weldeghebriel *et al.*, 2022; Mills *et al.*, 2023 for various reviews and compilations). However, with questions over the signal primacy captured by the data (vs. alteration by, e.g. the diagenesis of carbonates (Ahm *et al.*, 2018 and refs. therein)), and with some time periods suffering from a paucity of sampling, interpreting Earth system change using proxies alone can be difficult, particularly over long, continuous timescales (tens to hundreds of Myr). Moreover, it is difficult to discern *why* the Earth has changed from environmental data alone.

The advent and proliferation of global biogeochemical modelling over the last five decades, has allowed a greater insight into the coupled evolution of Earth and life, producing predictions of

biogeochemical change over geological timescales, and interrogating the drivers behind such changes. It is not the purpose of this work to delve too deeply into the history of biogeochemical modelling, instead we would direct interested readers to the work of Cosslett-Kemeny *et al.* (2025), who cover this at length. However, a certain amount of background information is necessary to understand the overall rationale of this work. In terms of model operation, this has occurred, in essence, via two different methods: 1) the direct utilisation of proxy data, combined with knowledge of whole Earth system processes, to calculate chemical variables ("inversion" models); and 2) purely process driven ("forwards") models, which can test hypotheses via the generation of synthetic proxy records which can then be compared against empirical data.

Biogeochemical models can also be classified by structural complexity. Because of the computational power and wall-time required (i.e. the real-life time it takes to simulate a modelled interval) there is a sliding scale of intricacy, necessitating a compromise between: 1) 3D simulations, typically run for geologically-short timescales due to their high computational expense; and 2) more computationally efficient (run in minutes on standard desktop PCs), but lower complexity models which can be run dynamically over deep time. The former is typified by the cGENIE model (e.g. Ridgwell and Schmidt, 2010), which can produce spatial maps of Phanerozoic marine conditions when given boundary conditions including overall chemical concentrations, but cannot continuously model how those concentrations might change over millions of years. The latter are typically represented by zero-dimension 'box' models, like COPSE, MAGic, GEOCARBSULF(OR), and others, where chemical fluxes, such as silicate weathering, are estimated at the global scale to give a singular value at each timestep (Hansen and Wallmann, 2003; Bergman, 2004; Berner, 2006a; Arvidson, Mackenzie and Guidry, 2013; Krause *et al.*, 2018; Lenton, Daines and Mills, 2018; Horne and Goldblatt, 2024). In between these two endmembers are various moderate or mixed complexity models such as GEOCLIM (Donnadieu *et al.*, 2004; Ridgwell and Schmidt, 2010; Maffre *et al.*, 2025), the CH2O-CHOO TRAIN model (Kukla *et al.*, 2023), and CANOPS-GRB (Ozaki *et al.*, 2022), which can model aspects of the Earth in higher spatial dimensions (e.g. from a 1D, 2D or 3D perspective), but – as with the cGENIE

model – typically balance this additional computational demand by limiting runs to geologically-short snapshots of time, and then sometimes interpolating between these snapshots. The choice of model to be used for hypothesis testing then, is dependent on a number of factors, including the computing resources available, and the desired spatial vs. temporal resolution of the required outputs.

Because of the long residence and response times involved in the global carbon and oxygen cycles, delineating the evolution of atmospheric O_2 and CO_2 across the entire Phanerozoic has traditionally come from the zero-dimensional box models: COPSE (Bergman, 2004; Lenton, Daines and Mills, 2018) and GEOCARBSULF(OR) (Berner, 2006a; Krause *et al.*, 2018), but with notable contributions from other models such as MAGic (Arvidson, Mackenzie and Guidry, 2006, 2013). However, these models are highly simplified and do not represent, for example, the spatial variability of mountain uplift, surface temperature, precipitation, and thus physical and chemical weathering. In response to this, the Spatial Continuous Integration (SCION) model was developed. SCION combines aspects of COPSE and GEOCLIM – specifically the non-dimensional marine biogeochemistry of COPSE, and the spatially-resolved general climate model (GCM) emulator approach to 2D terrestrial weathering of GEOCLIM (which used runs of the Fast Ocean Atmosphere Model – FOAM). By using a keyframing routine to 'step' the emulated climates through geological time, SCION has enabled a quasi-3D method for modelling the deep-time Earth system, resulting in, in particular, predictions of Phanerozoic atmospheric CO_2 and surface temperature evolution which are more closely aligned to geochemical and lithological proxies than previously achieved (Mills, Donnadieu and Goddéris, 2021; Merdith *et al.*, 2025; Mills *et al.*, 2025).

However, like the COPSE and GEOCARBSULF(OR) box models, a major drawback to SCION continues to be how the atmosphere and ocean are combined into a single reservoir, meaning that atmosphere and ocean chemical concentrations cannot be separated or exchanged, and processes that rely on this exchange, such as oceanic carbonate chemistry and marine anoxia, are therefore not

explicitly represented. Moreover, the lack of a surface and deep ocean means that the processes of productivity and remineralisation, which drive marine biogeochemistry, also cannot be explicitly modelled. This is problematic when considering that a key purpose of models such as SCION is to investigate life evolution and extinction events, many of which are best recorded in the ocean, and are often linked to marine productivity and anoxia.

In this paper we rectify this issue in SCION by developing AMMONITE: the Atmosphere and Minimal Multi-box Ocean model for Numerical Integration Through Earth history. This is a multi-box ocean plus atmosphere system capable of running efficiently over Phanerozoic timescales, which we couple to SCION to replace the single ocean-atmosphere box from COPSE. We largely base AMMONITE on the CHEES model (Zhao *et al.*, 2023; Qiu *et al.*, 2025) but with a number of alterations that enable it to better function over Phanerozoic timescales, as CHEES has not been previously used in this way.

2. Model description

2.1. Model overview and structure

AMMONITE is a 0D biogeochemical model that consists of an atmosphere and a five-box ocean. It is coupled to the large crustal carbon and sulfur reservoirs and the spatially explicit terrestrial processes already present in the SCION model, which rely on a climate emulator generated from previous runs of the FOAM GCM (Figure 1). For the original SCION model the outputs from FOAM included 2D fields of topographic height, runoff, and surface temperature using 21 predetermined paleogeographies and the present-day continental configuration (to cover 540 – 0 Ma) mapped to a 40 x 48 grid, and a wide range of possible atmospheric CO_2 concentrations. This was later then extended into the Neoproterozoic (Mills *et al.*, 2025) and AMMONITE uses this dataset, as incorporating the paleogeography at 580 Ma allows a better representation of conditions at the Ediacaran-Cambrian boundary, although the combined model is not assessed for the Precambrian in this work.

The atmospheric CO_2 calculated from AMMONITE is used in the same way as in the original SCION model, where the model looks at the nearest neighbour (e.g. immediate previous and future timepoints) GCM outputs and bracketed CO_2 values, to run calculations of the 2D terrestrial processes for both timepoints ('double keyframing'). The outputs for both timepoints are summed up across the entire land surface, and interpolation is then used to produce a weighted average for the final bulk flux values. For a more detailed overview of the SCION model structure see Mills *et al*. (2021). The resulting terrestrial outputs (e.g. weathering fluxes) are then delivered to AMMONITE. In this way, AMMONITE directly replaces the previous singular ocean-atmosphere box model in SCION.

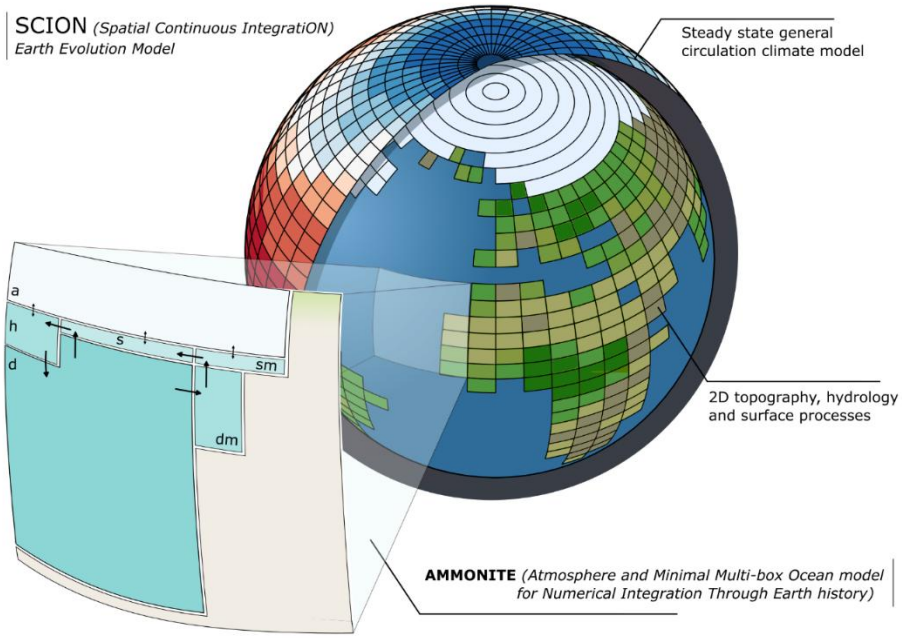

Figure 1 | SCION-AMMONITE model linkage. *AMMONITE replaces the single box atmosphere-ocean biogeochemistry module within the SCION model with a 5-box ocean module and separate atmosphere (a) box. The continental shelf is split into shallow margin (sm) and deep margin (dm) environments, with the open ocean having surface (s), high-latitude (h) and deep (d) regions. Arrows here denote major thermohaline (s-h-d) and coastal upwelling (d-dm-sm) circulation patterns. Bi-directional arrows denote atmosphere-ocean gas transfer.*

The physical architecture of the AMMONITE ocean follows the CHEES model by Zhao *et al.* (2023) which utilised the classic 3-box ocean, 1-box atmosphere model of Sarmiento and Toggweiler (1984). The Sarmiento and Toggweiler model consists of low-latitude surface (s), high-latitude surface (h), and deep (d) ocean boxes, where thermohaline circulation, and bi-directional horizontal and vertical mixing moves dissolved species, such as inorganic carbon (DIC), between the reservoirs. In addition, in Sarmiento and Toggweiler (1984), particulate matter sinks from the surface reservoirs to the deep ocean, and CO_2 is exchanged between the two surface ocean boxes and the atmosphere. Zhao *et al.* (2023) extended this model to include a continental shelf composed of shallow margin (sm) and deep margin (dm) reservoirs. The shallow margin reservoir is connected to the atmosphere and is 100 m in depth, overlying shallow coastal sediments across the global ocean. The deep margin box sits below the shallow margin and is 900 m in depth, encompassing the deeper waters overlying the continental shelves, thus is not directly connected to the atmosphere. We retain the depths of the shallow margin, deep margin, low-latitude surface (100 m) and high-latitude surface (250 m) reservoirs from Zhao *et al.* (2023), however, using corrected ocean surface area and volume data from Costello *et al.* (2015) and reverting back to a high-latitude surface reservoir which covers 15% of the global ocean surface area (Sarmiento and Toggweiler, 1984), we slightly adjust the ocean volume apportioned to each reservoir (see Table 1). In this work, the sizes of the ocean boxes remain fixed throughout the Phanerozoic as there is no bathymetry for the associated FOAM model. Otherwise, the thermohaline circulation (model abbreviation: $f_{Tran\_species\_direction}$), bi-directional vertical mixing ($f_{Mix\_species\_direction}$), and particulate matter sinking ($f_{Sink\_species\_direction}$) operate in the same way as in Zhao *et al.* (2023).

Table 1: The five reservoirs of the ocean and their volumes.

Ocean reservoir name	Model abbreviation	Approximate total modern-day volume (m^3)	Reference
Total ocean	vol_{ocean}	$1.34x10^{18}$	(Sarmiento and Toggweiler, 1984; Toggweiler, 1999; Costello, Smith and Fraczek, 2015; Zhao *et al.*, 2023)
Shallow margin ocean	vol_{sm}	$1.70x10^{15}$	
Deep margin ocean	vol_{dm}	$7.98x10^{15}$	
Low-latitude surface ocean	vol_{s}	$2.66x10^{16}$	
High-latitude surface ocean	vol_{h}	$1.35x10^{16}$	
Deep ocean	vol_{d}	$1.29x10^{18}$	

AMMONITE tracks the major compounds in the coupled elemental cycles of carbon (C), oxygen (O), phosphorus (P), sulfur (S) and iron (Fe) as they cycle through the atmosphere and/or ocean boxes, and also links these cycles to the crustal reservoirs in SCION. Table 2 shows the reservoirs, their model abbreviations and their modern-day sizes in terms of moles. At each timestep in the SCION-AMMONITE model, the molar inventories of each compound in each ocean or atmosphere box are dynamically calculated, with species separation for DIC, particulate organic carbon (POC), dissolved inorganic phosphorus (DIP), particulate organic phosphorus (POP), sulfate, sulfide, Fe(II) and Fe(III). The present-day (e.g. t = 0) concentration for each individual ocean reservoir is calculated using the fractional water volume in that reservoir multiplied by the total molar amount in the global ocean, e.g. for shallow margin sulfate concentrations:

$$[SO_4^{2-}]_{sm\,(0)} = [SO_4^{2-}]_{global\,(0)} * \frac{Volume_{sm}}{Volume_{ocean}} \quad (1)$$

Where the units for concentrations of species are in mol/m^3.

For the amount of dissolved H_2S in the modern ocean, the CHEES model set this to be equal to zero for simplicity (Zhao *et al.*, 2023). We choose instead to set a low but realistic value here. Experimental work has suggested a concentration of 0.51 nM for sulfide species in North Atlantic waters (Cutter and Oatts, 1987) and a range from <0.1 to 1.1 nM in the Western Atlantic (Cutter and Krahforst, 1988). Thus, we use 0.51 nM as a global estimate, considering it sits within the middle of the Western Atlantic range and is equal to that of the North Atlantic. Similarly, CHEES assumed no dissolved Fe(II) is present in the modern ocean. Work in Gran Canaria has shown that some portion of total dissolved Fe is present as Fe(II), with concentrations between 0.13 – 0.63 nM reported on the first measurement day (Hopwood *et al.*, 2020). For AMMONITE we use the highest value of this range, but tempered by the observation that at least 99% of this is complexed by organic ligands which bind Fe (Gledhill and Buck, 2012), thus is not truly dissolved and necessarily available for uptake by organisms. The atmosphere, ocean and sediments evolve through the Phanerozoic subject to the input and output fluxes as described by a large

set of mass balance equations (see Table S3). We now move to providing further information about these fluxes, including how they are derived and the various forcing factors acting upon them, and their present-day sizes. Although many fluxes have been detailed previously in the papers deriving COPSE, SCION and CHEES (Lenton, Daines and Mills, 2018; Mills, Donnadieu and Goddéris, 2021; Zhao *et al.*, 2023), we repeat those which are key to the operation of the model here, for completeness.

Table 2: Chemical reservoirs in the model and their modern-day size.

Reservoir name	Model abbreviation*	Approximate total present-day size	Reference
Atmospheric CO_2	$CO_{2\_a\,(0)}$	5.00×10^{16} mol C	(Dal Corso *et al.*, 2020)
Atmospheric O_2	$O_{2\_a\,(0)}$	3.80×10^{19} mol O	(Berner, 2006a)
Dissolved inorganic carbon	$DIC_{x\,(0)}$	2.80×10^{18} mol C	(Zeebe and Wolf-Gladrow, 2001)
Alkalinity	$ALK_{x\,(0)}$	2.80×10^{18} mol equivalents	Set to be equal to DIC
Dissolved and particulate organic carbon	$POC_{x(0)}$	6.00×10^{16} mol C	$POP_{x\,(0)}$ * 106
Sulfate	$SO_{4\_x\,(0)}$	3.74×10^{19} mol S	(Berner, 1987; Canfield, 2004)
Sulfide	$H_2S_{x\,(0)}$	6.81×10^{11} mol S	(Cutter and Oatts, 1987; Cutter and Krahforst, 1988)
Ocean O_2	$O_{2\_x\,(0)}$	2.30×10^{17} mol O	(Ozaki *et al.*, 2022)
Dissolved phosphorus	$DPhos_{x\,(0)}$	2.84×10^{15} mol P	(Slomp and Van Cappellen, 2007)
Particulate phosphorus	$POP_{x\,(0)}$	5.68×10^{14} mol P	(Slomp and Van Cappellen, 2007)
Iron(III)	$FeIII_{x\,(0)}$	8.30×10^{11} mol Fe	(Tagliabue *et al.*, 2016)
Iron(II)	$FeII_{x\,(0)}$	8.38×10^{9} mol Fe	(Gledhill and Buck, 2012; Hopwood *et al.*, 2020)
Total oceanic nitrate	$N_{(0)}$	4.35×10^{16} mol N	(Lenton, Daines and Mills, 2018)
Sedimentary carbonate carbon	$C_{(0)}$	5.00×10^{21} mol C	(Berner, 1987)
Sedimentary organic carbon	$G_{(0)}$	1.25×10^{21} mol C	(Berner, 1987)
Sedimentary sulfide	$PYR_{(0)}$	1.80×10^{20} mol S	(Lenton, Daines and Mills, 2018)
Sedimentary sulfate	$GYP_{(0)}$	2.00×10^{20} mol S	(Lenton, Daines and Mills, 2018)

*Ocean reservoirs are indicated by $Reservoir_{x\,(0)}$ where the x indicates that within the model the total reservoir size is subdivided into five components represented by the letters in Table 1 and the 0 represents time = 0 (modern-day).

2.2. Nondimensional forcings

As is typically the case for Phanerozoic box models (Berner, 2006a; Arvidson, Mackenzie and Guidry, 2013; Krause *et al.*, 2018; Lenton, Daines and Mills, 2018) a number of dimensionless forcings are used to partially drive model processes (e.g. weathering, degassing, and burial fluxes). Many of these are used directly from SCION (Mills, Donnadieu and Goddéris, 2021). These are BAS_{area} and $GRAN_{area}$, which describe the relative areal extent of exposure of these lithologies to weathering; the timing of the evolution of land plants (*EVO*), and their effect on chemical weathering rates (*W*); and a paleoshoreline (*SHORELINE*) which is used to increase gypsum burial in shallow margin ocean settings as basins become restricted.

Solid-Earth degassing (*D*) is also included where the current degassing rate forcing in SCION (Merdith *et al.*, 2025) combines estimates from continental arcs and rifts, and mid-ocean ridges, based on full-plate reconstructions of seafloor production and consumption, and a full-plate model of the lengths of peri-continental subduction zones. This methodology removed the normalised parameter, *B*, which represents a change in volcanic/metamorphic carbonate breakdown rates due to the evolution of pelagic calcifiers in the mid-Mesozoic, which is thought to have increased the flux of carbonate entering subduction zones (Volk, 1989; Berner, 1991; Merdith *et al.*, 2025) as it estimated it directly (Müller *et al.*, 2022). However, we reinstate this parameter in the carbonate degassing flux to use as an additional modulator of sedimentary carbonate build-up, which is discussed further in Section 4.1. We also reintroduce the COPSE forcing (Lenton *et al.*, 2016; Tostevin and Mills, 2020) of varying terrestrial C:P ratios of buried organic matter (*CPLAND*) because of the simple terrestrial vegetation scheme in SCION?. Finally, because of its importance in regulating the C, S and P cycles (and thus indirectly the O and Fe cycles) we include a normalised (to present-day) forcing of oceanic calcium concentrations (*Calc*). The forcing was created in a previous study (Krause *et al.*, 2024) and is based on reconstructions

of calcium concentrations from fluid inclusions across the Phanerozoic (Weldeghebriel *et al.*, 2022), and we explore this forcing further in Section 4.2.

2.3. Temperatures and iceline

Through coupling to SCION we produce a spatial map of air surface temperature throughout the Phanerozoic. From this we can derive a global average surface temperature (GAST), average air surface temperatures specifically for the equator and tropics, and also average air surface temperatures for low and high-latitude bands (which our low and high-latitude surface ocean boxes are then equal to). We assume that our shallow margin ocean temperature is the same as our low-latitude surface ocean, as during the present day there is a broadly similar length of coastlines across equatorial, low and high-latitude bands, thus this should average out to be somewhat equitable to low-latitude temperatures. We recognise that this should change throughout the Phanerozoic with shifting paleogeographies, and that detailed mapping of this could be assessed in future work. For the deep ocean box, we use the following equation to work out its temperature in °C:

$$T_{d(degC)} = [\max(275.5 + (GAST_{Kelvin} - T_0) * 1.5, 271.15)] - 273.15 \quad (2)$$

For the deep margin ocean box we follow the LOSCAR model (Zeebe, 2012), where the intermediate depth boxes are 1 to 1.5 degrees cooler than the combined average of the low-latitude surface and deep ocean boxes, thus:

$$T_{dm(degC)} = \frac{T_{s(degC)} + T_{d(degC)}}{2} - 1 \quad (3)$$

The continental ice line estimate (extent of ice caps) also follows SCION, which predicts at what latitude the modelled surface temperature of the continent(s) reaches -10°C, i.e. the temperature of the present day ice line (Caldeira and Kasting, 1992; Mills, Donnadieu and Goddéris, 2021).

2.4. Weathering fluxes

2.4.1. Silicate weathering

Silicate weathering rates are unmodified from SCION, which were calculated using relationships derived from work by West (2012) and Maffre *et al.* (2018), with distinct weathering of basaltic and granitic lithologies (Berner, 2006b, 2008; Mills, Daines and Lenton, 2014). Following Merdith *et al.* (2025) the enhanced weathering of silicate minerals in continental arcs and suture zones is also included. The silicate cation denudation per grid cell is calculated as:

$$\omega_{sil} = \varepsilon * \chi_m * \left\{1 - e^{-k_{grain} * f_{kinetic}}\right\} * \left(1 + \omega_{arcs} + \omega_{relict\_arcs} + \omega_{sutures}\right) \quad (4)$$

Where χ_m represents the mass fraction of chemically mobile material lying within the bedrock, k_{grain} is the dependence of weathering on mineral grain size, and ω_{arcs}, ω_{relict_arcs} and $\omega_{sutures}$ are the enhanced weathering of silicates in continental arcs, relict arcs and ophiolitic-bearing suture zones, respectively. The kinetic term, $f_{kinetic}$ is determined via dependencies on local temperature (f_T), runoff (f_Q) and denudation (f_ε) rates, thus:

$$f_{kinetic} = f_T * f_Q * f_\varepsilon \quad (5)$$

Each of these dependencies are calculated as follows:

$$f_T = e^{\left(\frac{E_a}{R*T0} - \frac{E_a}{R*T_{(t)}}\right)} \quad (6)$$

$$f_Q = 1 - e^{-k_{wflow} * Q} \quad (7)$$

$$f_\varepsilon = \frac{\left(\frac{z}{\varepsilon}\right)^{\sigma+1}}{\sigma+1} \quad (8)$$

Where, E_a is the silicate activation energy, R is the gas constant, T is air surface temperature (in °K), k_{wflow} is a constant describing the effect of water flow, z is the depth of the weathering zone, and σ accounts for the effect of time on weathering rates. The erosion rate per grid cell, following West (2012) and Maffre *et al.* (2018), is determined based on, a scaling constant ($k_{erosion}$), the local runoff and temperature, and the topographic slope (*tslope*):

$$\varepsilon = k_{erosion} * Q^{0.31} * tslope * \max(T, 2) \quad (9)$$

A constant parameter ($silw_{scale}$) is then included, to separate the present-day silicate weathering rate ($f_{silw(0)}$) from the spatial scaling conducted:

$$w_{sil\_spatial} = w_{sil\_total} * \frac{f_{silw(0)}}{silw_{scale}} \quad (10)$$

Finally, the basaltic and granitic fractions of silicate weathering are determined thus:

$$\omega_{basw} = \omega_{sil\_spatial} * \left(\frac{k_{basfrac} * BAS_{area}}{k_{basfrac} * BAS_{area} + (1 - k_{basfrac}) * GRAN_{area}}\right) * f_{biota} \quad (11)$$

$$\omega_{granw} = \omega_{sil\_spatial} * \left(\frac{(1 - k_{basfrac}) * GRAN_{area}}{k_{basfrac} * BAS_{area} + (1 - k_{basfrac}) * GRAN_{area}}\right) * f_{biota} \quad (12)$$

Where $k_{basfrac}$ is a constant detailing the fraction of silicate weathering which comes from basalts, and f_{biota} is the biotic enhancement of weathering (see Section 2.7 for further details).

2.4.2. Other weathering fluxes

Carbonate and sulfate (as gypsum) weathering are again unmodified from SCION, where we assume that the key limiting factor on weathering rates is local runoff, as both classes of minerals (sulfates in particular) readily dissolve in the subsurface (Berner, 2006a; Lenton, Daines and Mills, 2018). As with silicates, a constant ($carbw_{scale}$) is used to separate the spatial effect for carbonate weathering, allowing a global flux with the units of mol/yr to be calculated:

$$f_{carbw} = carbw_{scale} * Q * f_{biota} \quad (13)$$

$$f_{gypw} = k_{gypw} * \frac{GYP_{(t)}}{GYP_{(0)}} * \frac{f_{carbw\,(t)}}{k_{carbw}} \quad (14)$$

Where k_{gypw} and k_{carbw} are the present-day gypsum and carbonate weathering flux sizes, respectively.

Although there is some debate as to the sensitivity of pyrite weathering to O_2 levels (e.g. Bergman, 2004; Berner, 2006a; Bolton, Berner and Petsch, 2006; Kanzaki and Kump, 2017), more recent work has shown that under modern day levels pyrite can be oxidised at depths of several metres below the Earth's surface, even in the absence of microbial activity (see Gu *et al.*, 2020 and refs. therein). Instead, as previously indicated (Wildman *et al.*, 2004; Berner, 2006a; Bolton, Berner and Petsch, 2006) and confirmed by more recent work (Gu *et al.*, 2020), under high levels of O_2 the fracture of rocks – such as shales rich in both pyrite and organic matter – via uplift and erosion hold a greater control over pyrite weathering rates. Thus, while SCION has previously assumed, as with carbonates and sulfates, that oxidative and pyrite weathering scales with runoff only, here we modify this relationship to include both erosion and runoff rates, with the inclusion of a dependency on silicate weathering. For pyrite weathering during the Phanerozoic, due to the relatively high levels of O_2, we do not include an O_2-dependent feedback term, but extension of the model back into the Neoproterozoic and beyond will necessitate the inclusion of some relationship between the two variables. However, the correlation between oxidative weathering and O_2 levels appears to be clearer (Daines, Mills and Lenton, 2017) thus we keep the O_2 feedback for this flux.

$$f_{oxidw} = k_{oxidw} * \frac{G_{(t)}}{G_{(0)}} * \left(\frac{O_{2\_a\,(t)}}{O_{2\_a\,(0)}}\right)^{0.5} * \frac{f_{silw\,(t)}}{k_{silw}} \quad (15)$$

$$f_{pyrw} = k_{pyrw} * \frac{PYR_{(t)}}{PYR_{(0)}} * \frac{f_{silw\,(t)}}{k_{silw}} \quad (16)$$

Here, k_{oxidw}, k_{pyrw} and k_{silw} are the present-day flux sizes of oxidative, pyrite, and silicate weathering.

We also keep phosphorus weathering fluxes unchanged from SCION, with fractional contributions (p_{frac}) of phosphorus from the weathering of silicate, carbonate and organic carbon-rich sediments to scale against the present-day flux (k_{phosw}):

$$f_{phosw} = k_{phosw} * \left\{\left(pfrac_{silw} * \frac{f_{silw\,(t)}}{k_{silw}}\right) + \left(pfrac_{carbw} * \frac{f_{carbw\,(t)}}{k_{carbw}}\right) + \left(pfrac_{oxidw} * \frac{f_{oxidw\,(t)}}{k_{oxidw}}\right)\right\} \quad (17)$$

Some of which is retained on land ($k_{landfrac}$) via uptake by the mass of the terrestrial biosphere (*vegetation*):

$$f_{pland} = k_{landfrac} * vegetation * f_{phosw} \quad (18)$$

With the rest entering the ocean:

$$f_{psea} = f_{phosw} - f_{pland} \quad (19)$$

Likewise, we make no changes to the expression for seafloor weathering, which has its own specific activation energy and is dependent on deep ocean temperatures:

$$f_{sfw} = k_{sfw} * D * e^{[E_{a\_sfw} * (T_{d\,(t)} - T_{d\,(0)})]} \quad (20)$$

Finally, we add the weathering of soluble Fe minerals flux from CHEES (Zhao *et al.*, 2023), where, as with pyrite weathering, we assume it broadly scales with the silicate weathering flux.

$$f_{Fe(III)w} = k_{Fe(III)w} * \frac{f_{silw\,(t)}}{k_{silw}} \quad (21)$$

2.5. Degassing and hydrothermal fluxes

Degassing of carbon species and input of other reductants from the mantle are largely unchanged from SCION, but we reintroduce sulfur species degassing into the model for this work. The equations follow broadly the same format, where the constant (k_i) is the present-day flux size for each of organic carbon (f_{ocdeg}), carbonate carbon (f_{ccdeg}), sulfides (f_{pyrdeg}), sulfates (f_{gypdeg}), and reductants ($f_{reductant\_input}$):

$$f_{ocdeg} = k_{ocdeg} * D * \frac{G_{(t)}}{G_{(0)}} \quad (22)$$

$$f_{ccdeg} = k_{ccdeg} * D * \frac{C_{(t)}}{C_{(0)}} * B \quad (23)$$

$$f_{pyrdeg} = k_{pyrdeg} * D * \frac{PYR_{(t)}}{PYR_{(0)}} \quad (24)$$

$$f_{gypdeg} = k_{gypdeg} * D * \frac{GYP_{(t)}}{GYP_{(0)}} \quad (25)$$

$$f_{reductant\_input} = k_{reductant\_input} * D \quad (26)$$

We also include two hydrothermal activity associated fluxes which were not previously considered in SCION. 1) the input of Fe(II) to the ocean which we assume scales with the degassing rate only and was introduced in CHEES (Zhao *et al.*, 2023); and 2) a new flux: the sink of DIP via scavenging on to Fe(III) oxides at both hydrothermal ridge flanks and plumes, which depends on the relative amount of DIP and a Monod constant, which serves to reduce the flux size when O_2 levels in the deep ocean are low (Wallmann *et al.*, 2019):

$$f_{Fe(II)_{hydro}} = k_{Fe(II)\_hydro} * D \quad (27)$$

$$f_{P_{hydro}} = k_{P\_hydro} * D * \frac{DPhos_{d\,(t)}}{DPhos_{d\,(0)}} * \frac{O_{2\,d\,(t)}}{O_{2\,d\,(t)} + Mon_{O2}} \quad (28)$$

For the present-day Fe(II) input flux ($k_{Fe(II)\_hydro}$), Wallmann *et al.* (2019) use a value of 1.35×10^{10} mol/yr, based on work by Tagliabue *et al.* (2014). However, Thompson *et al.* (2019) suggest a substantially larger amount of Fe(II) enters the ocean via hydrothermal activity (10.8×10^{12} mol/yr). Considering the sizes of the other source and sink fluxes, we use a value of 5.5×10^{11} mol/yr, closer to that used by Wallmann *et al.* (2019).

2.6. Dust fluxes

Atmospheric dust is a key source of nutrients to the oceans, with substantial deposition occurring in both margin and open ocean settings, in the process stimulating microbial activity and thus drawing down CO_2 from the ocean-atmosphere system, and supporting food webs (Moore *et al.*, 2013; Westberry *et al.*, 2023). The CHEES model included a source of Fe(III) to the low- and high-latitude

surface ocean, but did not consider aeolian input into shallow margin settings or dust-sourced phosphorus. Hence, in AMMONITE, for both Fe and P, the dust enters the surface ocean (shallow margin, low-latitude, high-latitude), the amount of which is dependent on the estimated pre-industrial flux sizes (Moore *et al.*, 2013; Tagliabue, Aumont and Bopp, 2014) and the surface area fraction of the ocean (Costello, Smith and Fraczek, 2015), e.g. for the shallow margin:

$$f_{Fe\ dust_{sm}} = area_{sm} * k_{Fe\_dust} \quad (29)$$

$$f_{P\ dust_{sm}} = area_{sm} * k_{P\_dust} \quad (30)$$

2.7. Other terrestrial fluxes and associated parameters

We continue SCION's use of the COPSE approach to building global parameters which encapsulate terrestrial biosphere mass (*vegetation*) and its effect on weathering (f_{biota}). While couplings to the deep-time vegetation model, FLORA, have been used with SCION for Mesozoic to present (Gurung *et al.*, 2022, 2024), this has not currently been extended for all of Phanerozoic time, hence the simpler approach used here:

$$f_{biota} = [1 - min(vegetation * W, 1)] * PREPLANT * pCO_2^{0.5} + (vegetation * W) \quad (31)$$

Where *PREPLANT* is a constant which reflects terrestrial weathering by plants as a result of CO_2 fertilisation (Berner and Kothavala, 2001; Lenton, Daines and Mills, 2018). Although the baseline (e.g. single model run) versions of COPSE and SCION set this to have a value of 0.15 based upon the GEOCARB II model (Berner, 1994) we follow GEOCARB III (Berner and Kothavala, 2001) and change this to be 0.25 for the baseline version of AMMONITE, but use the same uncertainty range (1/7 to 1) for the Monte Carlo ensemble runs (see Section 2.14.) as SCION.

For determining the biosphere mass, *vegetation*, a product of productivity and wildfire forcings is used:

$$vegetation = V_{npp} * firef \quad (32)$$

The *firef* term represents the effect of wildfires as a feedback on terrestrial biomass, including the involvement of the mixing ratio of atmospheric O_2 (mrO_2) on fire ignition (*ignit*):

$$firef = \frac{k_{fire}}{k_{fire} - 1 + ignit} \quad (33)$$

$$ignit = min[max(48 * mrO_2 - 9.08, 0), 5] \quad (34)$$

$$mrO_2 = \frac{\left(\frac{O_{2\_a(t)}}{O_{2\_a(0)}}\right)}{\left[\left(\frac{O_{2\_a(t)}}{O_{2\_a(0)}}\right) + 3.762\right]} \quad (35)$$

While, the V_{npp} term describes the cumulative effect on terrestrial net primary productivity from the global average surface temperature (GAST), and atmospheric O_2 and CO_2 levels:

$$V_{npp} = k_{npp\_terrestrial} * EVO * Veg_{temp} * Veg_{O2} * Veg_{CO2} \quad (36)$$

$$Veg_{temp} = 1 - \left(\frac{GAST_{degC} - 25}{25}\right)^2 \quad (37)$$

$$Veg_{O2} = 1.5 - \left(0.5 * \frac{O_{2\_a(t)}}{O_{2\_a(0)}}\right) \quad (38)$$

$$Veg_{CO2} = \frac{CO_{2\_a\,(ppm)} - CO_{2\,pp\_min}}{CO_{2\,pp\_half} + CO_{2\_a\,(ppm)} - CO_{2\,pp\_min}} \quad (39)$$

Including constants for: net primary productivity ($k_{npp\_terrestrial}$), the minimum CO_2 level for primary productivity to occur ($CO_{2\,pp\_min}$), and the level of CO_2 at which primary productivity halves ($CO_{2\,pp\_half}$). As detailed in Section 2.4.2., the *vegetation* term is key for determining the amount of P retained on land (f_{pland}), which then feeds directly into estimating terrestrial organic carbon burial via scaling to the modern-day rate (k_{locb}):

$$f_{locb} = k_{locb} * \frac{f_{pland\,(t)}}{f_{pland\,(0)}} * CPLAND \quad (40)$$

406 The final terrestrially-related flux used from SCION is the burial of calcium sulfate minerals
407 (as gypsum) as ocean waters become trapped in, and evaporated from, basins as they close:

408 $$f_{gypb} = k_{gypb} * \frac{SO_{4\_sm\,(t)}}{SO_{4\_sm\,(0)}} * \frac{1}{SHORELINE} * Calc \quad (41)$$

409 The flux is dependent on the modern-day flux size, the normalised to present day amount of sulfate in
410 the shallow margin ocean box, a reconstruction of shoreline length based on information from a digital
411 elevation model (Mills, Donnadieu and Goddéris, 2021), and the normalised amount of calcium in the
412 ocean.

413

414 2.8. The carbonate system

415 *2.8.1. Overview*

416 CO_2 in the atmosphere readily dissolves in seawater. When it does it becomes an aqueous
417 version of itself ($CO_{2(aq)}$), before then reacting with the water to form carbonic acid (H_2CO_3), after which
418 it can then undergo a series of dissociation reactions to generate bicarbonate (HCO_3^-) and carbonate
419 (CO_3^{2-}) ions, as well as 'free' protons (Zeebe and Wolf-Gladrow, 2001). As H_2CO_3 concentrations are
420 small and hard to distinguish chemically from $CO_{2(aq)}$ these two parameters are added together and often
421 denoted as either $CO_{2(aq)}^*$ or $H_2CO_3^*$ and sometimes as CO_{2T} (Zeebe and Wolf-Gladrow, 2001; Dickson,
422 2010). The sum of all our carbon-associated species in the ocean makes up DIC, and the ionic charges
423 are kept track of by the carbonate alkalinity (Zeebe and Wolf-Gladrow, 2001). Thus, we have our
424 atmosphere-ocean carbon system, where the concentrations of each species at any point in time are
425 partially dependent on pH, temperature and salinity, and if two out of six parameters are known, the
426 whole system can be calculated.

427 The system, then, can be expressed as a series of equilibrium relationships (Zeebe and Wolf-Gladrow,
428 2001; Dickson, 2010):

429 $$k_0 = \frac{\left[CO_{2\,(aq)}^*\right]}{CO_{2\,(g)}} \quad (42)$$

$$k_1 = \frac{[H^+] * [HCO_3^-]}{\left[CO^*_{2\,(aq)}\right]} \quad (43)$$

$$k_2 = \frac{[H^+] * [CO_3^{2-}]}{[HCO_3^-]} \quad (44)$$

$$k_B = \frac{[H^+] * [B(OH)_4^-]}{[B(OH)_3]} \quad (45)$$

$$k_w = [H^+] * [OH^-] \quad (46)$$

Where equations 45 and 46 represent the dissociation of boric acid and the self-ionisation of water, respectively, but are not included in this work. The constant, k_0 represents Henry's Law, and is sometimes denoted as k_H.

2.8.2. Determining AMMONITE's carbonate species

The CHEES ocean biogeochemical model (Zhao *et al.*, 2023) contains equations, using the above principles, to derive carbonate-associated parameters based upon the work by Walker and Kasting (1992). While this approach works well, it is a *relatively* simple approximation of a highly complex system. As such, we take the opportunity to refine the representation of the carbonate system in AMMONITE by incorporating many elements of the 'csys' model (Zeebe and Wolf-Gladrow, 2001). There are a large number of equations and constants involved in defining the carbonate system in this work, as many of the equations are lengthy and require to be broken down for clarity. Thus, in this section we provide a general overview of the equations and constants, and what we have done, with the full equations and constants listed in Tables S1 and S2.

Historically, there have been four different scales used for determining seawater pH: the NBS (now the IUPAC) scale; the 'free' hydrogen ion scale; the seawater scale, and the 'total' hydrogen ion scale, each with a different set of constant parameters, attuned to various temperatures and salinities, which are used to calculate pH (Dickson, 1984, 2010; Zeebe and Wolf-Gladrow, 2001). This resulted

in variances in pH readings of the same medium prior to the early 1990's, after which the total hydrogen scale was determined to be the most appropriate scale for the temperatures and salinities encountered in the ocean (Dickson, 1993). Further, the total scale includes not only 'free' protons – i.e. those which bond to a water molecule (forming H_3O^+) before undergoing further hydrogen bonding to form $H_9O_4^+$ – but also those associated with other ions, such as sulfate and fluoride (Dickson, 1984, 1993). However, that is not to say that the other scales are unimportant and do not have their uses in chemical oceanography. Indeed, the IUPAC scale is more suitable for measuring the pH of extracellular fluids of marine vertebrates (Dickson, 2010), but importantly for this work, even though the total scale is used, pressure-related corrections to k_1 and k_2 have only been derived in the csys model for other pH scales, thus some back and forth conversion between the scales needs to take place to allow for these pressure corrections for the deep margin and deep ocean boxes (Zeebe and Wolf-Gladrow, 2001).

In AMMONITE, we calculate k_0, k_1 and k_2 explicitly, using model-derived temperatures and the constant values by Mehrbach *et al.* (1973) – which were originally expressed on the IUPAC scale – reformulated by Lueker *et al.* (2000) to the total scale. For the ocean boxes connected to the atmosphere we assume, for simplicity, that the pressure is equal to the atmosphere at sea level (e.g. 1 atm) but for the deep margin and deep ocean boxes we assume that pressures are equivalent to their lowest depths and thus are 100 atm and 400 atm respectively (Broecker and Peng, 1982). The pressure in each box could be calculated using an average of the height of the box (e.g. an average of 1–25 atm for the high-latitude surface ocean), but this will be explored in future work which also examines the effect of changing eustasy on the carbonate system. The k_1 and k_2 constants are calculated for all five ocean boxes, and the solubility product constants (K_{spc} and K_{spa}) for the three sediment-connected boxes, all at 1 atm on the total scale. For the deep margin and deep boxes, the sulfate and fluoride dissociation constants are determined and used to help convert k_1 and k_2 from the total to seawater pH scale (Millero, 2010). Pressure corrections are applied, and then the constants are converted back to the total pH scale. The solubility product constants are corrected for pressure but do not require pH scale conversions for this. We use the k_1 and k_2 values, alongside our model calculated [DIC] and [ALK], to ascertain [HCO_3^-

480] in each ocean box (Walker and Kasting, 1992). The [ALK] and [HCO_3^-] are then used to find [CO_3^{2-}];
481 while [HCO_3^-], [CO_3^{2-}] and k_2 help us to determine [H^+] and subsequently pH levels (see Table S1).

482

483 *2.8.3. Air-sea gas exchange of CO_2*

484 With all other carbonate system species derived, we can calculate the $CO_{2\,(aq)}^*$ variable, using
485 [ALK], [H^+], k_1 and k_2. The [$CO_{2\,(aq)}^*$] then needs to be converted to CO_2 fugacity (pCO_2), via the use
486 of k_0, before we can work out the air-sea gas exchange of the surficial ocean boxes. The air-sea gas
487 exchange (in mol/yr) is dependent on the timescale for this flux (τ, approximately 10 years), the
488 fractional surface area of each ocean box, the present-day flux size, and the difference between pCO_2
489 in the atmosphere and ocean.

490

491 *2.8.4. Carbonate burial*

492 The ultimate sink for atmospheric CO_2 over geologic timescales is the burial of marine
493 carbonates, with this process closing the silicate-carbonate cycle (Walker, Hays and Kasting, 1981).
494 With all other aspects of the carbonate system introduced, we can finally determine how much carbon
495 is removed from the ocean and as which polymorph of $CaCO_3$ (either calcite or aragonite). For each
496 polymorph of $CaCO_3$ the saturation state (Ω) in each box is computed using the concentration of Ca in
497 the ocean ([Ca^{2+}]$_{sw}$), [CO_3^{2-}], and the solubility products. While for the CHEES model the only free
498 variable was [CO_3^{2-}] (Zhao *et al.*, 2023), in AMMONITE all three variables change through time, with
499 [CO_3^{2-}] and the solubility products calculated explicitly by the model and the [Ca^{2+}]$_{sw}$ imposed upon it
500 via the *Calc* forcing. A generalised equation for carbonate precipitation has been used extensively in
501 the literature (Burton and Walter, 1987; Caldeira and Rampino, 1993; Opdyke and Wilkinson, 1993;
502 Zeebe and Westbroek, 2003; Rampino and Caldeira, 2005):

503 $$F_{carb} = k(\Omega - 1)^{\eta} \quad (47)$$

Where: k is a precipitation rate constant; and η is the order of reaction, with values between 1.7 – 2 often used. Both the CARMER (Dal Corso *et al.*, 2020) and CHEES (Zhao *et al.*, 2023) models modified this equation such that the saturation state was normalised against the present-day saturation, and the precipitation rate constant was replaced with the present-day carbonate burial rate, allowing the calculation of a burial flux with the desired units (mol/yr):

$$f_{mccb} = k_{mccb} * \frac{(\Omega_{(t)}-1)^{\eta}}{\Omega_{(0)}} \quad (48)$$

Where η = 1.7. Previous modelling has used a constant value for η (Caldeira and Rampino, 1993; Zeebe and Westbroek, 2003; Rampino and Caldeira, 2005; Dal Corso *et al.*, 2020; Zhao *et al.*, 2023), however, this is a kinetic parameter, and experimental work has shown that its value is temperature-dependent and varies on whether calcite or aragonite is the precipitating polymorph (Burton and Walter, 1987). As such, we use the data points for η and temperature in Table 1 in Burton and Walter (1987) to develop equations (linear for aragonite, polynomial for calcite) which allow us to find η for any temperature:

$$\eta_{calc\,(t)} = \left[-0.001 * \left(T_{x\,(\mathrm{degC})}\right)^2\right] + \left[0.0947 * T_{x\,(\mathrm{degC})}\right] + 0.1513 \quad (49)$$

$$\eta_{arag\,(t)} = \left[0.0628 * T_{x\,(\mathrm{degC})}\right] + 0.0985 \quad (50)$$

Where $T_{x\,(degC)}$ is the temperature of the relevant ocean box in °C.

Both the CARMER and CHEES models used a constant value for the present-day $CaCO_3$ saturation state of the ocean (Dal Corso *et al.*, 2020; Zhao *et al.*, 2023). However, the saturation state varies with latitude, longitude and with depth, and is different for calcite and aragonite (Feely *et al.*, 2004; Gehlen *et al.*, 2007; Fabry *et al.*, 2008; Friedrich *et al.*, 2012; Hoegh-Guldberg *et al.*, 2017). Previous works, which estimate calcite and/or aragonite saturation values for the pre-industrial/present-day ocean, do so using data observations of other carbonate system parameters and/or biogeochemical models, meaning that the overall spatial patterns of saturation are similar but there is some variance between reported values. For example, Friedrich *et al.* (2012) model for the pre-industrial years, 800–

1750, the average surface Ω_{arag}, finding that the saturation values in the tropics are generally >3.5 and this declines to 1.5 in the higher latitudes, apart from patches in the Arctic ocean, where $\Omega_{arag} = 1$ (see their supplementary figure 1). While, using a different model, Hoegh-Guldberg *et al.* (2017) estimate a slightly greater areal extent of the surface ocean where Ω_{arag} is at, or below, saturation. We combine a number of data and model maps to use estimates of $\Omega_{arag(0)}$ and $\Omega_{calc(0)}$ for AMMONITE (Feely *et al.*, 2004; Gehlen *et al.*, 2007; Fabry *et al.*, 2008; Friedrich *et al.*, 2012; Hoegh-Guldberg *et al.*, 2017), but acknowledge that future work could involve refining these numbers. As we only need saturation values for the shallow margin, deep margin and deep ocean boxes in order to calculate carbonate burial, we do not worry about $\Omega_{arag(0)}$ and $\Omega_{calc(0)}$ for the low- and high-latitude surface boxes.

We switch between burying solely calcite or aragonite using approximate geological ages for calcitic and aragonitic seas (Lowenstein, Kendall and Anbar, 2014), linearly interpolating between the timepoints. Future work could look at burying both, but in different proportions depending on seawater magnesium concentrations, and changing ocean temperatures and pressures (i.e. due to climate/tectonic changes to eustasy and isostasy). Finally, equation 48 represents total global marine carbonate burial, thus CHEES introduced an additional scaling term which separates the global flux into that which is buried: on shallow margin continental shelves (70% of total f_{mccb}); deep margin continental shelves (20%); and in deep ocean sediments (10%), which we retain in AMMONITE.

2.9. Primary production, remineralisation, and burial of particulate organic matter

2.9.1. Overview

In AMMONITE we use the productivity and remineralisation scheme from CHEES (Zhao *et al.*, 2023) with some modifications. Primary producers in the shallow margin, low- and high-latitude ocean boxes create particulate organic carbon (POC), in the process depleting the DIC pool, and generate as a by-product, O_2. As the primary producers die, the POC sinks through the water column, and in all ocean boxes undergoes a chain of remineralisation reactions: aerobic respiration; iron

554 reduction; and sulfate reduction – for simplicity nitrate and manganese reduction were not considered.
555 In each reaction the POC is the electron donor, and O_2, Fe(III), and SO_4^{2-} are the electron acceptors
556 respectively. It is estimated that approximately 80% of all POC produced is remineralised in the surficial
557 ocean, with another ~15% remineralised at greater depths, leaving only ~5% reaching the sediments
558 (Middelburg, 2019). However, only a small fraction of the organic carbon which makes it into the
559 sediments is locked away for geologically long timescales, instead most is degraded further, dependent
560 on the depositional environment and the nature of the organic carbon (Curtis, 1977; Emerson and
561 Hedges, 1988; Chen *et al.*, 2022). For our model we assume that all of the DIC produced from sediment
562 remineralisation diffuses back into the ocean, although in reality, some of this DIC will go towards the
563 formation of authigenic carbonates (Irwin, Curtis and Coleman, 1977). At the same time, primary
564 producers generate particulate organic phosphorus compounds (POP), for which we assume that: the
565 ratio of POC:POP created is equal to the Redfield ratio of 106:1 (Redfield, 1958); and the compounds
566 are subject to the same remineralisation processes and stoichiometry as POC in the ocean and marine
567 sediments, with only a small amount of POP escaping complete degradation.

568

569 *2.9.2. Primary production*

570 POC created through primary production is calculated as follows:

571 $$POC_{primprod_x} = k_{pp\_x} * NPP_{temp\_x} * Monod_{PO4\_x} \quad (51)$$

572 We use the present-day rate (k_{pp_x}) for each surficial ocean box, the influence of temperature on primary
573 producers (NPP_{temp_x}) and a Monod-related term ($Monod_{PO4\_x}$) linked to phosphate levels. The effect of
574 temperature on primary productivity was not included in CHEES, and we use the functional form used
575 in iterations of the cGENIE model (Reinhard *et al.*, 2020; Van De Velde *et al.*, 2021):

576 $$NPP_{temp\_x} = kt_{scale} * e^{\left(\frac{T_{x\,(\mathrm{deg})}}{temp_{biota}}\right)} \quad (52)$$

577 Where kt_{scale} is a scaling constant, and $temp_{biota}$ is an e-folding temperature for biological rates (i.e. the
578 temperature by which rates change as a factor of Euler's number). The effect of the scaling constant and

579 e-folding temperature is to provide an approximate doubling in primary productivity per 10°C increase
580 (from temperature increases alone, e.g. Q_{10} = ~2) (Reinhard *et al.*, 2020; Van De Velde *et al.*, 2021).
581 We retain this and still observe the Q_{10} rule, but we use a lower e-folding temperature (15.65°C instead
582 of 15.8°C) based on other work (Schmittner *et al.*, 2008; Wallmann *et al.*, 2019) and subsequently
583 calculate a different scaling constant for use in AMMONITE.

584

585 Phosphate is generally considered to be the principal limiting nutrient for primary productivity
586 over geologic timescales (Tyrrell, 1999), and thus we assume the availability of DIP serves as a control
587 on POC rates. While CHEES used a co-limitation of P and Fe to control primary productivity (Zhao *et*
588 *al.*, 2023), we only use DIP concentrations because the residence time of Fe in the ocean is often shorter
589 than ocean circulation times (Black *et al.*, 2020) and concentrations are far more spatially heterogeneous
590 than our model can easily resolve, meaning that background conditions far from present-day could
591 cause inconsistencies with co-limitation in the CHEES model, thus we assume:

592 $$Monod_{PO4\_x} = DPhos_{conc\_x} * \frac{DPhos_{conc\_x}}{DPhos_{conc\_x} + Mon_{P\_pp}} \quad (53)$$

593 Where $DPhos_{conc\_x}$ is the concentration of dissolved inorganic P in the relevant ocean box, and Mon_{P_pp}
594 is the actual Monod (half-saturation) constant for P as used in primary productivity.

595

596 For the Monod constant, previous studies have used a wide range of values, e.g.: $1x10^{-5}$ mol/m^3
597 (Wallmann *et al.*, 2019); $1x10^{-4}$ mol/m^3 (Van De Velde *et al.*, 2021); $1x10^{-6}$ mol/m^3 (Ozaki *et al.*, 2022);
598 $1x10^{-7}$ mol/m^3 (Archer and Johnson, 2000); $5x10^{-4}$ mol/m^3 (Parekh, Follows and Boyle, 2005). A
599 compilation of P half-saturation constants for different phytoplankton groups suggests a range from
600 $1.3x10^{-5}$ mol/m^3 to $5.24x10^{-3}$ mol/m^3 (Munkes, Löptien and Dietze, 2021). Eukaryotic microalgae
601 dominate the modern ocean, but in deep time prokaryotic cyanobacteria would have been the major
602 contributors to primary production (Parker, Mock and Armbrust, 2008), as such, and ignoring the half-
603 saturations of diatoms and dinoflagellates, we average those of the microalgae and cyanobacteria

(Munkes, Löptien and Dietze, 2021) to produce the value of 1.9×10^{-3} mol/m^3 which we use in AMMONITE. We divide the primary production of POC: a) by the Redfield ratio to estimate POP production; and b) by the C:O_2 ratio (106:138) to estimate the amount of O_2 generated (Redfield, 1958):

$$POP_{primprod_x} = \frac{POC_{primprod_x}}{Red_{C:P}} \quad (54)$$

$$O_{2\_primprod_x} = \frac{POC_{primprod_x}}{Red_{C:O_2}} \quad (55)$$

2.9.3. Water column remineralisation

We use the nomenclature, 'remineralisation' in this work to mean all processes which lead to the degradation of organic matter, albeit much of its breakdown, particularly within the water column, is via aerobic respiration conducted by various organisms (Emerson and Hedges, 2008). As with the CHEES model, the processing of organic matter within the water column follows a sequence controlled by energy yields, and is calculated using a Monod scheme (Froelich *et al.*, 1979; Reed, Slomp and Gustafsson, 2011; Zhao *et al.*, 2023). We start with aerobic remineralisation, which is followed by iron reduction and then sulfate reduction:

$$AR_x = k_{POCwr\_x} * \frac{POC_{x\,(t)}}{POC_{x\,(0)}} * \left(\frac{O_{2\ conc\_x\,(t)}}{O_{2\ conc\_x\,(t)} + Mon_{O2}}\right) \quad (56)$$

Here, k_{POCwr_x} is the present-day remineralisation rate of POC, and is multiplied by the normalised amount of POC, and the concentration of O_2 subject to a Monod constant, in each ocean box.

$$ironR_x = k_{POCwr\_x} * \frac{POC_{x\,(t)}}{POC_{x\,(0)}} * \left(\frac{Mon_{O2}}{O_{2\ conc\_x\,(t)} + Mon_{O2}}\right) * \left(\frac{Fe(III)_{conc\_x\,(t)}}{Fe(III)_{conc\_x\,(t)} + Mon_{Fe(III)_{resp}}}\right) \quad (57)$$

$$sulfR_x = k_{POCwr\_x} * \frac{POC_{x\,(t)}}{POC_{x\,(0)}} * \left(\frac{Mon_{O2}}{O_{2\ conc\_x\,(t)} + Mon_{O2}}\right) * \left(\frac{Mon_{Fe(III)_{resp}}}{Fe(III)_{conc\_x\,(t)} + Mon_{Fe(III)_{resp}}}\right) * k_{\Psi} * \left(\frac{SO_{4\ conc\_x\,(t)}}{SO_{4\ conc\_x\,(t)} + Mon_{SO4_{resp}}}\right) \quad (58)$$

Iron and sulfate reduction complement the aerobic respiration flux with sequential additions of Fe(III) and sulfate concentrations respectively, such that organic matter not consumed by the first is available for subsequent processes. There is also a multiplication constant (k_{Ψ}) to attenuate sulfate reduction, which takes into account that organic matter remineralisation via this pathway is slower than via aerobic respiration and iron reduction (Reed, Slomp and Gustafsson, 2011). While CHEES set the attenuation factor to be equal to 0.2 (Zhao *et al.*, 2023), in AMMONITE we revert back to 0.075 (Reed, Slomp and Gustafsson, 2011). The reasoning behind this is that the model used by Reed *et al.* (2011) explicitly separated organic matter into three pools (highly reactive, less reactive and non-reactive) whereas AMMONITE does not, but due to the redox order in operation, aerobic respiration and iron reduction will use more of the highly reactive phase of organic matter, leaving more recalcitrant materials for sulfate reduction. The total amount of water column remineralisation for POC, and subsequently POP then, is:

$$POC_{wr\_x} = AR_x + ironR_x + sulfR_x \quad (59)$$

$$POP_{wr\_x} = \frac{POC_{wr\_x}}{Red_{CP}} \quad (60)$$

2.9.4. Burial and sediment remineralisation

The amount of POC in each of the shallow margin, deep margin and deep ocean boxes helps to determine the size of the export flux of organic carbon from the water column to the underlying sediments, and consequently the POP export flux:

$$C_{watsed\ export\_x} = k_{watsed\_x} * \frac{POC_{x\,(t)}}{POC_{x\,(0)}} \quad (61)$$

$$P_{watsed\ export\_x} = \frac{C_{watsed\ export\_x}}{Red_{CP}} \quad (62)$$

Where k_{watsed_x} is the present-day export of POC and is calculated using a mass balance approach, i.e., that the water-sediment flux equals primary production minus water column remineralisation. There is some uncertainty regarding the absolute amount of POC locked away, escaping microbial degradation,

as this process can continue in very deep and ancient marine sediments (Hedges and Keil, 1995; Lenton, Daines and Mills, 2018; LaRowe *et al.*, 2020; Bradley *et al.*, 2022). For AMMONITE we retain the upper limit ($4.5x10^{12}$ mol/yr) for organic carbon burial used in the SCION model (Lenton, Daines and Mills, 2018; Mills, Donnadieu and Goddéris, 2021) and apportion 45% of this as being buried in shallow margin sediments (Hedges and Keil, 1995), with 35% in deep margin and 20% in deep sediments (Berner, 1982). Total marine-derived organic carbon burial is lower than in the CHEES model, but AMMONITE includes the simplified representation of terrestrially-derived organic carbon burial from SCION to counterbalance this. We use the present-day POC burial and water-sediment export rates to calculate a burial efficiency:

$$CBE_x = \frac{f_{mocb\_x\,(0)}}{C_{watsed\ export\_x\,(0)}} \quad (63)$$

We assume here, for simplicity, that the burial efficiency for the present-day holds for the rest of the Phanerozoic, such that we can re-arrange equation 63 to find f_{mocb_x} for time (t). The total amount of POC buried in marine sediments, f_{mocb_total}, is then the summation of that which occurs in the shallow margin, deep margin and deep sediments. Again, POP burial (f_{POPb_x}) is f_{mocb_x} divided by the Redfield ratio.

The POC which is not buried is degraded in the sediments and the carbon is returned to the overlying water column as a benthic flux of DIC:

$$DICbenthic_x = C_{watsed\ export\_x} - f_{mocb\_x} \quad (64)$$

And is the product of a series of reactions where the functional forms of the electron acceptors are similar to those seen in the water column, such that the oxygen consumed during aerobic respiration in the sediments is:

$$O_{2\ benthic\_x} = \frac{C_{watsed\ export\_x} - f_{mocb\_x}}{Red_{CO}} * \left(\frac{O_{2\ conc\_x\,(t)}}{O_{2\ conc\_x\,(t)} + Mon_{O2}}\right) \quad (65)$$

And the amount of Fe(III) and sulfate being reduced to Fe(II) and sulfide, respectively, is calculated thus:

$$Fe(III)_{benthic\_x} = \frac{C_{watsed\ export\_x} - f_{mocb\_x}}{Red_{CO}} * \left(\frac{Mon_{O2}}{O_{2\ conc_x(t)} + Mon_{O2}}\right) * \left(\frac{Fe(III)_{conc\_x\,(t)}}{Fe(III)_{conc\_x\,(t)} + Mon_{Fe(III)resp}}\right) \quad (66)$$

$$sulfate_{benthic\_x} = \frac{C_{watsed\ export\_x} - f_{mocb\_x}}{Red_{CO}} * \left(\frac{Mon_{O2}}{O_{2\ conc_x(t)} + Mon_{O2}}\right) * \left(\frac{Mon_{Fe(III)resp}}{Fe(III)_{conc_x(t)} + Mon_{Fe(III)resp}}\right) * k_{\Psi} * \left(\frac{SO_{4\ conc\_x\,(t)}}{SO_{4\ conc\_x\,(t)} + Mon_{SO4resp}}\right) \quad (67)$$

In the CHEES model, no attenuation factor was included in the equation for sulfate reduction in the sediments (Zhao *et al.*, 2023). However, as with water column sulfate reduction, Reed *et al.* (2011) include this factor for sediment sulfate reduction and also for sediment methanogenesis, using the same value for k_{Ψ} for both processes as for water column sulfate reduction. And so for this work we decide to include it in both equations too. Methanogenesis does not create DIC but does create an additional sink for oceanic O_2. Our equation for methanogenesis is:

$$methanogenesis_{benthic\_x} = \frac{C_{watsed\ export\_x} - f_{mocb\_x}}{Red_{CO}} * \left(\frac{Mon_{O2}}{O_{2\ conc_x(t)} + Mon_{O2}}\right) * \left(\frac{Mon_{Fe(III)resp}}{Fe(III)_{conc_x(t)} + Mon_{Fe(III)resp}}\right) * k_{\Psi} * \left(\frac{Mon_{SO4inhib}}{SO_{4\ conc\_x\,(t)} + Mon_{SO4inhib}}\right) \quad (68)$$

Where $Mon_{SO4inhib}$ is a inhibition constant for dissimilatory sulfate reduction (Ridgwell *et al.*, 2007).

In terms of the benthic fluxes of P, which represents conversion of particulate organic P (POP) back into the dissolved inorganic form (DIP), not all of the DIP diffuses from the sediment back into the overlying water column. Instead, some DIP reacts with elements such as calcium to form authigenic minerals (e.g. apatite), and some sorbs to Fe (oxy)hydroxides (Froelich *et al.*, 1982), and are then subsequently buried. For AMMONITE, for now, we assume simple relationships for authigenic P

formation and Fe-P sorption, based on the modern-day burial rates and multiplied by the normalised DIP concentrations in the overlying water column, as we do not explicitly model fluxes within marine sediments:

$$P_{auth\_x} = k_{Pauth\_x} * \frac{DPhos_{x\,(t)}}{DPhos_{x\,(0)}} \quad (69)$$

$$P_{Fe\_x} = k_{PFe\_x} * \frac{DPhos_{x\,(t)}}{DPhos_{x\,(0)}} \quad (70)$$

The benthic P flux then, can be defined thus:

$$P_{benthic\_x} = P_{watsed\ export\_x} - f_{POPb_x} - P_{auth\_x} - P_{Fe\_x} \quad (71)$$

2.10. Iron mineral reactions

The model includes a number of processes which alter the quantity of various Fe minerals in the ocean boxes, depending on the concentrations of the different phases of Fe and S as governed by changes to redox. Chief among these processes is the formation of pyrite minerals, both within the water column and within the sediments. In the water column, we follow the CHEES model, where the rate of pyrite formation in any box is linked to a kinetic constant (k_{py}), the concentration of Fe(II) and sulfide, a thermodynamic equilibrium constant ($Ksp_{FeS(aq)}$) and a parameter ($ST_{FeS(aq)}$) which describes a solubility threshold beyond which some portion of aqueous FeS will precipitate out of solution and then react with more sulfides to form pyrite:

$$water_{pyF\_x} = k_{py} * max\left[\left(\frac{Fe(II)_{conc_x} * H_2S_{conc_x}}{Ksp_{FeS(aq)}} - ST_{FeS(aq)}\right), 0\right] * H_2S_{conc_x} * vol_x \quad (72)$$

The CHEES model estimated sedimentary sulfate reduction rates, albeit it did not incorporate the long-term effects of pyrite formation in the sediments on the oxygen cycle. As this early diagenetic process is an important component of the longer-term Earth system (Berner, 1984; Mertens, Paradis and Hemingway, 2026) and is a major process in SCION, we include sedimentary pyrite formation in

AMMONITE and its impact on O_2 concentrations. The amount of pyrite formed is related to the normalised-to-present benthic fluxes involving Fe(III) and sulfate, which are utilising organic carbon as an electron donor to become reduced to Fe(II) and H_2S in the sediments and the modern-day rate of formation:

$$seds_{pyF\_x} = k_{pyrb\_x} * \frac{Fe(III)_{benthic\_x\,(t)} * 2 * sulfate_{benthic\_x\,(t)}}{Fe(III)_{benthic\_x\,(0)} * 2 * sulfate_{benthic\_x\,(0)}} \quad (73)$$

Total pyrite burial (f_{pyrb_total}) is equal to the sum of pyrite formation occurring in the water column from all ocean boxes and in the sediments (which as noted earlier, are not an explicit reservoir).

In oxic waters, Fe(III) can be generated via the aerobic oxidation of Fe(II) species (Wang and Van Cappellen, 1996), while in anoxic waters, sulfide can assist in the reduction of Fe(III) back to Fe(II) (Poulton, 2003). For these two reactions we utilise the same representation as in CHEES, where they are contingent on the reaction rate constants and the concentration of the respective Fe species, then either the O_2 or the sulfide concentration in the relevant ocean box:

$$ironO_x = max\left[\left(k_{ironO} * Fe(II)_{conc_x} * O_{2conc_x} * vol_x\right), 0\right] \quad (74)$$

$$SironR_x = max\left[\left(k_{SironR} * H_2S_{conc_x} * Fe(III)_{conc_x} * vol_x\right), 0\right] \quad (75)$$

As with the CHEES model, we include the removal of Fe(III) in oxic waters via scavenging by particulate organic matter and ligands. The removal rate is determined by a kinetic constant for scavenging multiplied by the normalised POC concentration, which is then multiplied by the concentration of Fe(III) minus a ligand constant (Lefèvre and Watson, 1999; Parekh, Follows and Boyle, 2005; Tagliabue *et al.*, 2016; Zhao *et al.*, 2023):

$$Fe_{scav\_x} = max\left[\left\{\left(k_{Fe\_scav\_x} * \frac{POC_{x\,(t)}}{POC_{x\,(0)}}\right) * \left(Fe(III)_{conc\_x} - k_{Fe\_ligand}\right)\right\}, 0\right] \quad (76)$$

Finally, siderite can be an important sink of Fe in the ocean, with it being a common component of iron formations in the Precambrian (Ohmoto, Watanabe and Kumazawa, 2004; Konhauser *et al.*, 2017) and

in certain environments has been shown to precipitate directly from Fe-rich anoxic fluids (Grengs *et al.*, 2024). The amount of siderite precipitation taking place follows CHEES:

$$SideP_x = k_{Side} * max[(\Omega_{side} - 1), 0] * vol_x \quad (77)$$

Where, k_{Side} is a reaction rate constant for siderite, and the saturation state for siderite is derived thus:

$$\Omega_{side} = \frac{Fe(II)_{conc_x} * [CO_3^{2-}]_x}{Ksp_{side}} \quad (78)$$

2.11. Other model variables and fluxes

2.11.1. Sulfide oxidation

In oxygenated environments sulfide can be oxidised to sulfur intermediates, such as thiosulfates and elemental sulfur, and eventually back to sulfate (Fike, Bradley and Rose, 2015). In AMMONITE, as with CHEES, this flux relies on the concentrations of sulfide and O_2 in each ocean box and the modern-day formation rate:

$$sulfO_x = max\left[\left(k_{sulfO} * H_2S_{conc_x} * O_{2conc_x} * vol_x\right), 0\right] \quad (79)$$

2.11.2. Air-sea gas exchange of O_2

As with CO_2, there is an exchange of O_2 between the surficial ocean and atmosphere. This bi-directional flux is determined by the following equation (Zhao *et al.*, 2023):

$$f_{airsea\_O2\_x} = k_{pv\_x} * \left(O_{2\_eq\_ax} - O_{2\_conc\_x}\right) \quad (80)$$

Where k_{pv_x} is a piston velocity, $O_{2\_conc\_x}$ is the concentration of O_2 in the ocean, and $O_{2\_eq\_ax}$ is the oxygen saturation concentration as it equilibrates between the atmosphere (subscript *a*) and the relevant ocean box (subscript *x*). The oxygen saturation concentration is calculated as follows:

$$O_{2\_eq\_ax} = \frac{1}{k_{mv}} * \frac{O_{2\,a\,(t)}}{O_{2\,a\,(0)}} * e^{C_{Weiss}} \quad (81)$$

The term k_{mv} is the real gas molar volume for O_2 derived from Van der Waals constants (Emerson and Hedges, 2008), and C_{Weiss} is the gas solubility of O_2 determined by Weiss (Weiss, 1970), which is dependent on temperature (in °K) and salinity (*sal*):

$$C_{Weiss} = A_1 + \left[A_2 * \frac{100}{T_{x\,(\deg K)}}\right] + \left[A_3 * ln\left(\frac{T_{x\,(\deg K)}}{100}\right)\right] + \left[A_4 * \frac{T_{x\,(\deg K)}}{100}\right] + sal * \left\{B_1 + \left[B_2 * \frac{T_{x\,(\deg K)}}{100}\right] + \left[B_3 * \left(\frac{T_{x\,(\deg K)}}{100}\right)^2\right]\right\} \quad (82)$$

2.12. The nitrogen cycle

SCION and COPSE incorporate a minimalist oceanic nitrogen cycle (Lenton, Daines and Mills, 2018; Mills, Donnadieu and Goddéris, 2021) where the concentration of nitrate (here, N) throughout the Phanerozoic varies as a result of nitrogen fixation, denitrification and organic nitrogen burial. We add this cycle to AMMONITE but retain its simplified form, rather than expanding all processes across each ocean region. We calculate: a summed N fixation (f_{nfix}) rate for the whole ocean; denitrification in each ocean box (f_{denit_x}), which is then summed together to provide a global value; and total nitrogen burial (f_{monb}):

$$f_{nfix} = \begin{cases} 0, \ if \ \frac{[N]_{(t)}}{16} > [P]_{total\,(t)} \\ k_{nfix} * \left[\frac{[P]_{total\,(t)} - \left(\frac{[N]_{(t)}}{16}\right)}{[P]_{total\,(0)} - \left(\frac{[N]_{(0)}}{16}\right)}\right]^2, \ if \ \frac{[N]_{(t)}}{16} < [P]_{total\,(t)} \end{cases} \quad (83)$$

$$f_{denit\_x} = \left(\frac{1}{5} * k_{denit}\right) * \left[1 + \frac{DOA_x}{1 - k_{oxfrac}}\right] * \frac{[N]_{(t)}}{[N]_{(0)}} \quad (84)$$

$$f_{monb} = \frac{f_{mocb\_total}}{C{:}N_{ocean}} \quad (85)$$

Here, k_{nfix} and k_{denit} are the present-day flux sizes for N fixation and denitrification; $C{:}N_{ocean}$ is the C:N ratio used for marine N burial in COPSE; f_{mocb_total} is the summation of organic carbon burial taking place in the three ocean boxes connected to the sediments; and k_{oxfrac} is a constant representing the

781 fraction of the modern ocean which is oxic. DOA_x is the degree of anoxia in each ocean box, and is
782 calculated thus:

783 $$DOA_x = max\left[1 - \left(k_{oxfrac} * \frac{O_{2x(t)}}{O_{2x(0)}}\right), 0\right] \quad (86)$$

784 For the purposes of this work, we only use N concentrations as an illustrative tracer of nutrient changes
785 through time. It does not function as a limiting nutrient and no other model processes are dependent on
786 the N cycle.

787

788 2.13. Alkalinity

789 Alkalinity is an important component of the marine system, helping to keep track of the charges
790 entering and leaving the ocean (Zeebe and Wolf-Gladrow, 2001). The weathering of minerals changes
791 the alkalinity balance of the ocean via the delivery of proton acceptors such as bicarbonate and
792 carbonate ions, as well as acids (e.g. sulfuric, silicic, phosphoric, boric, and water) which then undergo
793 dissociation (Zeebe and Wolf-Gladrow, 2001; Wolf-Gladrow *et al.*, 2007). In AMMONITE, although
794 we track alkalinity and it influences, and is influenced by, other components of the carbonate system,
795 we are careful to say that we are not considering total alkalinity here. To do so would require a more
796 comprehensive nitrogen system at the least, as currently in the model primary production is solely
797 dependent on phosphorus, and depending on the form of nitrogen being utilised, primary production
798 can be a source, sink or neutral with regards to its effect on alkalinity (Wolf-Gladrow *et al.*, 2007).
799 Instead, we include carbonate alkalinity with further contributions from the Fe and S cycles. Here,
800 silicate and carbonate weathering both result in an increase in alkalinity by two mol equivalents,
801 whereas carbonate (including siderite) formation in the ocean has a corresponding effect of a decrease
802 by two mol equivalents (Walker and Kasting, 1992; Zeebe and Wolf-Gladrow, 2001; Soetaert *et al.*,
803 2007; Wolf-Gladrow *et al.*, 2007; Krumins *et al.*, 2013).

804

For the Fe and S cycles, the reduction of iron (oxy)hydroxides and sulfate by microbes using organic matter as the electron donor enhances alkalinity by eight and two mol equivalents, respectively (Soetaert *et al.*, 2007; Krumins *et al.*, 2013; Rassmann *et al.*, 2020), while sulfide mediated iron reduction increases it by four mol equivalents (Soetaert *et al.*, 2007). The oxidation of Fe(II) and various reduced sulfur species decreases alkalinity, in both cases, by two mol equivalents (Soetaert *et al.*, 2007; Rassmann *et al.*, 2020). Although the simplified final step of pyrite formation, following the reaction of iron monosulfide with hydrogen sulfide, is neutral regarding alkalinity change, the full chain reaction involving organic matter, sulfate, iron (oxy)hydroxides, and occasionally free protons, results in the generation of two mol equivalents of alkalinity (Rassmann *et al.*, 2020). In AMMONITE we use this net increase when it comes to alkalinity change as a consequence of pyrite formation.

In the full consideration of total alkalinity, phosphorus is included as three species: phosphoric acid (H_3PO_4); hydrogen phosphate (HPO_4^{2-}); and phosphate (PO_4^{3-}), where H_3PO_4 and HPO_4^{2-} contribute to the alkalinity balance by -1 and +1 mol equivalents respectively, and PO_4^{3-} by -2 mol equivalents (Zeebe and Wolf-Gladrow, 2001). Despite it being a dissociation product of phosphoric acid, $H_2PO_4^-$ is not included in total alkalinity, as its proton condition is at the zero level (Zeebe and Wolf-Gladrow, 2001; Wolf-Gladrow *et al.*, 2007). To include the full scope of the P cycle on alkalinity then, would require the implementation of an approach similar to that of the carbonate system in this model, which is beyond the scope of this current piece of work. Similarly, as we do not have silica or boron cycles we omit their contributions to alkalinity, leaving this as fruitful areas for future research.

2.14. Model operation

For compatibility with existing SCION code, AMMONITE has been built using the MATLAB programming language. We use the routine ode23t to solve the full set of SCION-AMMONITE ordinary differential equations detailed in Table S3. The coupled model can output results in three modes: 1) all flux, reservoir and graphical outputs for a single model run across the entire Phanerozoic, which takes

approximately 5 minutes to complete on a single CPU; 2) as per mode one, but with only the flux and reservoir outputs; 3) a parallelised 'Monte Carlo' sensitivity ensemble which conducts multiple model runs across the Phanerozoic, sampling linearly between defined bounds for certain model forcings/variables (see Table 3), and outputting a smaller subset of flux and reservoir results.

Table 3: Parameters, and their boundaries, included in the Monte Carlo ensemble.

Parameter	Lower boundary	Upper boundary	Source
Degassing, *D*	Minimum combined estimate	Maximum combined estimate	(Merdith *et al.*, 2025)
Basaltic area, BAS_{area}	Baseline area – 20%	Baseline area + 20%	(Lenton, Daines and Mills, 2018)
Granitic area, $GRAN_{area}$	Baseline area – 20%	Baseline area + 20%	(Lenton, Daines and Mills, 2018)
Enhanced terrestrial weathering by plants due to CO_2 fertilisation, *PREPLANT*	1/7	1	(Lenton, Daines and Mills, 2018)
$[Ca^{2+}]_{sw}$, *Calc*	Minimum combined estimate	Maximum combined estimate	(Krause *et al.*, 2024)

For the baseline model results in this work, we use mode three, running the model 2,000 times, and plotting the mean, minimum and maximum values of all model runs at each time point. Some combinations of the sampled forcings/variables cause the model to crash during its spin up phase (between 600–570 Ma), but we remove these model runs (n = 254) prior to statistical processing.

3. Results and discussion

Major predictions from the linked SCION-AMMONITE model for the Phanerozoic are shown in Figure 2 for the atmosphere and land surface and Figure 3 for the ocean. In both cases they are compared to the current SCION model (with single ocean-atmosphere box) and available proxy data.

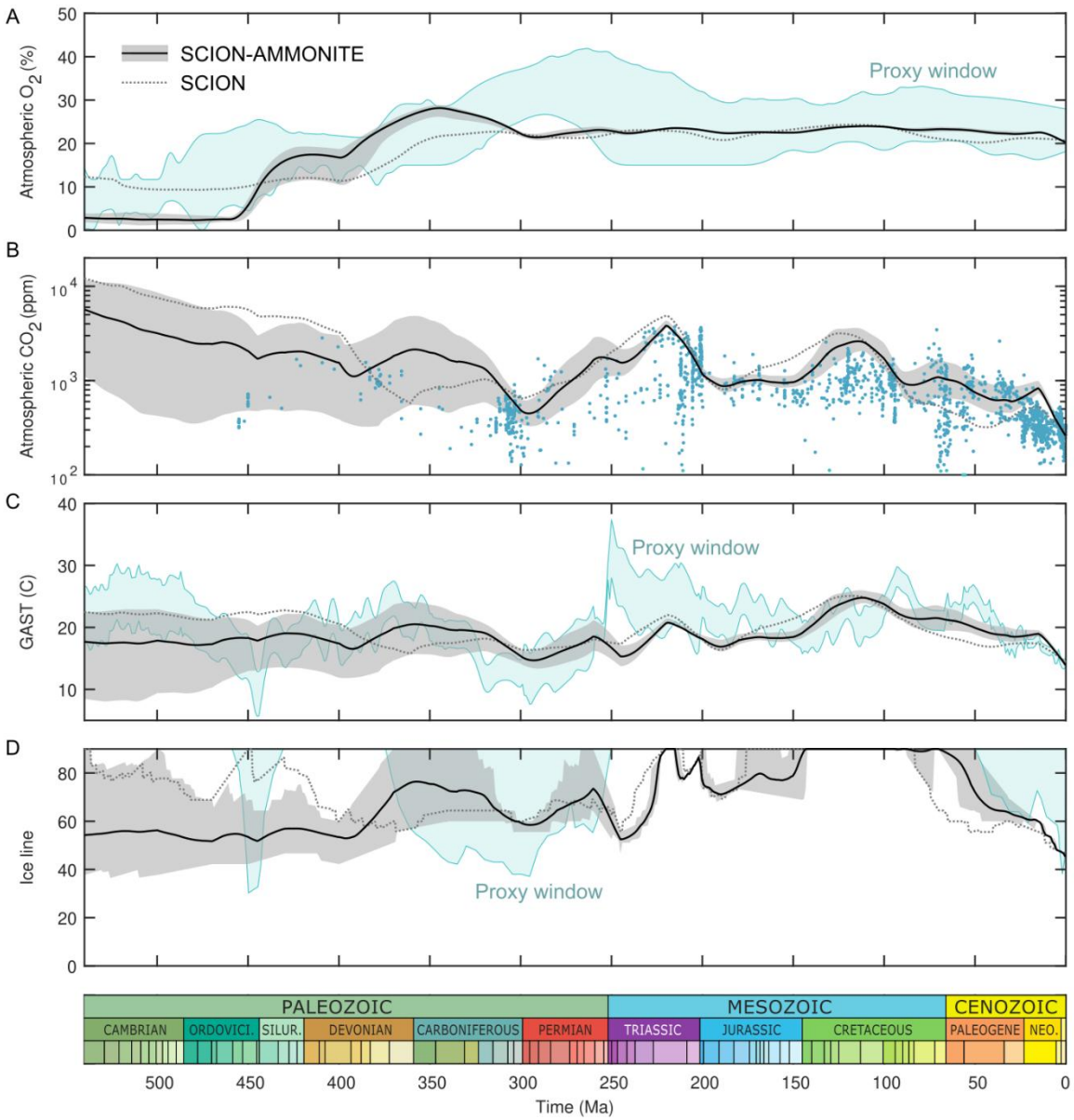

Figure 2 | Modelled atmospheric and surface conditions. *A. Atmospheric O_2 against combined proxy window from Mills et al. (2023). B. Atmospheric CO_2 against combined proxy data points from Foster et a. (2017) and Witkowski et a. (2018). C. Global Average Surface Temperature (GAST) against combined proxy window from Scotese et al. (2021). D. Ice sheet paleolatitude against geological compilation from Scotese (2021). For each panel, black solid lines and shading show the present SCION-AMMONITE model and uncertainty window whereas dashed lines show the previous SCION model with zero-dimensional ocean (Merdith et al. 2025).*

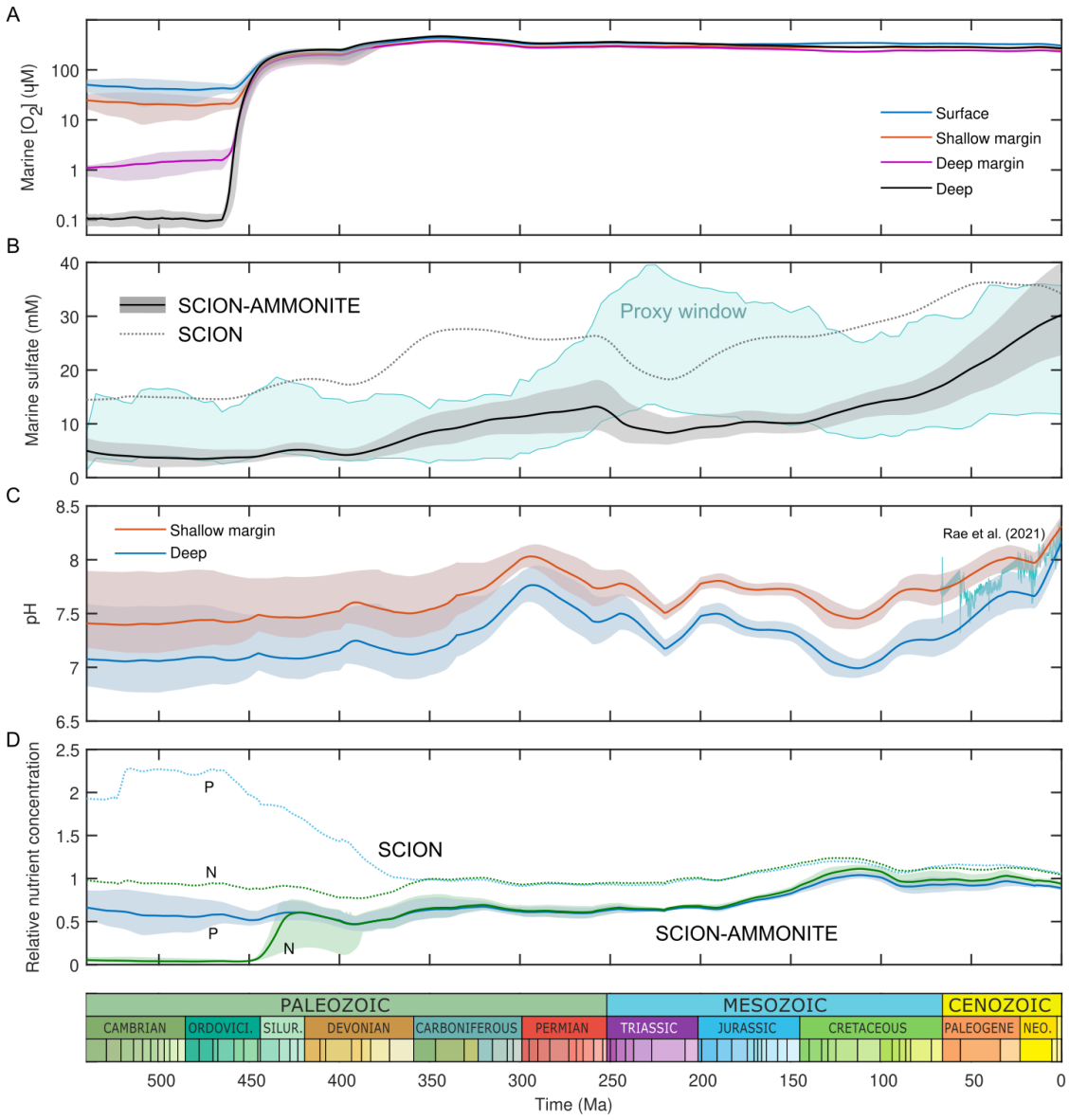

858

859 ***Figure 3 | Modelled marine conditions***. *A. Marine oxygen concentration across ocean boxes in the*
860 *AMMONITE module. B. Globally-averaged marine sulfate concentrations compared to the microbial*
861 *sulfate reduction proxy (Algeo et al., 2015). C. Marine pH in the shallow margin and deep ocean*
862 *compared from pH reconstructed from boron isotopes in Rae et al. (2021). D. Relative nutrient*
863 *concentrations across the global ocean. For panels B and D, solid lines and shading show the present*
864 *SCION-AMMONITE model and uncertainty window whereas dashed lines show the previous SCION*
865 *model with zero-dimensional ocean (Merdith et al., 2025).*

866

867 3.1. O_2 in the atmosphere and ocean

868 SCION-AMMONITE predicts O_2 levels in the atmosphere (Figure 2A) which generally align
869 with both marine and terrestrial proxies and modelling constraints, summarised by the proxy window
870 shown. In contrast to SCION, the mean predicted early Paleozoic O_2 concentrations are well below the
871 modelled threshold (~10.5% atm) by which we would expect a consistently well oxygenated deep ocean
872 (Canfield, 1998). Instead, our results tarry with compilations of redox-sensitive proxies such as Fe
873 speciation, Mo and U isotopes, Ce anomalies etc. which suggest that widespread deep ocean anoxia
874 (and consequently expected atmospheric O_2 levels of <~10% atm) continued until at least the
875 Ordovician, with regional euxinia extending into the early Silurian (Dahl *et al.*, 2010; Sperling *et al.*,
876 2015; Wallace *et al.*, 2017; Tostevin *et al.*, 2019; Stockey *et al.*, 2020; Liu *et al.*, 2021).

877

878 In this regard, our results improve upon those made by the SCION model (Mills et al., 2021),
879 which suggested higher concentrations throughout the Paleozoic, with no rise in O_2 coincident with the
880 earliest evolution and spread of terrestrial plants. This is partly due to the incorporation of sulfur
881 degassing fluxes, which are not present in SCION, whereby 'pyrite degassing' (i.e. the oxidation of
882 sulfides in the crust and mantle from volcanism and metamorphism, leading to the release of SO_2 gas)
883 rates are relatively high in the early Paleozoic as a consequence of the larger sedimentary reservoir in
884 the Precambrian (Canfield and Farquhar, 2009). Pyrite degassing reduces O_2 levels in the waters
885 overlying the ocean sediments, with air-sea gas exchange then stabilising some of this ocean O_2 loss via
886 reduction in atmospheric O_2 levels. Additionally, lower limiting nutrient (see Section 3.4.) and sulfate
887 levels (Section 3.5.) in AMMONITE are constraining both the amount of primary production and pyrite
888 formation – both eventually sources of O_2 to the atmosphere – taking place respectively. Therefore,
889 changes to both the sources and sinks of oxygen are providing the lower predictions by SCION-
890 AMMONITE through this time, and these appear reasonable as they are based on the consideration of
891 a generally accepted large sedimentary pyrite reservoir and low marine sulfate level for the early
892 Paleozoic.

At ~450 Ma, the model charts the first major increase in O_2 to a level above the absolute minimum threshold required (15%) for the spontaneous ignition of fire (Belcher and McElwain, 2008; Belcher, Collinson and Scott, 2013), and at ~400 Ma matches the atmospheric O_2 level suggested by the charcoal proxy record (Glasspool and Scott, 2010; Glasspool *et al.*, 2015; Mills *et al.*, 2023). This rise is much greater than that in SCION because we assume a high C:P ratio for early plants as in COPSE (Lenton, Daines and Mills, 2018; Mills, Donnadieu and Goddéris, 2021). From there, our model predicts a second rise in oxygen, reaching a peak of ~28% at ~350 Ma, and again is higher than in SCION due to the assumptions of high C:P ratios of terrestrially-derived organic matter during widescale coal formation in swamps (Lenton, Daines and Mills, 2018). O_2 levels then decline towards modern day levels by the end of the Carboniferous, where the C:P ratio is assumed to decline to modern values, and tracks the original SCION predictions thereafter. The lower Permo-Carboniferous O_2 in both SCION and AMMONITE is in contrast to records generated by isotope mass balance models, which indicate that drastically elevated atmospheric O_2 continued until at least the end of the Permian, and was potentially higher than modern day levels for much of the Mesozoic too (Berner, 2009; Krause *et al.*, 2018; Mills *et al.*, 2023). However, SCION and AMMONITE both plot within the range reconstructed from the charcoal proxy, and crucially remains within an O_2 limitation window (~15-35%) below which there would be no occurrences of wildfires, and above this level the combined effect of enhanced photorespiration and wildfires would severely stunt the areal extent of vegetation either via growth inhibition and/or from large scale destruction, leaving a recognisable mark on multiple biogeochemical cycles (Watson, 1978; Belcher and McElwain, 2008; Belcher, Collinson and Scott, 2013; Vitali *et al.*, 2026).

Oxygen in the ocean boxes (Figure 3A) mirrors the overall trend set by atmospheric O_2, with lower concentrations ($[O_2]$) in the earliest Paleozoic followed by a rise in $[O_2]$ in all boxes at the same time as atmospheric O_2 increases. For the three surface ocean boxes, $[O_2]$ lie within a dysoxia (e.g. ~8.17 μM < $[O_2]$ < ~81.7 μM) window (Tyson and Pearson, 1991) and are often below a hypoxia threshold (~62.5 μM, Vaquer-Sunyer and Duarte, 2008) until the Devonian. Whilst this may appear

contrary to proxy data, which suggests an oxygenated surface ocean has been present since the Great Oxidation Episode (Lyons *et al.*, 2024), due to the low spatial resolution of the ocean, we cannot capture the true depth or regional gradients of surface ocean oxygen levels throughout time, instead we can only provide an averaged estimate for each ocean box. Moreover, oxygenation is spatially heterogeneous and waters overlying the shelves are prone to deoxygenation through time up until the present day (Kwiecinski and Babbin, 2021; Feng *et al.*, 2025). This is hypothesised to be the case even if atmospheric O_2 was at modern day levels throughout the Phanerozoic (Pohl *et al.*, 2022). Because of a combination of: modelled high temperatures during the early Paleozoic; the overall small inventory of oceanic O_2; and the anoxic deep margin and deep waters, the surface ocean boxes in our model have a lower holding capacity for dissolved gases such as oxygen, and are also not sufficiently replenished by thermohaline circulation or by enhanced primary production. After the evolution of land plants our model predicts that both surface and deep ocean waters would have been extensively oxygenated.

Our deep margin and deep water boxes lie below the dysoxic threshold until land plant evolution, aligning well with the various geochemical proxies gathered from sediments in these areas of the ocean (Dahl *et al.*, 2010; Sperling *et al.*, 2015; Wallace *et al.*, 2017; Tostevin *et al.*, 2019; Stockey *et al.*, 2020; Liu *et al.*, 2021). While both these boxes also exceed the dysoxic threshold with the evolution and spread of land plants, there are times when the deep ocean has higher oxygen levels than the deep margin ocean. This is unsurprising, as oxygen minimum zones or anoxic wedges often form in deeper waters overlying continental shelves, where microbial processing of sinking detritus can rapidly consume oxygen (Canfield and Kraft, 2022), but it is good to see that AMMONITE can capture this real world phenomena.

3.2. Atmospheric CO_2, temperature and ice line

SCION-AMMONITE predicts, similarly to many other Earth system box models (Berner, 2008; Lenton, Daines and Mills, 2018; Mills, Donnadieu and Goddéris, 2021; Alcott *et al.*, 2024;

Krause *et al.*, 2024; Merdith *et al.*, 2025), that CO_2 levels in the atmosphere were substantially higher in the terminal Ediacaran and Cambrian than at present (Figure 2B). SCION-AMMONITE returns lower CO_2 predictions in the Cambrian to Silurian than SCION, despite both models using the same uncertainty ranges in their Monte Carlo ensembles for degassing, terrestrial silicate area (and proportion of basalt to granitic split), and amplitude of biotic weathering enhancement, all of which should affect CO_2 sources and sinks in the same manner. Some of this variance is undoubtedly a result of the reintroduction of the *B* parameter (see Section 4.1.), as well as the different present-day flux sizes chosen (Table S4), but there will also be a contribution from the lower predicted atmospheric oxygen levels, which restrict the carbon source through a reduction in oxidative weathering compared to SCION.

Since then, overall, both in the proxy record and in the model, CO_2 has steadily declined apart from three distinct punctuations from the trend: in the late Carboniferous, which experienced a transient, geologically rapid decline; the mid-Triassic, with a large increase; and another rise in levels in the mid-Cretaceous. Here, SCION-AMMONITE differs from SCION in predicting higher Devonian-Carboniferous CO_2, because of the assumed larger increase in O_2 levels driven by early plant evolution and the resulting increase in oxidation of continental organic carbon. Nevertheless, the results of our modelling continue to provide a good fit to the proxy compilation (Foster, Royer and Lunt, 2017; Witkowski *et al.*, 2018), with the only real disagreement occurring in the mid-Devonian to mid-Carboniferous where both SCION-AMMONITE and SCION predict rising CO_2, whereas the CO_2 proxies, temperature records (Scotese *et al.*, 2021; Judd *et al.*, 2024) and shift of the ice line towards lower latitudes (Scotese *et al.*, 2021) suggest a decrease, facilitating the Earth's shift into an icehouse climate. However, the minimum of our Monte Carlo sampling does hint that lower CO_2 can be achieved by the model, and thus at this period of time it is possible that the Earth experienced degassing levels at the lower end of those recreated (Merdith *et al.*, 2025), or that the model paleogeography and climate emulation here still needs revision (Zhang *et al.*, 2025). Improved climate emulation may also improve the model fit in the Neogene, where both SCION-AMMONITE and SCION predict CO_2 levels higher

than the proxy record, but the modelled temperature is at the upper end of the window (Scotese *et al.*, 2021) or firmly within the confidence intervals (Judd *et al.*, 2024) of the proxy record. At the same time, there is a small contraction of our ice line towards higher latitudes, which gets the timing, but not the magnitude, correct with regards to the reconstructed paleo ice line (Scotese *et al.*, 2021).

3.3. pH

To date, few other models have produced a continuous pH record for the last 540 Myr, with most producing broad predictions through time, showing generally a monotonic rise in pH levels (Halevy and Bachan, 2017; Krissansen-Totton, Arney and Catling, 2018; Krissansen-Totton, Kipp and Catling, 2021). There are two exceptions to this.

1) The earlier version of the MAGic model (Arvidson, Mackenzie and Guidry, 2006), which estimated: pH < 8.1 in the early Paleozoic, the Cretaceous, and at 0 Ma; with pH ≥ 8.1 during the late Paleozoic – Triassic, and much of the Cenozoic, contrary to what the boron isotope proxy suggests (Rae *et al.*, 2021). A later version of the model loses much of this variability in pH, with an almost steady increase in pH from 7 to 8.1 units across the Phanerozoic (Arvidson, Mackenzie and Guidry, 2013).
2) A simple calcium-magnesium model which produces pH levels for surficial and deep waters for the last 550 Myr (Farkaš *et al.*, 2007). Similarly to MAGic, this model suggests that both surface and deeper waters were more acidic in the early Paleozoic, and surface water pH rose to something akin to modern, pre-industrial levels in the Carboniferous and Permian. However, with this model, the ocean became more acidic across the Triassic, whereas in MAGic this decline occurred later, in the Early Jurassic (Arvidson, Mackenzie and Guidry, 2006). From approximately the Middle Jurassic, both surface and deep waters rise, sometimes sharply, to modern-day pH levels (Farkaš *et al.*, 2007).

AMMONITE provides, for the first time in decades for these types of Earth system box models, temporally variable pH estimates across the entire Phanerozoic (Figure 3C), at a greater spatial

resolution than previously presented. These results tend to agree more closely with Farkaš *et al.* (2007), rather than other more recent work (Arvidson, Mackenzie and Guidry, 2013; Halevy and Bachan, 2017; Krissansen-Totton, Arney and Catling, 2018; Krissansen-Totton, Kipp and Catling, 2021), and suggest that pH has not monotonically risen over the last ~540 Myr.

The pH is, as expected, considerably lower in the deep ocean than the other ocean boxes, and while changes in pH levels occur simultaneously across all ocean boxes throughout the Phanerozoic, the magnitude of such variances is not equal, with the deep ocean exhibiting the greatest range in pH variability. The pH values for the surface ocean boxes are broadly similar, but it tends to be slightly more acidic in the high-latitude than the shallow margin and low-latitudes. This is a result of a mixture of processes: The products of all weathering processes enter the shallow margin ocean box, altering the alkalinity balance and providing the cations required for carbonate production, with much of the carbonate burial taking place on shallow continental shelves, releasing a mole of CO_2 for every mole of $CaCO_3$ buried. As warmer ocean temperatures in the shallow margin (and in the low-latitude) surface box mean they are less able to retain dissolved CO_2 than the cooler waters of the high latitudes, outgassing to the atmosphere is favoured here, shifting the carbonate system towards less free H^+ and thus a more alkaline pH (Walker and Kasting, 1992; Zeebe and Wolf-Gladrow, 2001).

Despite high temperatures in the early Paleozoic, the sheer abundance of CO_2 in the atmosphere means that the amount of dissolved CO_2 is also high, such that the carbonate system has been shifted towards major H^+ production in all ocean boxes, resulting in pH levels far below the pre-industrial global ocean average of 8.2–8.3 (Rae *et al.*, 2021). Aside from a brief rise to something more akin to a pH of 8.2 in the Permo-Carboniferous due to lower CO_2 levels, AMMONITE predicts that surface ocean pH levels have remained alkaline (i.e. pH > 7) but were far below 8.2 for almost the entirety of the Phanerozoic, and that quite basic waters are a late Cenozoic phenomenon. The model results for the surface ocean throughout the Cenozoic provide a generally good fit to estimations using boron isotopes

during this time (Rae *et al.*, 2021). Prior to the Cenozoic there have been, to date, few other proxy-based reconstructions of pH, as boron isotope work done to specifically determine paleo-CO_2 and pH has been mainly conducted on foraminifera which, despite their likely evolution in the Neoproterozoic, have not always been well preserved (somewhat due to the lack of remaining deep ocean sediments from before the Jurassic)(Pawlowski *et al.*, 2003; Steinthorsdottir *et al.*, 2025). Thus, Paleozoic and Mesozoic comparisons are currently limited and we eagerly await the results of experimental work on conducting boron isotopes on other species, such as radiolarians and brachiopods. In early work here, Jurikova *et al.* (2025) estimate pH from brachiopod boron isotopes for the Carboniferous-Permian and suggest values of around 7.7–8.2 units, with a decrease across this range in the early Permian. AMMONITE predictions sit in a similar range, and also record a decline here, but over a greater timeframe.

AMMONITE reproduces pH records which are very similar, not only in terms of the pH units, but also the timing of rises and falls in levels, to the calcium-magnesium model of Farkaš *et al.* (2007). For example, their early Paleozoic pH for the surface and deep ocean is ~7.5 and ~7.1–7.2, respectively, while AMMONITE predicts ~7.4 and ~7.1 during this time. The calcium-magnesium model has a small transient rise in pH during the end-Silurian – early Devonian, whilst our model also has a small transient rise a little later, in the mid-Devonian. Both models have approximately modern-day pH levels in the Permian, and showcase sharp rises from the Cretaceous onwards. AMMONITE shows more variability, particularly during the Late Triassic and Early Cretaceous, with sharp declines in pH, and much of this is due to the updated degassing forcing, with additional effects from the remineralisation of organic matter and spatial weathering present in our model. However, it is interesting that differing approaches to modelling the Earth system are producing broadly comparable pH records.

Our model results also align well with inverse carbon cycle modelling work (Krissansen-Totton, Kipp and Catling, 2021), and importantly, the pH levels for the surface ocean reservoirs at the end of

the model run are within the reconstructed global average of 8.2–8.3 prior to the industrial revolution (Rae *et al.*, 2021). Additionally, post the industrial revolution, it should be noted that measured pH levels vary substantially both latitudinally and longitudinally. For example, a compilation of in-situ measurements from oceanographic cruises covering ~60°S to 60°N in the western Pacific show a wide range in pH: from ~8.0–8.1 at 60°S, to ~7.9–8.5 in the tropics, to <7.8 at ~60°N, albeit these were recorded prior to the 1990s and thus the equivalent values on the total scale are uncertain (Dickson, 1993; Skirrow, 1965 cited in Bethke, 2021). But, altogether, this gives us confidence that the model, at least in the Cenozoic, is functioning as expected.

For the deep ocean, AMMONITE suggests that the pH, although lower than surface waters, likely remained neutral to alkaline for the entire Phanerozoic, albeit the minimum values obtained from our Monte Carlo sampling indicates that it could have been mildly acidic until the Carboniferous and for a few Myr during the Cretaceous. However, in this work we do not change eustasy, which would change the total amount of carbonate formation (and dissolution) and how this is apportioned between shallow margin, deep margin, and deep ocean sediments, nor do we include reverse weathering. Both of these processes would alter the alkalinity balance and thus pH of the ocean (Dunlea *et al.*, 2017; Isson and Planavsky, 2018; Rahman and Trower, 2026). As a consequence, the model currently misses some of the finer scale acidification events, such as the Middle Eocene Climatic Optimum, where a shoaling of the carbonate compensation depth occurred concurrent with multi-kyr warming, possibly due to a combination of: continental weathering changes; enhanced clay formation on the continents and in the ocean; alongside changes to the organic carbon cycle (Spofforth *et al.*, 2010; Sluijs *et al.*, 2013; Van Der Ploeg *et al.*, 2018; Henehan *et al.*, 2020; Krause *et al.*, 2023). Both processes could be incorporated in future work.

3.4. P and N levels

In COPSE, and consequently SCION, marine organic carbon burial rates are highly dependent on the relative amount of primary production taking place as a function of the relative amounts of nitrate (here N) to phosphate (here P) in the ocean, with N being the proximate limiting nutrient (Lenton, Daines and Mills, 2018; Mills, Donnadieu and Goddéris, 2021). For both COPSE and SCION, N levels are tightly regulated within 20-30% of modern-day levels for the entire ~540 Myr model run (Mills, Donnadieu and Goddéris, 2021). While, in both of these models P levels are much higher (>2x modern) in the early Paleozoic and then decline during the Devonian, albeit the timing of this decline differs. For P, it is clear that changing atmospheric O_2 levels, which affect the anoxic fraction of the ocean, is driving P concentrations in both models due to enhanced burial of P with Fe oxy(hydroxides) as O_2 increases. This feedback is strong in the COPSE and SCION models because their oceans are based on simple functions taking place within a single box, so can become decoupled from atmospheric O_2 concentrations and therefore entirely anoxic with relative ease. In SCION, the anoxia of the early Paleozoic also increases denitrification, altering the N:P ratio and thereby allowing greater nitrogen fixation in the water column to rebalance the system (Mills, Donnadieu and Goddéris, 2021).

In SCION-AMMONITE, roughly the opposite to SCION is seen in the modelled results of P and N concentrations over the Paleozoic. Here, instead of P being elevated in the early Paleozoic, P levels are relatively low (~0.5 – 0.7x modern) and are more tightly regulated throughout the model run, whereas N levels are extremely low in the early Paleozoic. This demonstrates how the choice of which element is the limiting nutrient impacts the modelled P and N cycles: whichever nutrient is effectively limiting will be regulated through productivity feedbacks, whereas the non-limiting nutrient will be allowed to vary much more considerably if changes occur in their cycle. In SCION-AMMONITE, the low O_2 of the early Paleozoic drives high amounts of denitrification, which can deplete the marine N pool, as N levels do not limit productivity. In SCION, the almost complete anoxia in the early Paleozoic ocean also leads to high amounts of denitrification, but as N is the limiting factor this puts a cap on primary productivity and ultimately boosts marine P to high levels. Overall, this shows how nutrient co-limitation in the ancient ocean may be complicated by redox differences, but as AMMONITE does

not include bioavailable reduced forms of nitrogen like ammonium, it is difficult to link N to productivity and to draw further conclusions at this stage.

3.5. Sulfate concentrations

Our modelled sulfate concentrations are vastly different from those predicted by SCION, mainly due to the use of a proxy-informed calcium reservoir, which influences the amount of gypsum burial taking place and the timing of when this occurs. Sulfate predictions in SCION-AMMONITE are low in the early Paleozoic, with even the maximum values from our Monte Carlo ensemble remaining <10 mM until the late Devonian, whereupon levels rise moderately to the end of the Permian. After this, sulfate concentrations decrease slightly across the Triassic (mean of ~6–9 mM), before beginning a slow rise to modern day levels (28–29 mM) by the end of the model run. Our results are on the whole a good match to concentrations suggested by fluid inclusion proxy data, albeit they are a bit lower during the Permo-Carboniferous (Weldeghebriel *et al.*, 2022), and align well to levels from carbonate-associated sulfur isotopes for the early-mid Paleozoic (Gill, Lyons and Saltzman, 2007; Hurtgen, Pruss and Knoll, 2009; Gill *et al.*, 2011; Loyd *et al.*, 2012; He *et al.*, 2019; Cai *et al.*, 2022; Kozik *et al.*, 2022). The results tend to plot towards the low end of the reconstruction of levels from microbial sulfate reduction (Algeo *et al.*, 2015). As per previous modelling (Berner, 2004; Arvidson, Mackenzie and Guidry, 2013; Krause *et al.*, 2024), SCION-AMMONITE predicts the mid-Phanerozoic sulfate high occurred in the Permian, rather than the Triassic, most likely due to the timing of lower $[Ca^{2+}]_{sw}$ in the *Calc* forcing, thereby decreasing the gypsum burial sink for sulfate. These results represent an improvement in sulfate predictions compared to the unaltered SCION model (which has no Ca cycle), indicating the importance of calcium for controlling sulfate levels in these types of models (Mills, Donnadieu and Goddéris, 2021; Krause *et al.*, 2024).

As we have a multi-box ocean, we specified (for the first time for this class of box models) that gypsum burial rates are dependent on the concentration of sulfate in the shallow margin ocean, rather than the global ocean concentration. For the Phanerozoic this makes little difference to estimates of

gypsum burial as, despite changes over the last 540 Myr, the residence time of sulfate has remained very long (Krause *et al.*, 2024). Thus, the ocean is well-mixed, and concentrations are equal in all boxes. However, in the Proterozoic and beyond, when concentrations of sulfate were likely sub mM (Canfield, 2004; Kah, Lyons and Frank, 2004; Wortmann and Paytan, 2012; Fike, Bradley and Rose, 2015), it is possible that spatial differences in sulfate levels occurred, and therefore this distinction of where sulfate for gypsum burial is sourced from will become important in future work. In addition, unlike previous work (Krause *et al.*, 2024), we have not considered the impact on our results from discrete gypsum weathering and burial events as the timing and magnitude of these introduce more uncertainty into the model. Their inclusion may serve to close the model-proxy gap, particularly during the Permo–Triassic. However, a key driver of sulfate levels through time is the normalised calcium forcing, which, as previously mentioned, is used to help calculate gypsum burial rates. Thus, we explore the impact of this variable further in section 4.2.

4. Sensitivity testing

Although we conducted a Monte Carlo model run of AMMONITE, folding in a range of estimates for key parameters to generate an uncertainty envelope, we further explore the model response to two non-dimensional forcings (a greater Mesozoic increase in open ocean carbonate burial, *B,* and the assumed $[Ca^{2+}]_{sw}$, *Calc*) which have been scrutinised in recent work (Krause *et al.*, 2024; Merdith *et al.*, 2025). Figure 4 shows the baseline SCION-AMMONITE model alongside alternative runs where either *B* or *Calc* are kept fixed at the present-day value (i.e. *B* or *Calc* are equal 1 for the whole Phanerozoic). Model means only are shown here, for ease of comparison.

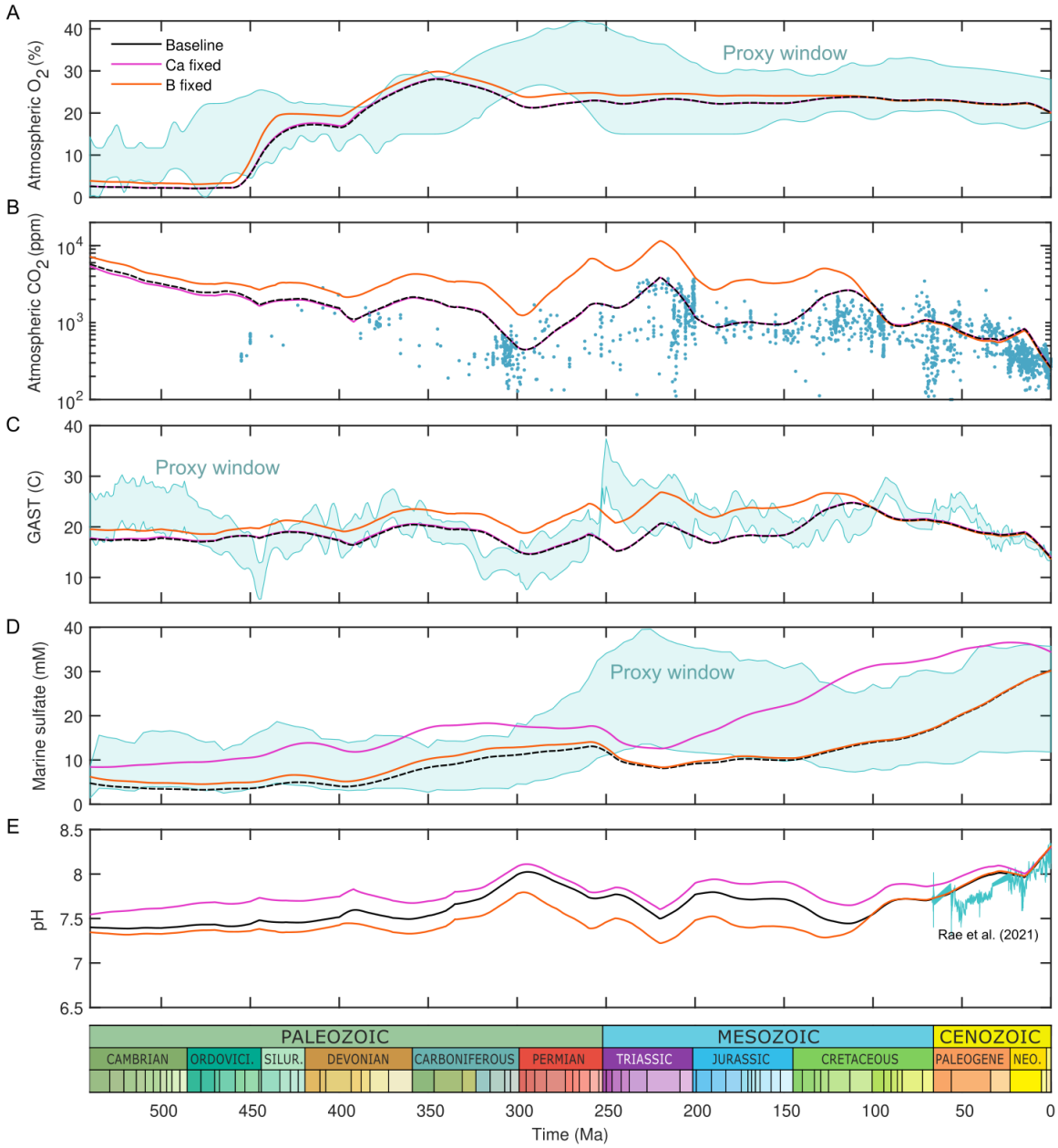

Figure 4 | Sensitivity to B parameter and Calc forcings. *Mean lines from the SCION-AMMONITE baseline run, as in Figures 2 and 3, are compared to the model with either a fixed Ca concentration (purple) or without the 'B' forcing (orange). A. Atmospheric O_2 against combined proxy window from Mills et al. (2023). B. Atmospheric CO_2 against combined proxy data points from Foster et al. (2017) and Witkowski et al. (2018). C. Global Average Surface Temperature (GAST) against combined proxy window from Scotese et al. (2021). D. Globally-averaged marine sulfate concentrations compared to the microbial sulfate reduction reconstruction (Algeo et al., 2015). E. Marine pH in the shallow margin compared to pH reconstructed from boron isotopes in Rae et al. (2021).*

4.1. The *B* nondimensional forcing

As previously mentioned in Section 2.2., the *B* parameter denotes how volcanic/metamorphic carbonate breakdown rates change when pelagic calcifiers evolve in the mid-Mesozoic (Volk, 1989; Berner, 1991). The value of *B* is set at 0.75 prior to 150 Ma, then rises linearly to the value of 1 by 100 Ma and remains at that value until the present-day, to highlight the expansion of pelagic calcifiers from the late Jurassic to early Cretaceous oceans, and the assumption that this would increase degassing rates via subducted deep ocean carbonate sediments. There is considerable uncertainty regarding this parameter and how it should be represented (if at all) within biogeochemical modelling. For example, the expression used in this work and others (Krause *et al.*, 2018; Lenton, Daines and Mills, 2018; Mills, Donnadieu and Goddéris, 2021) is taken from GEOCARB II (Berner, 1994), however, in that work Berner explored tying this parameter to changes to the total amount of subaerial land throughout the Phanerozoic, and in GEOCARB I (Berner, 1991) the rise at 150 Ma was faster and asymptotic, rather than linear. These explorations change atmospheric CO_2 predictions in GEOCARB considerably, particularly for the Paleozoic. As a result, Merdith *et al.* (2025) used plate tectonic modelling to explicitly quantify what contribution pelagic sediments make to arc degassing over the Phanerozoic, allowing them to omit *B* from their pySCION modelling after Müller *et al*. (2022). But, this change causes a divergence from the proxy record prior to 150 Ma, particularly during the early Triassic and late Jurassic to mid-Cretaceous, and while some of this can be explained by the climate sensitivity in FOAM (e.g. at the Permo-Triassic boundary, where their results are a good match to the temperature records (Scotese *et al.*, 2021; Judd *et al.*, 2024)), there are points where both CO_2 and temperature estimations are noticeably different from the proxies (Merdith *et al.*, 2025).

In order to explore greater variability here, we have re-incorporated *B* for the baseline AMMONITE model, but we also investigate the effect setting this to be equal to 1 for the entire Phanerozoic (i.e. it no longer puts a constraint on the size of carbonate degassing prior to 150 Ma) has

on certain model outputs. We kept all other model parameters the same and ran the model ensemble (see Figure 4). Unsurprisingly, all model results from 100 Ma to present remained generally the same (orange versus black line in Figure 4). While atmospheric O_2 is a few percent higher before 100 Ma, and sulfate levels prior to 250 Ma are, at most, ~3 mM higher, fixing *B* throughout the Phanerozoic predominantly causes CO_2 levels to be much higher throughout the Paleozoic and most of the Mesozoic, in the process driving air and ocean temperatures higher, and pH levels lower. These results are, as expected, closer to the original SCION model. Sometimes, for example during the Devonian, this brings GAST predictions closer to the proxy record, again highlighting the potential climate sensitivity issue with FOAM, but this change also produces a hothouse climate in the Carboniferous, contrary to data indicating an icehouse world (Scotese *et al.*, 2021; Judd *et al.*, 2024).

Thus, there is likely still more work to be done on understanding and reconstructing carbonate-related contributions to overall degassing through time, as well as other factors influencing CO_2 levels and global surface temperature. The problem may lie with the treatment of carbonate burial and deposition, and subsequent degassing in the model, as well as the simple vegetation scheme present. Ultimately, as the carbon cycle in deep-time Earth-system models such as COPSE and SCION are derived from the GEOCARB model (Berner, 1991), all carbonates which are buried enter into a singular sedimentary carbonate reservoir and thus are available for degassing at the next model timestep. This reservoir of carbon is very large in size – five orders of magnitude greater than the carbon residing in the atmosphere at present day (see Table 2) – thus small deviations in either the size of the sedimentary reservoir or degassing forcing can result in a substantial outflux of CO_2 to the atmosphere. However, this neglects that a) carbonate burial is spatially variant, with more occurring in marginal settings even after the evolution of pelagic calcifiers (O'Mara and Dunne, 2019) – although the *B* parameter tries to address this somewhat – but that substantial quantities of carbonate may have accumulated in deep ocean settings even before nanoplankton evolution (Husson and Peters, 2026); b) that different tectonic regimes will recycle carbon back to the atmosphere at different rates (Merdith *et al.*, 2025); and c) that crustal carbonate appears to have been increasing throughout Earth history (Hayes and Waldbauer,

2006; Lee *et al.*, 2016). An alternative to using the *B* parameter would be to directly impose upon the model the size of the sedimentary carbonate reservoir, as has previously been explored in other work (Krause *et al.*, 2022; Alcott *et al.*, 2024; Müller *et al.*, 2024), which would restrict the amount of CO_2 outgassing possible. Another option would be to break up the sedimentary carbonate reservoir into several smaller reservoirs and then use individualised relative forcings for each setting, which may result in more accurate CO_2 emissions through time. However, for now, for simplicity's sake, the *B* parameter serves as an adequate uncertainty function and helps explore uncertainty in atmospheric CO_2 predictions and their comparison with the proxy record.

4.2. The *Calc* forcing

In the absence of a dynamic calcium cycle within AMMONITE, we used the reconstruction of $[Ca^{2+}]_{sw}$ from fluid inclusions (Weldeghebriel *et al.*, 2022) which was then normalized to the present-day (Krause *et al.*, 2024) to help determine both $CaCO_3$ saturation, and gypsum burial rates. As $CaCO_3$ saturation, and consequently its burial, removes DIC from the ocean which could hitherto be used by primary producers, and as gypsum burial removes oceanic sulfate, in the process constraining sulfide production rates, the *Calc* forcing should be a powerful driver to changes to multiple biogeochemical cycles through Earth history.

Based on the fluid inclusion data available (Weldeghebriel *et al.*, 2022), it would seem that $[Ca^{2+}]_{sw}$ has consistently been higher than the present-day for the entire rest of the Phanerozoic, with extremely high concentrations peaking in the Ordovician-Silurian and the Cretaceous, delineated by a nadir in values towards the end of the Permian (Krause *et al.*, 2024). This double-humped feature of the $[Ca^{2+}]_{sw}$ is somewhat apparent in the baseline model results for sulfate, indicating some control over concentrations via modulating gypsum burial, but it is much less obvious than in previous modelling work (Krause *et al.*, 2024). Within the prior modelling framework, changing the *Calc* forcing had a minor effect on atmospheric O_2 predictions, a large effect on oceanic sulfate levels, but made no

difference to CO_2 results (Krause *et al.*, 2024). We were curious as to whether this was a consequence of the isotope mass balance approach or whether its combined ocean-atmosphere reservoir and lack of explicit carbonate chemistry was, in particular, preventing changes to the inorganic carbon cycle. Thus, we ran the baseline version of AMMONITE again but with *Calc* fixed to be 1 (i.e. $[Ca^{2+}]_{sw}$ is equal to the present-day concentration) for the whole of the model run.

Interestingly, as was the case before, this makes very little difference to our CO_2, atmospheric O_2 or GAST predictions. Ultimately, carbonate removal is required to balance the calcium and carbonate ion product, and changing calcium concentrations over very long timescales serves only to drive opposite changes in carbonate ion activity such that although there are regional variations, globally on average the product remains the same, resulting in only minor variations in total carbonate burial. This rebalancing around changing calcium levels has been demonstrated in simple multi-box models before (Shields and Mills, 2021) and can only drive clear changes in e.g. CO_2 levels during transient periods of large changes in calcium levels.

Also as noted in previous work, fixing *Calc* drastically changes sulfate concentrations, elevating them for the entirety of the last 550 Myr, in a similar way to the original SCION model, in the process providing a poorer fit to fluid inclusion data (apart from in the Carboniferous and Cambrian)(Weldeghebriel *et al.*, 2022) and the microbial sulfate reduction trend reconstruction (Algeo *et al.*, 2015). This divergence in $[SO_4^{2-}]_{sw}$ are not driven by the pyrite side of the sulfur cycle, as burial and weathering rates, and thus the sedimentary reservoir size, are the same in the baseline and fixed-*Calc* versions of the model for the entire Phanerozoic. Instead, possibly because of the difference in the flux sizes, the deviations in $[SO_4^{2-}]_{sw}$ between the two model runs are entirely as a result of variations to gypsum weathering and burial rates, and thus changes to the proportion of sulfate in the ocean versus that residing in the sediments. Gypsum weathering is enhanced throughout the Phanerozoic in the baseline run compared to the fixed-*Calc* version, albeit noticeably more so post-Jurassic, but the timing

of changes to weathering rates remains consistent across model versions. For gypsum burial, rates are similar across model runs until the Jurassic and then deviate markedly, coinciding with an increase in pyrite burial. Thus, while the *Calc* forcing has two peaks (one in the Ordovician, the other in the Cretaceous), enhanced removal of sulfate during the Mesozoic (versus the Paleozoic) in the baseline model run is compounded by higher sulfate-sulfide-pyrite conversion at the same time. This means that if we were to improve the model spin-up conditions such that the fixed-*Calc* version of AMMONITE could reproduce ~29 mM sulfate at 0 Ma, this would likely drag down the concentrations to be similar to that of the baseline model from the Paleozoic until the Jurassic, but they would remain elevated from the Jurassic until the present-day. However, changing model spin-up conditions does not always move estimations up or down by a few mM for the entire Phanerozoic, as these affect internal feedbacks in hard to predict ways, thus altering these may somewhat reduce the Mesozoic – Cenozoic sulfate estimation difference between the model runs.

Interestingly, this change to *Calc* also serves to increase the pH of the different ocean boxes, sometimes by as much as ~0.3 pH units, representing a substantial mopping up of H^+, despite only minor changes to the total global carbonate burial taking place. As above, this is mainly linked to changing carbonate ion activity, due to rebalancing of calcium carbonate solubility at different Ca levels (Shields and Mills, 2021), but there will be some contribution via changes in modelled alkalinity from the effects of *Calc* on the global sulfur cycle. However, the pH remains within the window where it is being controlled by HCO_3^- concentrations (Zeebe and Wolf-Gladrow, 2001). Altogether, the role of calcium in biogeochemical modelling should be looked at in finer detail in future work via the incorporation of a more comprehensive calcium cycle.

5. Conclusions

Here, we have presented a new Earth system model: SCION-AMMONITE, which combines 3D general circulation, whole plate tectonic, and multi-box biogeochemical modelling to produce new

estimates for key variables conducive to understanding the chemical evolution of the Earth and life, over the Phanerozoic. This represents a considerable increase in model complexity, whilst still maintaining the ability to compute hundreds of millions of years in a reasonable amount of wall-time on a single CPU core. The model introduces the AMMONITE multi-box atmosphere-ocean allowing for the computation of explicit carbonate chemistry which helps to improve atmospheric CO_2 levels compared to previous modelling efforts (e.g. Lenton, Daines and Mills, 2018; Mills, Donnadieu and Goddéris, 2021; Merdith *et al.*, 2025), but that CO_2, and consequently temperature and paleo ice line predictions are still seen to be strongly dependent on external forcings, such as degassing rates. The inclusion of carbonate chemistry has also allowed us to produce a new, detailed, continuous Phanerozoic pH record. Our revised atmospheric O_2 estimates reinforce the notion of low levels in the earliest Paleozoic with a two-step oxygenation event across the Silurian – Devonian (Lenton *et al.*, 2016; Krause *et al.*, 2018; Lenton, Daines and Mills, 2018). The ocean echoes this trend in O_2 with low levels in the early Paleozoic and a rise in the Ordovician, which is partly dependent on atmospheric O_2 levels, but is also a product of strong P recycling and not being constrained by a whole ocean anoxia forcing, as is in COPSE and SCION. While, from the Mesozoic onwards, although all ocean boxes are oxic, deeper margin waters are prone to be less well oxygenated than other areas of the ocean. Our sulfate record indicates that concentrations were lower than modelled by SCION (Mills, Donnadieu and Goddéris, 2021), and are more in line with proxy records (Algeo *et al.*, 2015; Weldeghebriel *et al.*, 2022) and isotope mass balance modelling (Krause *et al.*, 2024), but these are controlled by an external forcing – the concentration of Ca in the ocean – rather than by internal modelling processes.

There are still advances required of the model and its predictions, particularly with regards to resolving model-proxy mismatches for extreme climate events, such as the Hirnantian glaciation, and the hothouses of the Permo-Triassic, Early Cretaceous, and Paleocene–Eocene. The paleo ice line, in particular, is not being captured accurately, but to do this may require another jump in complexity by coupling to a model which incorporates ice sheet modelling and a snow line. We have made suggestions throughout as to how the model could be improved upon by either adding in other biogeochemical

cycles or by updating model forcings; and we have also highlighted some examples where SCION-AMMONITE can be used for hypothesis testing that could not be done in SCION alone.

Acknowledgements

AJK and BJWM were funded by UKRI project EP/Y008790/1. ASM and BJWM were funded by NERC project NE/X011208/1. ASM was funded by ARC DECRA Fellowship DE230101642. BJWM was funded by UKRI project NE/Z000122/1.

Author contributions

AJK wrote the AMMONITE model code, with contributions from the CHEES model code by MZ, and the way it is coupled to SCION. AJK wrote the text and BJWM drew the figures of the first draft, and all authors reviewed and revised the paper.

Code availability

The SCION-AMMONITE model is written in MATLAB and is available at [code files attached for reviewers, will be hosted online in a public repository if published].

References

Ahm, A.-S.C. *et al.* (2018) 'Quantifying early marine diagenesis in shallow-water carbonate sediments', *Geochimica et Cosmochimica Acta*, 236, pp. 140–159. Available at: https://doi.org/10.1016/j.gca.2018.02.042.

Alcott, L.J. *et al.* (2024) 'Crustal carbonate build-up as a driver for Earth's oxygenation', *Nature Geoscience*, 17(5), pp. 458–464. Available at: https://doi.org/10.1038/s41561-024-01417-1.

Algeo, T.J. *et al.* (2015) 'Reconstruction of secular variation in seawater sulfate concentrations', *Biogeosciences*, 12(7), pp. 2131–2151. Available at: https://doi.org/10.5194/bg-12-2131-2015.

Archer, D.E. and Johnson, K. (2000) 'A model of the iron cycle in the ocean', *Global Biogeochemical Cycles*, 14(1), pp. 269–279. Available at: https://doi.org/10.1029/1999GB900053.

1344 Arvidson, R.S., Mackenzie, F.T. and Guidry, M.W. (2006) 'MAGic: A Phanerozoic Model for the
1345 Geochemical Cycling of Major Rock-Forming Components', *American Journal of Science*, 306(3), pp.
1346 135–190. Available at: https://doi.org/10.2475/ajs.306.3.135.

1347 Arvidson, R.S., Mackenzie, F.T. and Guidry, M.W. (2013) 'Geologic history of seawater: A MAGic
1348 approach to carbon chemistry and ocean ventilation', *Chemical Geology*, 362, pp. 287–304. Available
1349 at: https://doi.org/10.1016/j.chemgeo.2013.10.012.

1350 Belcher, C.M., Collinson, M.E. and Scott, A.C. (2013) 'A 450-Million-Year History of Fire', in C.M.
1351 Belcher (ed.) *Fire Phenomena and the Earth System*. 1st edn. Wiley, pp. 229–249. Available at:
1352 https://doi.org/10.1002/9781118529539.ch12.

1353 Belcher, C.M. and McElwain, J.C. (2008) 'Limits for Combustion in Low O_2 Redefine
1354 Paleoatmospheric Predictions for the Mesozoic', *Science*, 321(5893), pp. 1197–1200. Available at:
1355 https://doi.org/10.1126/science.1160978.

1356 Bergman, N.M. (2004) 'COPSE: A new model of biogeochemical cycling over Phanerozoic time',
1357 *American Journal of Science*, 304(5), pp. 397–437. Available at: https://doi.org/10.2475/ajs.304.5.397.

1358 Berner, R.A. (1982) 'Burial of organic carbon and pyrite sulfur in the modern ocean; its geochemical
1359 and environmental significance', *American Journal of Science*, 282(4), pp. 451–473. Available at:
1360 https://doi.org/10.2475/ajs.282.4.451.

1361 Berner, R.A. (1984) 'Sedimentary pyrite formation: An update', *Geochimica et Cosmochimica Acta*,
1362 48(4), pp. 605–615. Available at: https://doi.org/10.1016/0016-7037(84)90089-9.

1363 Berner, R.A. (1987) 'Models for carbon and sulfur cycles and atmospheric oxygen; application to
1364 Paleozoic geologic history', *American Journal of Science*, 287(3), pp. 177–196. Available at:
1365 https://doi.org/10.2475/ajs.287.3.177.

1366 Berner, R.A. (1991) 'A model for atmospheric CO_2 over Phanerozoic time', *American Journal of*
1367 *Science*, 291(4), pp. 339–376. Available at: https://doi.org/10.2475/ajs.291.4.339.

1368 Berner, R.A. (1994) 'GEOCARB II; a revised model of atmospheric CO_2 over Phanerozoic time',
1369 *American Journal of Science*, 294(1), pp. 56–91. Available at: https://doi.org/10.2475/ajs.294.1.56.

1370 Berner, R.A. (2004) 'A model for calcium, magnesium and sulfate in seawater over Phanerozoic time',
1371 *American Journal of Science*, 304(5), pp. 438–453. Available at: https://doi.org/10.2475/ajs.304.5.438.

1372 Berner, R.A. (2006a) 'GEOCARBSULF: A combined model for Phanerozoic atmospheric O_2 and CO_2',
1373 *Geochimica et Cosmochimica Acta*, 70(23), pp. 5653–5664. Available at:
1374 https://doi.org/10.1016/j.gca.2005.11.032.

1375 Berner, R.A. (2006b) 'Inclusion of the Weathering of Volcanic Rocks in the GEOCARBSULF Model',
1376 *American Journal of Science*, 306(5), pp. 295–302. Available at: https://doi.org/10.2475/05.2006.01.

1377 Berner, R.A. (2008) 'Addendum to "Inclusion of the Weathering of Volcanic Rocks in the
1378 GEOCARBSULF Model": (R. A. Berner, 2006, V. 306, p. 295-302).', *American Journal of Science*,
1379 308(1), pp. 100–103. Available at: https://doi.org/10.2475/01.2008.04.

1380 Berner, R.A. (2009) 'Phanerozoic atmospheric oxygen: New results using the GEOCARBSULF
1381 model', *American Journal of Science*, 309(7), pp. 603–606. Available at:
1382 https://doi.org/10.2475/07.2009.03.

Berner, R.A. and Kothavala, Z. (2001) 'GEOCARB III: A revised model of atmospheric CO_2 over Phanerozoic time', *American Journal of Science*, 301(2), pp. 182–204. Available at: https://doi.org/10.2475/ajs.301.2.182.

Bethke, C.M. (2021) *Geochemical and Biogeochemical Reaction Modeling*. 3rd edn. Cambridge University Press. Available at: https://doi.org/10.1017/9781108807005.

Black, E.E. *et al.* (2020) 'Ironing Out Fe Residence Time in the Dynamic Upper Ocean', *Global Biogeochemical Cycles*, 34(9), p. e2020GB006592. Available at: https://doi.org/10.1029/2020GB006592.

Bolton, E.W., Berner, R.A. and Petsch, S.T. (2006) 'The Weathering of Sedimentary Organic Matter as a Control on Atmospheric O_2: II. Theoretical Modeling', *American Journal of Science*, 306(8), pp. 575–615. Available at: https://doi.org/10.2475/08.2006.01.

Bradley, J.A. *et al.* (2022) 'Transfer efficiency of organic carbon in marine sediments', *Nature Communications*, 13(1), p. 7297. Available at: https://doi.org/10.1038/s41467-022-35112-9.

Broecker, W.S. and Peng, T.-H. (1982) *Tracers in the Sea*. New York: Lamont-Doherty Geological Observatory, Columbia University.

Burton, E.A. and Walter, L.M. (1987) 'Relative precipitation rates of aragonite and Mg calcite from seawater: Temperature or carbonate ion control?', *Geology*, 15(2), p. 111. Available at: https://doi.org/10.1130/0091-7613(1987)15%3C111:RPROAA%3E2.0.CO;2.

Cai, C. *et al.* (2022) 'Significant fluctuation in the global sulfate reservoir and oceanic redox state during the Late Devonian event', *PNAS Nexus*. Edited by K.E. Nelson, 1(4), p. pgac122. Available at: https://doi.org/10.1093/pnasnexus/pgac122.

Caldeira, K. and Kasting, J.F. (1992) 'The life span of the biosphere revisited', *Nature*, 360(6406), pp. 721–723. Available at: https://doi.org/10.1038/360721a0.

Caldeira, K. and Rampino, M.R. (1993) 'Aftermath of the end-Cretaceous mass extinction: Possible biogeochemical stabilization of the carbon cycle and climate', *Paleoceanography*, 8(4), pp. 515–525. Available at: https://doi.org/10.1029/93PA01163.

Canfield, D.E. (1998) 'A new model for Proterozoic ocean chemistry', *Nature*, 396(6710), pp. 450–453. Available at: https://doi.org/10.1038/24839.

Canfield, D.E. (2004) 'The evolution of the Earth surface sulfur reservoir', *American Journal of Science*, 304(10), pp. 839–861. Available at: https://doi.org/10.2475/ajs.304.10.839.

Canfield, D.E. and Farquhar, J. (2009) 'Animal evolution, bioturbation, and the sulfate concentration of the oceans', *Proceedings of the National Academy of Sciences*, 106(20), pp. 8123–8127. Available at: https://doi.org/10.1073/pnas.0902037106.

Canfield, D.E. and Kraft, B. (2022) 'The "oxygen" in oxygen minimum zones', *Environmental Microbiology*, 24(11), pp. 5332–5344. Available at: https://doi.org/10.1111/1462-2920.16192.

Chen, Z. *et al.* (2022) 'Organic carbon remineralization rate in global marine sediments: A review', *Regional Studies in Marine Science*, 49, p. 102112. Available at: https://doi.org/10.1016/j.rsma.2021.102112.

Costello, M.J., Smith, M. and Fraczek, W. (2015) 'Correction to Surface Area and the Seabed Area, Volume, Depth, Slope, and Topographic Variation for the World's Seas, Oceans, and Countries',

Environmental Science & Technology, 49(11), pp. 7071–7072. Available at: https://doi.org/10.1021/acs.est.5b01942.

Curtis, C.D. (1977) 'Geochemistry: Sedimentary geochemistry: environments and processes dominated by involvement of an aqueous phase', *Philosophical Transactions of the Royal Society of London. Series A, Mathematical and Physical Sciences*, 286(1336), pp. 353–372. Available at: https://doi.org/10.1098/rsta.1977.0123.

Cutter, G.A. and Krahforst, C.F. (1988) 'Sulfide in surface waters of the western Atlantic Ocean', *Geophysical Research Letters*, 15(12), pp. 1393–1396. Available at: https://doi.org/10.1029/GL015i012p01393.

Cutter, G.A. and Oatts, T.J. (1987) 'Determination of dissolved sulfide and sedimentary sulfur speciation using gas chromatography-photoionization detection', *Analytical Chemistry*, 59(5), pp. 717–721. Available at: https://doi.org/10.1021/ac00132a008.

Dahl, T.W. *et al.* (2010) 'Devonian rise in atmospheric oxygen correlated to the radiations of terrestrial plants and large predatory fish', *Proceedings of the National Academy of Sciences*, 107(42), pp. 17911–17915. Available at: https://doi.org/10.1073/pnas.1011287107.

Daines, S.J., Mills, B.J.W. and Lenton, T.M. (2017) 'Atmospheric oxygen regulation at low Proterozoic levels by incomplete oxidative weathering of sedimentary organic carbon', *Nature Communications*, 8(1), p. 14379. Available at: https://doi.org/10.1038/ncomms14379.

Dal Corso, J. *et al.* (2020) 'Permo–Triassic boundary carbon and mercury cycling linked to terrestrial ecosystem collapse', *Nature Communications*, 11(1), p. 2962. Available at: https://doi.org/10.1038/s41467-020-16725-4.

Dickson, A.G. (1984) 'pH scales and proton-transfer reactions in saline media such as sea water', *Geochimica et Cosmochimica Acta*, 48(11), pp. 2299–2308. Available at: https://doi.org/10.1016/0016-7037(84)90225-4.

Dickson, A.G. (1993) 'The measurement of sea water pH', *Marine Chemistry*, 44(2–4), pp. 131–142. Available at: https://doi.org/10.1016/0304-4203(93)90198-W.

Dickson, A.G. (2010) 'The carbon dioxide system in seawater: equilibrium chemistry and measurements', in U. Riebsell et al. (eds) *Guide to best practices for ocean acidification research and data reporting*. Luxembourg: Publications Office of the European Union.

Donnadieu, Y. *et al.* (2004) 'A "snowball Earth" climate triggered by continental break-up through changes in runoff', *Nature*, 428(6980), pp. 303–306. Available at: https://doi.org/10.1038/nature02408.

Dunlea, A.G. *et al.* (2017) 'Cenozoic global cooling and increased seawater Mg/Ca via reduced reverse weathering', *Nature Communications*, 8(1), p. 844. Available at: https://doi.org/10.1038/s41467-017-00853-5.

Emerson, S. and Hedges, J. (2008) *Chemical oceanography and the marine carbon cycle*. Cambridge: Cambridge University Press.

Emerson, S. and Hedges, J.I. (1988) 'Processes controlling the organic carbon content of open ocean sediments', *Paleoceanography*, 3(5), pp. 621–634. Available at: https://doi.org/10.1029/PA003i005p00621.

Fabry, V.J. *et al.* (2008) 'Impacts of ocean acidification on marine fauna and ecosystem processes', *ICES Journal of Marine Science*, 65(3), pp. 414–432. Available at: https://doi.org/10.1093/icesjms/fsn048.

Farkaš, J. *et al.* (2007) 'Calcium isotope record of Phanerozoic oceans: Implications for chemical evolution of seawater and its causative mechanisms', *Geochimica et Cosmochimica Acta*, 71(21), pp. 5117–5134. Available at: https://doi.org/10.1016/j.gca.2007.09.004.

Feely, R.A. *et al.* (2004) 'Impact of Anthropogenic CO_2 on the $CaCO_3$ System in the Oceans', *Science*, 305(5682), pp. 362–366. Available at: https://doi.org/10.1126/science.1097329.

Feng, K. *et al.* (2025) 'Persistent dysoxia in very shallow seas across the late Cambrian SPICE event, Durness Group, UK', *Geology*, 53(8), pp. 642–646. Available at: https://doi.org/https://doi.org/10.1130/GEOL.S.28851395.

Fike, D.A., Bradley, A.S. and Rose, C.V. (2015) 'Rethinking the Ancient Sulfur Cycle', *Annual Review of Earth and Planetary Sciences*, 43(1), pp. 593–622. Available at: https://doi.org/10.1146/annurev-earth-060313-054802.

Foster, G.L., Royer, D.L. and Lunt, D.J. (2017) 'Future climate forcing potentially without precedent in the last 420 million years', *Nature Communications*, 8(1), p. 14845. Available at: https://doi.org/10.1038/ncomms14845.

Friedrich, T. *et al.* (2012) 'Detecting regional anthropogenic trends in ocean acidification against natural variability', *Nature Climate Change*, 2(3), pp. 167–171. Available at: https://doi.org/10.1038/nclimate1372.

Froelich, P.N. *et al.* (1979) 'Early oxidation of organic matter in pelagic sediments of the eastern equatorial Atlantic: suboxic diagenesis', *Geochimica et Cosmochimica Acta*, 43(7), pp. 1075–1090. Available at: https://doi.org/10.1016/0016-7037(79)90095-4.

Froelich, P.N. *et al.* (1982) 'The marine phosphorus cycle', *American Journal of Science*, 282(4), pp. 474–511. Available at: https://doi.org/10.2475/ajs.282.4.474.

Gehlen, M. *et al.* (2007) 'The fate of pelagic $CaCO_3$ production in a high CO_2 ocean: a model study'.

Gill, B.C. *et al.* (2011) 'Geochemical evidence for widespread euxinia in the Later Cambrian ocean', *Nature*, 469(7328), pp. 80–83. Available at: https://doi.org/10.1038/nature09700.

Gill, B.C., Lyons, T.W. and Saltzman, M.R. (2007) 'Parallel, high-resolution carbon and sulfur isotope records of the evolving Paleozoic marine sulfur reservoir', *Palaeogeography, Palaeoclimatology, Palaeoecology*, 256(3–4), pp. 156–173. Available at: https://doi.org/10.1016/j.palaeo.2007.02.030.

Glasspool, I.J. *et al.* (2015) 'The impact of fire on the Late Paleozoic Earth system', *Frontiers in Plant Science*, 6. Available at: https://doi.org/10.3389/fpls.2015.00756.

Glasspool, I.J. and Scott, A.C. (2010) 'Phanerozoic concentrations of atmospheric oxygen reconstructed from sedimentary charcoal', *Nature Geoscience*, 3(9), pp. 627–630. Available at: https://doi.org/10.1038/ngeo923.

Gledhill, M. and Buck, K.N. (2012) 'The organic complexation of iron in the marine environment: a review', *Frontiers in Microbiology*, 3(69). Available at: https://doi.org/10.3389/fmicb.2012.00069.

Grengs, A. *et al.* (2024) 'Direct precipitation of siderite in ferruginous environments', *Geochemical Perspectives Letters*, 30, pp. 1–6. Available at: https://doi.org/10.7185/geochemlet.2414.

Gu, X. *et al.* (2020) 'Deep abiotic weathering of pyrite', *Science*, 370(6515), p. eabb8092. Available at: https://doi.org/10.1126/science.abb8092.

Gurung, K. *et al.* (2022) 'Climate windows of opportunity for plant expansion during the Phanerozoic', *Nature Communications*, 13(1), p. 4530. Available at: https://doi.org/10.1038/s41467-022-32077-7.

Gurung, K. *et al.* (2024) 'Geographic range of plants drives long-term climate change', *Nature Communications*, 15(1), p. 1805. Available at: https://doi.org/10.1038/s41467-024-46105-1.

Halevy, I. and Bachan, A. (2017) 'The geologic history of seawater pH', *Science*, 355(6329), pp. 1069–1071. Available at: https://doi.org/10.1126/science.aal4151.

Hansen, K.W. and Wallmann, K. (2003) 'Cretaceous and Cenozoic evolution of seawater composition, atmospheric O_2 and CO_2: A model perspective', *American Journal of Science*, 303(2), pp. 94–148. Available at: https://doi.org/10.2475/ajs.303.2.94.

Hayes, J.M. and Waldbauer, J.R. (2006) 'The carbon cycle and associated redox processes through time', *Philosophical Transactions of the Royal Society B: Biological Sciences*, 361(1470), pp. 931–950. Available at: https://doi.org/10.1098/rstb.2006.1840.

He, T. *et al.* (2019) 'Possible links between extreme oxygen perturbations and the Cambrian radiation of animals', *Nature Geoscience*, 12(6), pp. 468–474. Available at: https://doi.org/10.1038/s41561-019-0357-z.

Hedges, J.I. and Keil, R.G. (1995) 'Sedimentary organic matter preservation: an assessment and speculative synthesis', *Marine Chemistry*, 49(2–3), pp. 81–115. Available at: https://doi.org/10.1016/0304-4203(95)00008-F.

Henehan, M.J. *et al.* (2020) 'Revisiting the Middle Eocene Climatic Optimum "Carbon Cycle Conundrum" With New Estimates of Atmospheric pCO_2 From Boron Isotopes', *Paleoceanography and Paleoclimatology*, 35(6), p. e2019PA003713. Available at: https://doi.org/10.1029/2019PA003713.

Hoegh-Guldberg, O. *et al.* (2017) 'Coral Reef Ecosystems under Climate Change and Ocean Acidification', *Frontiers in Marine Science*, 4, p. 158. Available at: https://doi.org/10.3389/fmars.2017.00158.

Holland, H.D. (1984) *The Chemical Evolution of the Atmosphere and Oceans*. Princeton University Press. Available at: https://doi.org/10.2307/j.ctv15r58kg.

Hopwood, M.J. *et al.* (2020) 'Fe(II) stability in coastal seawater during experiments in Patagonia, Svalbard, and Gran Canaria', *Biogeosciences*, 17(5), pp. 1327–1342. Available at: https://doi.org/10.5194/bg-17-1327-2020.

Horne, J.E. and Goldblatt, C. (2024) 'EONS: A New Biogeochemical Model of Earth's Oxygen, Carbon, Phosphorus, and Nitrogen Systems From the Archean to the Present', *Geochemistry, Geophysics, Geosystems*, 25(4), p. e2023GC011252. Available at: https://doi.org/10.1029/2023GC011252.

Hurtgen, M.T., Pruss, S.B. and Knoll, A.H. (2009) 'Evaluating the relationship between the carbon and sulfur cycles in the later Cambrian ocean: An example from the Port au Port Group, western Newfoundland, Canada', *Earth and Planetary Science Letters*, 281(3–4), pp. 288–297. Available at: https://doi.org/10.1016/j.epsl.2009.02.033.

1541 Husson, J.M. and Peters, S.E. (2026) 'Shifting carbonate burial between oceanic and continental crust
1542 across Earth history', *Earth and Planetary Science Letters*, 677, p. 119810. Available at:
1543 https://doi.org/10.1016/j.epsl.2025.119810.

1544 Irwin, H., Curtis, C. and Coleman, M. (1977) 'Isotopic evidence for source of diagenetic carbonates
1545 formed during burial of organic-rich sediments', *Nature*, 269(5625), pp. 209–213. Available at:
1546 https://doi.org/10.1038/269209a0.

1547 Isson, T.T. and Planavsky, N.J. (2018) 'Reverse weathering as a long-term stabilizer of marine pH and
1548 planetary climate', *Nature*, 560(7719), pp. 471–475. Available at: https://doi.org/10.1038/s41586-018-
1549 0408-4.

1550 Judd, E.J. *et al.* (2024) 'A 485-million-year history of Earth's surface temperature', *Science*, 385(6715),
1551 p. eadk3705. Available at: https://doi.org/10.1126/science.adk3705.

1552 Jurikova, H. *et al.* (2025) 'Rapid rise in atmospheric CO_2 marked the end of the Late Palaeozoic Ice
1553 Age', *Nature Geoscience*, 18(1), pp. 91–97. Available at: https://doi.org/10.1038/s41561-024-01610-2.

1554 Kah, L.C., Lyons, T.W. and Frank, T.D. (2004) 'Low marine sulphate and protracted oxygenation of
1555 the Proterozoic biosphere', *Nature*, 431(7010), pp. 834–838. Available at:
1556 https://doi.org/10.1038/nature02974.

1557 Kanzaki, Y. and Kump, L.R. (2017) 'Biotic effects on oxygen consumption during weathering:
1558 Implications for the second rise of oxygen', *Geology*, 45(7), pp. 611–614. Available at:
1559 https://doi.org/10.1130/G38869.1.

1560 Kemeny, P.C., Krause, A. and Kump, L. (2025) 'A Historical Perspective on Long-Term Global
1561 Biogeochemical Box Models', in L.A. Coogan et al. (eds) *Geophysical Monograph Series*. 1st edn.
1562 Wiley, pp. 263–295. Available at: https://doi.org/10.1002/9781394229185.ch12.

1563 Konhauser, K.O. *et al.* (2017) 'Iron formations: A global record of Neoarchaean to Palaeoproterozoic
1564 environmental history', *Earth-Science Reviews*, 172, pp. 140–177. Available at:
1565 https://doi.org/10.1016/j.earscirev.2017.06.012.

1566 Kozik, N.P. *et al.* (2022) 'Geochemical Records Reveal Protracted and Differential Marine Redox
1567 Change Associated With Late Ordovician Climate and Mass Extinctions', *AGU Advances*, 3(1), p.
1568 e2021AV000563. Available at: https://doi.org/10.1029/2021AV000563.

1569 Krause, A.J. *et al.* (2018) 'Stepwise oxygenation of the Paleozoic atmosphere', *Nature*
1570 *Communications*, 9(1), p. 4081. Available at: https://doi.org/10.1038/s41467-018-06383-y.

1571 Krause, A.J. *et al.* (2022) 'Extreme variability in atmospheric oxygen levels in the late Precambrian',
1572 *Science Advances*, 8(41), p. eabm8191. Available at: https://doi.org/10.1126/sciadv.abm8191.

1573 Krause, A.J. *et al.* (2023) 'Enhanced clay formation key in sustaining the Middle Eocene Climatic
1574 Optimum', *Nature Geoscience*, 16(8), pp. 730–738. Available at: https://doi.org/10.1038/s41561-023-
1575 01234-y.

1576 Krause, A.J. *et al.* (2024) 'Modelling sulfate concentrations in the global ocean through Phanerozoic
1577 time', *Journal of the Geological Society*, 181(4), pp. jgs2023-184. Available at:
1578 https://doi.org/10.1144/jgs2023-184.

1579 Krissansen-Totton, J., Arney, G.N. and Catling, D.C. (2018) 'Constraining the climate and ocean pH
1580 of the early Earth with a geological carbon cycle model', *Proceedings of the National Academy of*
1581 *Sciences*, 115(16), pp. 4105–4110. Available at: https://doi.org/10.1073/pnas.1721296115.

Krissansen-Totton, J., Kipp, M.A. and Catling, D.C. (2021) 'Carbon cycle inverse modeling suggests large changes in fractional organic burial are consistent with the carbon isotope record and may have contributed to the rise of oxygen', *Geobiology*, 19(4), pp. 342–363. Available at: https://doi.org/10.1111/gbi.12440.

Krumins, V. *et al.* (2013) 'Dissolved inorganic carbon and alkalinity fluxes from coastal marine sediments: model estimates for different shelf environments and sensitivity to global change', *Biogeosciences*, 10(1), pp. 371–398. Available at: https://doi.org/10.5194/bg-10-371-2013.

Kukla, T. *et al.* (2023) 'All aboard! Earth system investigations with the CH2O-CHOO TRAIN v1.0', *Geoscientific Model Development*, 16(19), pp. 5515–5538. Available at: https://doi.org/10.5194/gmd-16-5515-2023.

Kwiecinski, J.V. and Babbin, A.R. (2021) 'A High-Resolution Atlas of the Eastern Tropical Pacific Oxygen Deficient Zones', *Global Biogeochemical Cycles*, 35(12), p. e2021GB007001. Available at: https://doi.org/10.1029/2021GB007001.

LaRowe, D.E. *et al.* (2020) 'The fate of organic carbon in marine sediments - New insights from recent data and analysis', *Earth-Science Reviews*, 204, p. 103146. Available at: https://doi.org/10.1016/j.earscirev.2020.103146.

Lee, C.-T.A. *et al.* (2016) 'Two-step rise of atmospheric oxygen linked to the growth of continents', *Nature Geoscience*, 9(6), pp. 417–424. Available at: https://doi.org/10.1038/ngeo2707.

Lefèvre, N. and Watson, A.J. (1999) 'Modeling the geochemical cycle of iron in the oceans and its impact on atmospheric CO_2 concentrations', *Global Biogeochemical Cycles*, 13(3), pp. 727–736. Available at: https://doi.org/10.1029/1999GB900034.

Lenton, T.M. *et al.* (2016) 'Earliest land plants created modern levels of atmospheric oxygen', *Proceedings of the National Academy of Sciences*, 113(35), pp. 9704–9709. Available at: https://doi.org/10.1073/pnas.1604787113.

Lenton, T.M., Daines, S.J. and Mills, B.J.W. (2018) 'COPSE reloaded: An improved model of biogeochemical cycling over Phanerozoic time', *Earth-Science Reviews*, 178, pp. 1–28. Available at: https://doi.org/10.1016/j.earscirev.2017.12.004.

Liu, X.-M. *et al.* (2021) 'A persistently low level of atmospheric oxygen in Earth's middle age', *Nature Communications*, 12(1), p. 351. Available at: https://doi.org/10.1038/s41467-020-20484-7.

Lowenstein, T.K., Kendall, B. and Anbar, A.D. (2014) 'The Geologic History of Seawater', *Treatise on Geochemistry*. Elsevier, pp. 569–622. Available at: https://doi.org/10.1016/B978-0-08-095975-7.00621-5.

Loyd, S.J. *et al.* (2012) 'Sustained low marine sulfate concentrations from the Neoproterozoic to the Cambrian: Insights from carbonates of northwestern Mexico and eastern California', *Earth and Planetary Science Letters*, 339–340, pp. 79–94. Available at: https://doi.org/10.1016/j.epsl.2012.05.032.

Lueker, T.J., Dickson, A.G. and Keeling, C.D. (2000) 'Ocean pCO_2 calculated from dissolved inorganic carbon, alkalinity, and equations for K_1 and K_2: validation based on laboratory measurements of CO_2 in gas and seawater at equilibrium', *Marine Chemistry*, 70(1–3), pp. 105–119. Available at: https://doi.org/10.1016/S0304-4203(00)00022-0.

Lyons, T.W. *et al.* (2024) 'Co-evolution of early Earth environments and microbial life', *Nature Reviews Microbiology*, 22(9), pp. 572–586. Available at: https://doi.org/10.1038/s41579-024-01044-y.

Maffre, P. *et al.* (2018) 'Mountain ranges, climate and weathering. Do orogens strengthen or weaken the silicate weathering carbon sink?', *Earth and Planetary Science Letters*, 493, pp. 174–185. Available at: https://doi.org/10.1016/j.epsl.2018.04.034.

Maffre, P. *et al.* (2025) 'GEOCLIM7, an Earth system model for multi-million-year evolution of the geochemical cycles and climate', *Geoscientific Model Development*, 18(18), pp. 6367–6413. Available at: https://doi.org/10.5194/gmd-18-6367-2025.

Mehrbach, C. *et al.* (1973) 'Measurement of the Apparent Dissociation Constants of Carbonic Acid in Seawater at Atmospheric Pressure', *Limnology and Oceanography*, 18(6), pp. 897–907. Available at: https://doi.org/10.4319/lo.1973.18.6.0897.

Merdith, A.S. *et al.* (2025) 'Phanerozoic icehouse climates as the result of multiple solid-Earth cooling mechanisms', *Science Advances*, 11(7), p. eadm9798. Available at: https://doi.org/10.1126/sciadv.adm9798.

Mertens, C., Paradis, S. and Hemingway, J.D. (2026) 'Sedimentary conditions drive modern pyrite burial flux to exceed oxidation', *Nature Geoscience*, 19(1), pp. 99–105. Available at: https://doi.org/10.1038/s41561-025-01855-5.

Middelburg, J.J. (2019) 'Carbon Processing at the Seafloor', in J. J. Middelburg, *Marine Carbon Biogeochemistry*. Cham: Springer International Publishing (SpringerBriefs in Earth System Sciences), pp. 57–75. Available at: https://doi.org/10.1007/978-3-030-10822-9_4.

Millero, F.J. (2010) 'Carbonate constants for estuarine waters', *Marine and Freshwater Research*, 61(2), pp. 139–142. Available at: https://doi.org/10.1071/MF09254.

Mills, B., Daines, S.J. and Lenton, T.M. (2014) 'Changing tectonic controls on the long-term carbon cycle from Mesozoic to present', *Geochemistry, Geophysics, Geosystems*, 15(12), pp. 4866–4884. Available at: https://doi.org/10.1002/2014GC005530.

Mills, B.J.W. *et al.* (2023) 'Evolution of Atmospheric O_2 Through the Phanerozoic, Revisited', *Annual Review of Earth and Planetary Sciences*, 51(1), pp. 253–276. Available at: https://doi.org/10.1146/annurev-earth-032320-095425.

Mills, B.J.W. *et al.* (2025) 'Exploring Neoproterozoic climate and biogeochemical evolution in the SCION model', *Global and Planetary Change*, 249, p. 104791. Available at: https://doi.org/10.1016/j.gloplacha.2025.104791.

Mills, B.J.W., Donnadieu, Y. and Goddéris, Y. (2021) 'Spatial continuous integration of Phanerozoic global biogeochemistry and climate', *Gondwana Research*, 100, pp. 73–86. Available at: https://doi.org/10.1016/j.gr.2021.02.011.

Moore, C.M. *et al.* (2013) 'Processes and patterns of oceanic nutrient limitation', *Nature Geoscience*, 6(9), pp. 701–710. Available at: https://doi.org/10.1038/ngeo1765.

Müller, R.D. *et al.* (2022) 'Evolution of Earth's tectonic carbon conveyor belt', *Nature*, 605(7911), pp. 629–639. Available at: https://doi.org/10.1038/s41586-022-04420-x.

Müller, R.D. *et al.* (2024) 'Solid Earth Carbon Degassing and Sequestration Since 1 Billion Years Ago', *Geochemistry, Geophysics, Geosystems*, 25(11), p. e2024GC011713. Available at: https://doi.org/10.1029/2024GC011713.

Munkes, B., Löptien, U. and Dietze, H. (2021) 'Cyanobacteria blooms in the Baltic Sea: a review of models and facts', *Biogeosciences*, 18(7), pp. 2347–2378. Available at: https://doi.org/10.5194/bg-18-2347-2021.

Ohmoto, H., Watanabe, Y. and Kumazawa, K. (2004) 'Evidence from massive siderite beds for a CO_2-rich atmosphere before ~1.8 billion years ago', *Nature*, 429(6990), pp. 395–399. Available at: https://doi.org/10.1038/nature02573.

O'Mara, N.A. and Dunne, J.P. (2019) 'Hot Spots of Carbon and Alkalinity Cycling in the Coastal Oceans', *Scientific Reports*, 9(1), p. 4434. Available at: https://doi.org/10.1038/s41598-019-41064-w.

Opdyke, B.N. and Wilkinson, B.H. (1993) 'Carbonate mineral saturation state and cratonic limestone accumulation', *American Journal of Science*, 293(3), pp. 217–234. Available at: https://doi.org/10.2475/ajs.293.3.217.

Ozaki, K. *et al.* (2022) 'CANOPS-GRB v1.0: a new Earth system model for simulating the evolution of ocean–atmosphere chemistry over geologic timescales', *Geoscientific Model Development*, 15(20), pp. 7593–7639. Available at: https://doi.org/10.5194/gmd-15-7593-2022.

Parekh, P., Follows, M.J. and Boyle, E.A. (2005) 'Decoupling of iron and phosphate in the global ocean', *Global Biogeochemical Cycles*, 19(2), p. 2004GB002280. Available at: https://doi.org/10.1029/2004GB002280.

Parker, M.S., Mock, T. and Armbrust, E.V. (2008) 'Genomic Insights into Marine Microalgae', *Annual Review of Genetics*, 42(1), pp. 619–645. Available at: https://doi.org/10.1146/annurev.genet.42.110807.091417.

Pawlowski, J. *et al.* (2003) 'The evolution of early Foraminifera', *Proceedings of the National Academy of Sciences*, 100(20), pp. 11494–11498. Available at: https://doi.org/10.1073/pnas.2035132100.

Pohl, A. *et al.* (2022) 'Continental configuration controls ocean oxygenation during the Phanerozoic', *Nature*, 608(7923), pp. 523–527. Available at: https://doi.org/10.1038/s41586-022-05018-z.

Poulton, S.W. (2003) 'Sulfide oxidation and iron dissolution kinetics during the reaction of dissolved sulfide with ferrihydrite', *Chemical Geology*, 202(1–2), pp. 79–94. Available at: https://doi.org/10.1016/S0009-2541(03)00237-7.

Qiu, R. *et al.* (2025) 'Pulsed biogenic methane emissions coupled with episodic warming during the Toarcian Oceanic Anoxic Event', *Proceedings of the National Academy of Sciences*, 122(36), p. e2423598122. Available at: https://doi.org/10.1073/pnas.2423598122.

Rae, J.W.B. *et al.* (2021) 'Atmospheric CO_2 over the Past 66 Million Years from Marine Archives', *Annual Review of Earth and Planetary Sciences*, 49(1), pp. 609–641. Available at: https://doi.org/10.1146/annurev-earth-082420-063026.

Rahman, S. and Trower, E.J. (2026) 'The Fate of Ocean Alkalinity: Carbonate Formation and Reverse Weathering Reactions', *Elements*, 22(1), pp. 36–41. Available at: https://doi.org/10.2138/gselements.22.1.36.

Rampino, M.R. and Caldeira, K. (2005) 'Major perturbation of ocean chemistry and a "Strangelove Ocean" after the end-Permian mass extinction', *Terra Nova*, 17(6), pp. 554–559. Available at: https://doi.org/10.1111/j.1365-3121.2005.00648.x.

Rassmann, J. *et al.* (2020) 'Benthic alkalinity and dissolved inorganic carbon fluxes in the Rhône River prodelta generated by decoupled aerobic and anaerobic processes', *Biogeosciences*, 17(1), pp. 13–33. Available at: https://doi.org/10.5194/bg-17-13-2020.

Redfield, A.C. (1958) 'The Biological Control of Chemical Factors in the Environment', *American Scientist*, pp. 205–221.

Reed, D.C., Slomp, C.P. and Gustafsson, B.G. (2011) 'Sedimentary phosphorus dynamics and the evolution of bottom-water hypoxia: A coupled benthic–pelagic model of a coastal system', *Limnology and Oceanography*, 56(3), pp. 1075–1092. Available at: https://doi.org/10.4319/lo.2011.56.3.1075.

Reinhard, C.T. *et al.* (2020) 'Oceanic and atmospheric methane cycling in the cGENIE Earth system model – release v0.9.14', *Geoscientific Model Development*, 13(11), pp. 5687–5706. Available at: https://doi.org/10.5194/gmd-13-5687-2020.

Ridgwell, A. *et al.* (2007) 'Marine geochemical data assimilation in an efficient Earth System Model of global biogeochemical cycling', *Biogeosciences*, 4, pp. 87–104. Available at: https://doi.org/https://doi.org/10.5194/bg-4-87-2007.

Ridgwell, A. and Schmidt, D.N. (2010) 'Past constraints on the vulnerability of marine calcifiers to massive carbon dioxide release', *Nature Geoscience*, 3(3), pp. 196–200. Available at: https://doi.org/10.1038/ngeo755.

Sarmiento, J.L. and Toggweiler, J.R. (1984) 'A new model for the role of the oceans in determining atmospheric pCO_2', *Nature*, 308(5960), pp. 621–624. Available at: https://doi.org/10.1038/308621a0.

Schmittner, A. *et al.* (2008) 'Future changes in climate, ocean circulation, ecosystems, and biogeochemical cycling simulated for a business-as-usual CO_2 emission scenario until year 4000 AD', *Global Biogeochemical Cycles*, 22(1), p. 2007GB002953. Available at: https://doi.org/10.1029/2007GB002953.

Scotese, C.R. *et al.* (2021) 'Phanerozoic paleotemperatures: The earth's changing climate during the last 540 million years', *Earth-Science Reviews*, 215, p. 103503. Available at: https://doi.org/10.1016/j.earscirev.2021.103503.

Shields, G.A. and Mills, B.J.W. (2021) 'Evaporite weathering and deposition as a long-term climate forcing mechanism', *Geology*, 49(3), pp. 299–303. Available at: https://doi.org/10.1130/G48146.1.

Skirrow, G. (1965) 'The dissolved gases - carbon dioxide', in J.P. Riley and G. Skirrow (eds) *Chemical Oceanography*. 1st edn. London: Academic Press, pp. 227–322.

Slomp, C.P. and Van Cappellen, P. (2007) 'The global marine phosphorus cycle: sensitivity to oceanic circulation'.

Sluijs, A. *et al.* (2013) 'A middle Eocene carbon cycle conundrum', *Nature Geoscience*, 6(6), pp. 429–434. Available at: https://doi.org/10.1038/ngeo1807.

Soetaert, K. *et al.* (2007) 'The effect of biogeochemical processes on pH', *Marine Chemistry*, 105(1–2), pp. 30–51. Available at: https://doi.org/10.1016/j.marchem.2006.12.012.

Sperling, E.A. *et al.* (2015) 'Statistical analysis of iron geochemical data suggests limited late Proterozoic oxygenation', *Nature*, 523(7561), pp. 451–454. Available at: https://doi.org/10.1038/nature14589.

Spofforth, D.J.A. *et al.* (2010) 'Organic carbon burial following the middle Eocene climatic optimum in the central western Tethys', *Paleoceanography*, 25(3). Available at: https://doi.org/10.1029/2009PA001738.

Steinthorsdottir, M. *et al.* (2025) 'Phanerozoic atmospheric CO_2 reconstructed with proxies and models: Current understanding and future directions', *Treatise on Geochemistry*. Elsevier, pp. 467–492. Available at: https://doi.org/10.1016/B978-0-323-99762-1.00074-7.

Stockey, R.G. *et al.* (2020) 'Persistent global marine euxinia in the early Silurian', *Nature Communications*, 11(1), p. 1804. Available at: https://doi.org/10.1038/s41467-020-15400-y.

Tagliabue, A. *et al.* (2016) 'How well do global ocean biogeochemistry models simulate dissolved iron distributions?', *Global Biogeochemical Cycles*, 30(2), pp. 149–174. Available at: https://doi.org/10.1002/2015GB005289.

Tagliabue, A., Aumont, O. and Bopp, L. (2014) 'The impact of different external sources of iron on the global carbon cycle', *Geophysical Research Letters*, 41(3), pp. 920–926. Available at: https://doi.org/10.1002/2013GL059059.

Thompson, K.J. *et al.* (2019) 'Photoferrotrophy, deposition of banded iron formations, and methane production in Archean oceans', *Science Advances*, 5(11), p. eaav2869. Available at: https://doi.org/10.1126/sciadv.aav2869.

Toggweiler, J.R. (1999) 'Variation of atmospheric CO_2 by ventilation of the ocean's deepest water', *Paleoceanography*, 14(5), pp. 571–588. Available at: https://doi.org/10.1029/1999PA900033.

Tostevin, R. *et al.* (2019) 'Uranium isotope evidence for an expansion of anoxia in terminal Ediacaran oceans', *Earth and Planetary Science Letters*, 506, pp. 104–112. Available at: https://doi.org/10.1016/j.epsl.2018.10.045.

Tostevin, R. and Mills, B.J.W. (2020) 'Reconciling proxy records and models of Earth's oxygenation during the Neoproterozoic and Palaeozoic', *Interface Focus*, 10(4), p. 20190137. Available at: https://doi.org/10.1098/rsfs.2019.0137.

Tyrrell, T. (1999) 'The relative influences of nitrogen and phosphorus on oceanic primary production', *Nature*, 400(6744), pp. 525–531. Available at: https://doi.org/10.1038/22941.

Tyson, R.V. and Pearson, T.H. (1991) 'Modern and ancient continental shelf anoxia: an overview', *Geological Society, London, Special Publications*, 58(1), pp. 1–24. Available at: https://doi.org/10.1144/GSL.SP.1991.058.01.01.

Van De Velde, S.J. *et al.* (2021) 'Iron and sulfur cycling in the cGENIE.muffin Earth system model (v0.9.21)', *Geoscientific Model Development*, 14(5), pp. 2713–2745. Available at: https://doi.org/10.5194/gmd-14-2713-2021.

Van Der Ploeg, R. *et al.* (2018) 'Middle Eocene greenhouse warming facilitated by diminished weathering feedback', *Nature Communications*, 9(1), p. 2877. Available at: https://doi.org/10.1038/s41467-018-05104-9.

Vaquer-Sunyer, R. and Duarte, C.M. (2008) 'Thresholds of hypoxia for marine biodiversity', *Proceedings of the National Academy of Sciences*, 105(40), pp. 15452–15457. Available at: https://doi.org/10.1073/pnas.0803833105.

Vitali, R. *et al.* (2026) 'Combined effects of photorespiration and fire strongly regulate atmospheric oxygen levels', *Science Advances*, 12(2), pp. 1–14. Available at: https://doi.org/https://doi.org/10.1126/sciadv.ady0542.

Volk, T. (1989) 'Sensitivity of climate and atmospheric CO_2 to deep-ocean and shallow-ocean carbonate burial', *Nature*, 337, pp. 637–640.

Walker, J.C.G., Hays, P.B. and Kasting, J.F. (1981) 'A negative feedback mechanism for the long-term stabilization of Earth's surface temperature', *Journal of Geophysical Research: Oceans*, 86(C10), pp. 9776–9782. Available at: https://doi.org/10.1029/JC086iC10p09776.

Walker, J.C.G. and Kasting, J.F. (1992) 'Effects of fuel and forest conservation on future levels of atmospheric carbon dioxide', *Palaeogeography, Palaeoclimatology, Palaeoecology*, 97(3), pp. 151–189. Available at: https://doi.org/10.1016/0031-0182(92)90207-L.

Wallace, M.W. *et al.* (2017) 'Oxygenation history of the Neoproterozoic to early Phanerozoic and the rise of land plants', *Earth and Planetary Science Letters*, 466, pp. 12–19. Available at: https://doi.org/10.1016/j.epsl.2017.02.046.

Wallmann, K. *et al.* (2019) 'Periodic changes in the Cretaceous ocean and climate caused by marine redox see-saw', *Nature Geoscience*, 12(6), pp. 456–461. Available at: https://doi.org/10.1038/s41561-019-0359-x.

Wang, Y. and Van Cappellen, P. (1996) 'A multicomponent reactive transport model of early diagenesis: Application to redox cycling in coastal marine sediments', *Geochimica et Cosmochimica Acta*, 60(16), pp. 2993–3014. Available at: https://doi.org/10.1016/0016-7037(96)00140-8.

Watson, A.J. (1978) *Consequences for the biosphere of forest and grassland fires*. University of Reading.

Weiss, R.F. (1970) 'The solubility of nitrogen, oxygen and argon in water and seawater', *Deep Sea Research and Oceanographic Abstracts*, 17(4), pp. 721–735. Available at: https://doi.org/10.1016/0011-7471(70)90037-9.

Weldeghebriel, M.F. *et al.* (2022) '[Ca^{2+}] and [SO_4^{2-}] in Phanerozoic and terminal Proterozoic seawater from fluid inclusions in halite: The significance of Ca-SO_4 crossover points', *Earth and Planetary Science Letters*, 594, p. 117712. Available at: https://doi.org/10.1016/j.epsl.2022.117712.

West, A.J. (2012) 'Thickness of the chemical weathering zone and implications for erosional and climatic drivers of weathering and for carbon-cycle feedbacks', *Geology*, 40(9), pp. 811–814. Available at: https://doi.org/10.1130/G33041.1.

Westberry, T.K. *et al.* (2023) 'Atmospheric nourishment of global ocean ecosystems', *Science*, 380(6644), pp. 515–519. Available at: https://doi.org/10.1126/science.abq5252.

Wildman, R.A. *et al.* (2004) 'The weathering of sedimentary organic matter as a control on atmospheric O_2: I. Analysis of a black shale', *American Journal of Science*, 304(3), pp. 234–249. Available at: https://doi.org/10.2475/ajs.304.3.234.

Witkowski, C.R. *et al.* (2018) 'Molecular fossils from phytoplankton reveal secular pCO_2 trend over the Phanerozoic', *Science Advances*, 4(11), p. eaat4556. Available at: https://doi.org/10.1126/sciadv.aat4556.

Wolf-Gladrow, D.A. *et al.* (2007) 'Total alkalinity: The explicit conservative expression and its application to biogeochemical processes', *Marine Chemistry*, 106(1–2), pp. 287–300. Available at: https://doi.org/10.1016/j.marchem.2007.01.006.

Wortmann, U.G. and Paytan, A. (2012) 'Rapid Variability of Seawater Chemistry Over the Past 130 Million Years', *Science*, 337(6092), pp. 334–336. Available at: https://doi.org/10.1126/science.1220656.

Zeebe, R.E. (2012) 'LOSCAR: Long-term Ocean-atmosphere-Sediment CArbon cycle Reservoir Model v2.0.4', *Geoscientific Model Development*, 5(1), pp. 149–166. Available at: https://doi.org/10.5194/gmd-5-149-2012.

Zeebe, R.E. and Westbroek, P. (2003) 'A simple model for the $CaCO_3$ saturation state of the ocean: The "Strangelove," the "Neritan," and the "Cretan" Ocean', *Geochemistry, Geophysics, Geosystems*, 4(12), p. 2003GC000538. Available at: https://doi.org/10.1029/2003GC000538.

Zeebe, R.E. and Wolf-Gladrow, D. (2001) 'Chapter 1 Equilibrium', *CO_2 in seawater: Equilibrium, kinetics, isotopes*. Elsevier (Elsevier Oceanography Series), pp. 1–84. Available at: https://doi.org/10.1016/S0422-9894(01)80002-7.

Zhang, Y. *et al.* (2025) 'Increased Continental Exposure as a Driver of Carbon Drawdown and Initiation of the Late Paleozoic Ice Age', *Geophysical Research Letters*, 52(24), p. e2025GL119356. Available at: https://doi.org/10.1029/2025GL119356.

Zhao, M. *et al.* (2023) 'Oxygenation of the Earth aided by mineral–organic carbon preservation', *Nature Geoscience*, 16(3), pp. 262–267. Available at: https://doi.org/10.1038/s41561-023-01133-2.

Supplementary Information

Phanerozoic atmosphere and ocean conditions estimated by a continuous climate and multi-box ocean model

Alexander J. Krause[a,b*], Mingyu Zhao[c], Andrew S. Merdith[d] and Benjamin J.W. Mills[b]

[a]School of Physical, Chemical and Environmental Sciences, Cardiff University, Main Building, Park Place, Cardiff, CF10 3AT, UK

[b]School of Earth, Environment and Sustainability, University of Leeds, Woodhouse Lane, Leeds, LS2 9JT, UK

[c]State Key Laboratory of Lithospheric and Environmental Coevolution, Institute of Geology and Geophysics, Chinese Academy of Sciences, Beijing 100029, China

[d]School of Physics, Chemistry and Earth Sciences, University of Adelaide, Adelaide, SA, Australia

*Corresponding author: krausea@cardiff.ac.uk

Table S1: Breakdown of other equations making up the carbonate system.

Parameter definition	Equation	Equation number
Henry's law	$k_{0\_x} = e^{h1 + \left(\frac{h2}{T_{100\_x}}\right) + (h3 * \ln T_{100\_x}) + \{sal * [h4 - (h5 * T_{100\_x}) + (h6 * T_{100\_x}^2)]\}}$	(SE1)
First acid dissociation constant for surficial ocean boxes	$k_{1\_x} = 10^{-\left\{\frac{pk_1C1}{T_x(°K)} - pk_1C2 + (pk_1C3 * \ln T_x(°K)) - (pk_1C4 * sal) + (pk_1C5 * sal^2)\right\}}$	(SE2)
Pre-pressure first acid dissociation constant for deeper ocean boxes	$prek_{1\_x} = 10^{-\left\{\frac{pk_1C1}{T_x(°K)} - pk_1C2 + (pk_1C3 * \ln T_x(°K)) - (pk_1C4 * sal) + (pk_1C5 * sal^2)\right\}}$	(SE3)
Second acid dissociation constant for surficial ocean boxes	$k_{2\_x} = 10^{-\left\{\frac{pk_2C1}{T_x(°K)} + pk_2C2 - (pk_2C3 * \ln T_x(°K)) - (pk_2C4 * sal) + (pk_2C5 * sal^2)\right\}}$	(SE4)
Pre-pressure second acid dissociation constant for deeper ocean boxes	$prek_{2\_x} = 10^{-\left\{\frac{pk_2C1}{T_x(°K)} + pk_2C2 - (pk_2C3 * \ln T_x(°K)) - (pk_2C4 * sal) + (pk_2C5 * sal^2)\right\}}$	(SE5)

Pre-pressure sulfuric acid dissociation constant for deep margin and deep boxes	$$preK_{s1\_x} = \frac{K_sC1}{T_x(°K)} + K_sC2 - (K_sC3 * \ln T_x(°K))$$ $$preK_{s2\_x} = \left[\frac{K_sC4}{T_x(°K)} + K_sC5 - (K_sC6 * \ln T_x(°K))\right] * iom_0^{0.5}$$ $$preK_{s3\_x} = \left[\frac{K_sC7}{T_x(°K)} - K_sC8 + (K_sC9 * \ln T_x(°K))\right] * iom_0$$ $$preK_{s4\_x} = \frac{K_sC10}{T_x(°K)} * iom_0^{0.5} * iom_0 + \left(\frac{K_sC11}{\ln T_x(°K)}\right) * iom_0^2$$ $$preK_{s\_x} = e^{[preK_{s1\_x} + preK_{s2\_x} + preK_{s3\_x} + preK_{s4\_x} + \ln(1 - \{K_sK_f * sal\})]}$$	(SE6a-e)
Pre-pressure hydrofluoric acid dissociation constant for deep margin and deep boxes	$$preK_{f\_x} = e^{\left[\frac{K_fC1}{T_x(°K)} - K_fC2 + (K_fC3 * iom_0^{0.5}) + \ln(1 - \{K_sK_f * sal\})\right]}$$	(SE7)
Pre-pressure pH conversions across seawater; total; and free scales	$$pre\_sws\_to\_free_x = 1 + \frac{sulfate\ (mol/kg)_x}{preK_{s\_x}} + \frac{[F^-]}{preK_{f\_x}}$$ $$pre\_total\_to\_free_x = 1 + \frac{sulfate\ (mol/kg)_x}{preK_{s\_x}}$$ $$pre\_total\_to\_sws_x = \frac{pre\_sws\_to\_free_x}{pre\_total\_to\_free_x}$$	(SE8a-c)

First and second acid dissociation constants for deep margin and deep boxes converted to the seawater scale	$sws\_prek_{1\_x} = prek_{1\_x} * total\_to\_sws_x$ $sws\_prek_{2\_x} = prek_{2\_x} * total\_to\_sws_x$	(SE9a-b)
Solubility product of calcite for surficial ocean boxes	$pK_{spc\_x} = ca_{spc1} - \left(ca_{sp2} * T_x(°K)\right) + \frac{ca_{sp3}}{T_x(°K)} + \left(ca_{sp4} * \log_{10} T_x(°K)\right)$ $+ \left\{\left[ca_{sp5} + \left(ca_{sp6} * T_x(°K)\right) + \left(\frac{ca_{sp7}}{T_x(°K)}\right)\right] * sal^{0.5}\right\} + \left(ca_{sp8} * sal\right) + \left(ca_{sp9} * sal^{1.5}\right)$ $K_{spc\_x} = 10^{(pK_{spc\_x})} * 10^6$	(SE10a-b)
Pre-pressure solubility product of calcite for deep margin and deep boxes	$preK_{spc\_x} = 10^{(pK_{spc\_x})} * 10^6$	(SE11)
Solubility product of aragonite for surficial ocean boxes	pK_{spa_x} = As per calcite (SE10a-b) but with aragonite specific constants (e.g. ag_{sp1}) $K_{spa\_x} = 10^{(pK_{spa\_x})} * 10^6$	(SE12a-b)
Pre-pressure solubility product of aragonite for	$preK_{spa\_x} = 10^{(pK_{spa\_x})} * 10^6$	(SE13)

deep margin and deep boxes		
Pressure corrections for all acid dissociation constants and solubility products (and pH scale corrections for k_1 and k_2)	$p_{a0} = [-25.5 \ \ -15.82 \ \ -18.03 \ \ -9.78 \ \ -48.76 \ \ -46]$ $p_{a1} = [0.1271 \ \ -0.0219 \ \ 0.0466 \ \ -0.009 \ \ 0.5304 \ \ 0.5304]$ $p_{a2} = [0 \ \ 0 \ \ 0.000316 \ \ -0.000942 \ \ 0 \ \ 0]$ $p_{b0} = [-0.00308 \ \ 0.00113 \ \ -0.00453 \ \ -0.00391 \ \ -0.01176 \ \ -0.01176]$ $p_{b1} = [0.0000877 \ \ -0.0001475 \ \ 0.00009 \ \ 0.000054 \ \ 0.0003692 \ \ 0.0003692]$ Position in above arrays = (i) $\partial v(i)_x = p_{a0}(i) + [p_{a1}(i) * T_x(°C)] + [p_{a2}(i) * T_x(°C)^2]$ $\partial k(i)_x = p_{b0}(i) + [p_{b1}(i) * T_x(°C)]$ $\ln pok_0(i)_x = \left[-\left(\frac{\partial v(i)_x}{Rgas * T_x(°K)} * Pressure_x\right)\right] + \left[\frac{0.5 * \partial k(i)_x}{Rgas * T_x(°K)} * Pressure_x^2\right]$ $sws\_postk_{1\_x} = sws\_prek_{1\_x} * e^{\ln pok_0(i)_x}$ $sws\_postk_{2\_x} = sws\_prek_{2\_x} * e^{\ln pok_0(i)_x}$ $postK_{s\_x} = preK_{s\_x} * e^{\ln pok_0(i)_x}$ $postK_{f\_x} = preK_{f\_x} * e^{\ln pok_0(i)_x}$ $postK_{spc\_x} = preK_{spc\_x} * e^{\ln pok_0(i)_x}$	(SE14a-n)

	$$postK_{spa\_x} = preK_{spa\_x} * e^{\ln pok_0(i)_x}$$	
Post pressure pH conversions across seawater; total; and free scales	$$post\_sws\_to\_free_x = 1 + \frac{sulfate\ (mol/kg)_x}{postK_{s\_x}} + \frac{[F^-]}{postK_{f\_x}}$$ $$post\_total\_to\_free_x = 1 + \frac{sulfate\ (mol/kg)_x}{postK_{s\_x}}$$ $$post\_total\_to\_sws_x = \frac{post\_sws\_to\_free_x}{post\_total\_to\_free_x}$$	(SE15a-c)
First and second dissociation constants converted back to the total scale for the deeper margin and deep boxes	$$k_{1\_x} = \frac{sws\_postk_{1\_x}}{post\_total\_to\_sws_x}$$ $$k_{2\_x} = \frac{sws\_postk_{2\_x}}{post\_total\_to\_sws_x}$$	(SE16a-b)
Carbonate equilibrium	$$kcarb_x = 1 - \left(4 * \frac{k_{2\_x}}{k_{1\_x}}\right)$$	(SE17)
Bicarbonate concentration	$$[HCO_3^-]_x = \frac{[DIC]_x - \{[DIC]_x^2 - [ALK]_x * (2 * [DIC]_x * [ALK]_x) * kcarb_x\}^{0.5}}{kcarb_x}$$	(SE18)
Carbonate concentration	$$[CO_3^{2-}]_x = \frac{[ALK]_x - [HCO_3^-]_x}{2}$$	(SE19)
Concentration of H^+	$$[H^+]_x = k_{2\_x} * \frac{[HCO_3^-]_x}{[CO_3^{2-}]_x}$$	(SE20)

pH	$pH = -1 * \log_{10}[H^+]_x$	(SE21)
Concentration of aqueous CO_2^*	$CO_{2\,(aq)\_x} = \frac{\left(\frac{[ALK]_x}{1000}\right)}{\left\{\frac{k_{1\_x}}{[H^+]_x} + \left(2 * k_{1_x} * \left\{\frac{k_{2\_x}}{[H^+]_x^2}\right\}\right)\right\}}$	(SE22)
CO_2 fugacity	$pCO_{2\_x} = \frac{\left(\frac{CO_{2\,(aq)\_x}}{k_{0\_x}} * 10^6\right)}{pCO_{2_{a(0)}}}$	(SE23)
Air-sea gas exchange	$AirSea_x = pCO_{2_{a(0)}} * area_x * \frac{1}{\tau} * \left(pCO_{2_{a(t)}} - pCO_{2\_x}\right)$	(SE24)
Calcite saturation	$\Omega_{calc_x\,(t)} = \frac{[Ca^{2+}]_{(0)} * Calc * [CO_3^{2-}]_x}{postK_{spc\_x}}$ or $\Omega_{calc_x\,(t)} = \frac{[Ca^{2+}]_{(0)} * Calc * [CO_3^{2-}]_x}{K_{spc\_x}}$	(SE25a-b)
Aragonite saturation	$\Omega_{arag_x\,(t)} = \frac{[Ca^{2+}]_{(0)} * Calc * [CO_3^{2-}]_x}{postK_{spa\_x}}$ or $\Omega_{arag_x\,(t)} = \frac{[Ca^{2+}]_{(0)} * Calc * [CO_3^{2-}]_x}{K_{spa\_x}}$	(SE26a-b)
Calcite burial	$calcb_x = k_{mccb} * frac_{mccb_x} * \frac{1}{\Omega_{calc_x\,(0)}} * \left[\max(\Omega_{calc_x\,(t)} - 1, 0.1)\right]^{\eta_{calc}\,(t)}$	(SE27)
Aragonite burial	$aragb_x = k_{mccb} * frac_{mccb_x} * \frac{1}{\Omega_{arag_x\,(0)}} * \left[\max(\Omega_{arag_x\,(t)} - 1, 0.1)\right]^{\eta_{arag}\,(t)}$	(SE28)

Table S2: Variables used for the carbonate system.

Variable	Value	Equation(s) location
h1	-60.2409	SE1
h2	93.4517	SE1
h3	23.3585	SE1
h4	0.023517	SE1
h5	0.023656	SE1
h6	0.0047036	SE1
T_{100_x}	$\frac{T_x(°K)}{100}$	SE1
sal	34.78	SE1-SE5, SE6e, SE7, SE10a, SE12a and (80), also other variables below
pk_lC1	3633.86	SE2, SE3
pk_lC2	61.2172	SE2, SE3
pk_lC3	9.6777	SE2, SE3
pk_lC4	0.011555	SE2, SE3
pk_lC5	0.0001152	SE2, SE3

pk_2C1	471.78	SE4, SE5
pk_2C2	25.929	SE4, SE5
pk_2C3	3.16967	SE4, SE5
pk_2C4	0.01781	SE4, SE5
pk_2C5	0.0001122	SE4, SE5
K_sC1	-4276.1	SE6a
K_sC2	141.328	SE6a
K_sC3	23.093	SE6a
K_sC4	-13856	SE6b
K_sC5	324.57	SE6b
K_sC6	47.986	SE6b
K_sC7	35474	SE6c
K_sC8	771.54	SE6c
K_sC9	114.723	SE6c
K_sC10	-2698	SE6d
K_sC11	1776	SE6d

iom_0	$19.924 * \frac{sal}{1000 - (1.005 * sal)}$	SE6b-d, SE7
K_sK_f	0.001005	SE6e, SE7
K_fC1	1590.2	SE7
K_fC2	12.641	SE7
K_fC3	1.525	SE7
$[F^-]$	$\frac{0.000067}{18.998} * \frac{sal}{1.80655}$	SE8a, SE15a
ca_{spc1}	-171.9065	SE10a
ca_{spc2}	0.077993	SE10a
ca_{spc3}	2839.319	SE10a
ca_{spc4}	71.595	SE10a
ca_{spc5}	-0.77712	SE10a
ca_{spc6}	0.0028426	SE10a
ca_{spc7}	178.34	SE10a
ca_{spc8}	-0.07711	SE10a
ca_{spc9}	0.0041249	SE10a
ag_{spc1}	-171.945	SE12a

ag_{spc2}	0.077993	SE12a
ag_{spc3}	2903.293	SE12a
ag_{spc4}	71.595	SE12a
ag_{spc5}	-0.068393	SE12a
ag_{spc6}	0.0017276	SE12a
ag_{spc7}	88.135	SE12a
ag_{spc8}	-0.10018	SE12a
ag_{spc9}	0.0059415	SE12a
R_{gas}	83.1451 mol bar/deg	SE14h
$Pressure_x$	Deep margin = 100 atm Deep = 400 atm	SE14h
$pCO_{2_a(0)}$	280 ppm	SE23, SE24
$area_x$	$area_{sm}$ = 0.1138 $area_s$ = 0.7362 $area_h$ = 0.15	SE24
τ	10 years	SE24
$[Ca^{2+}]_{(0)}$	10.28 mM	SE25a-b, SE26a-b

k_{mccb}	1.95×10^{13} mol/yr	SE27, SE28
$frac_{mccb_x}$	Shallow margin = 0.7 Deeper margin = 0.2 Deep = 0.1	SE27, SE28
$\Omega_{calc_x}(0)$	Shallow margin = 6 Deeper margin = 3 Deep = 1	SE27
$\Omega_{arag_x}(0)$	Shallow margin = 4 Deeper margin = 1 Deep = 0.65	SE28

Table S3: The differential equations underlying the model.

Reservoir name	Equation	Equation number
CO_{2_a}	$f_{ccdeg} + f_{ocdeg} + f_{oxidw} + f_{reductant\_input} - f_{AirSea\_sm} - f_{AirSea\_s} - f_{AirSea\_h} - f_{locb} - f_{carbw} - 2(f_{silw} + f_{sfw})$	(SE29)

O_{2_a}	$[(f_{locb} - f_{ocdeg} - f_{oxidw}) / Red_{C:O2}] - f_{AirSeaO2\_sm} - f_{AirSeaO2\_s} - f_{AirSeaO2\_h} - [(15 / 8) * f_{pyrw}] - f_{reductant\_input}$	(SE30)
DIC_{sm}	$f_{Tran\_DIC\_dm\_sm} + f_{AirSea\_sm} + 2(f_{carbw} + f_{silw}) + f_{Mix\_DIC\_dm\_sm} + f_{POC\_water\_remin\_sm} + f_{DICbenthic\_sm} - f_{Tran\_DIC\_sm\_s} - f_{mccb\_sm} - f_{POC\_primprod\_sm} - f_{SideP\_sm}$	(SE32)
DIC_{dm}	$f_{Tran\_DIC\_d\_dm} + f_{POC\_water\_remin\_dm} + f_{DICbenthic\_dm} - f_{Tran\_DIC\_dm\_sm} - f_{Mix\_DIC\_dm\_sm} - f_{mccb\_dm} - f_{SideP\_dm}$	(SE33)
DIC_{s}	$f_{Tran\_DIC\_d\_s} + f_{AirSea\_s} + f_{Tran\_DIC\_sm\_s} + f_{Mix\_DIC\_d\_s} + f_{POC\_water\_remin\_s} - f_{Tran\_DIC\_s\_h} - f_{POC\_primprod\_s} - f_{SideP\_s}$	(SE34)
DIC_{h}	$f_{Tran\_DIC\_s\_h} + f_{AirSea\_h} + f_{Mix\_DIC\_d\_h} + f_{POC\_water\_remin\_h} - f_{Tran\_DIC\_h\_d} - f_{POC\_primprod\_h} - f_{SideP\_h}$	(SE35)
DIC_{d}	$f_{Tran\_DIC\_h\_d} + 2(f_{sfw}) + f_{POC\_water\_remin\_d} + f_{DICbenthic\_d} - f_{Tran\_DIC\_d\_s} - f_{Tran\_DIC\_d\_dm} - f_{Mix\_DIC\_d\_s} - f_{Mix\_DIC\_d\_h} - f_{mccb\_d} - f_{SideP\_d}$	(SE36)
ALK_{sm}	$f_{Tran\_ALK\_dm\_sm} + f_{Mix\_ALK\_dm\_sm} + 2(f_{carbw} + f_{silw} - f_{mccb\_sm} - f_{SideP\_sm}) + 8(f_{ironR\_sm} + f_{Fe(III)benthic\_sm}) + 4(f_{SironR\_sm}) + 2(f_{water\_pyF\_sm} + f_{seds\_pyF\_sm} + f_{sulfR\_sm} + f_{sulf\_benthic\_sm}) - f_{Tran\_ALK\_sm\_s} - 2(f_{ironO\_sm} + f_{sulfO\_sm})$	(SE37)
ALK_{dm}	$f_{Tran\_ALK\_d\_dm} + 8(f_{ironR\_dm} + f_{Fe(III)benthic\_dm}) + 4(f_{SironR\_dm}) + 2(f_{water\_pyF\_dm} + f_{seds\_pyF\_dm} + f_{sulfR\_dm} + f_{sulf\_benthic\_dm}) - f_{Tran\_ALK\_dm\_sm} - f_{Mix\_ALK\_dm\_sm} - 2(f_{mccb\_dm} + f_{SideP\_dm}) - 2(f_{ironO\_dm} + f_{sulfO\_dm})$	(SE38)
ALK_{s}	$f_{Tran\_ALK\_d\_s} + f_{Tran\_ALK\_sm\_s} + f_{Mix\_ALK\_d\_s} + 8(f_{ironR\_s}) + 4(f_{SironR\_s}) + 2(f_{water\_pyF\_s} + f_{sulfR\_s}) - f_{Tran\_ALK\_s\_h} - 2(f_{ironO\_s} + f_{sulfO\_s})$	(SE39)
ALK_{h}	$f_{Tran\_ALK\_s\_h} + f_{Mix\_ALK\_d\_h} + 8(f_{ironR\_h}) + 4(f_{SironR\_h}) + 2(f_{water\_pyF\_h} + f_{sulfR\_h}) - f_{Tran\_ALK\_h\_d} - 2(f_{ironO\_h} + f_{sulfO\_h})$	(SE40)
ALK_{d}	$f_{Tran\_ALK\_h\_d} + 2(f_{sfw}) + 8(f_{ironR\_d} + f_{Fe(III)benthic\_d}) + 4(f_{SironR\_d}) + 2(f_{water\_pyF\_d} + f_{seds\_pyF\_d} + f_{sulfR\_d} + f_{sulf\_benthic\_d}) - f_{Tran\_ALK\_d\_s} - f_{Tran\_ALK\_d\_dm} - f_{Mix\_ALK\_d\_s} - f_{Mix\_ALK\_d\_h} - 2(f_{mccb\_d} + f_{SideP\_d}) - 2(f_{ironO\_d} + f_{sulfO\_d})$	(SE41)
SO_{4_sm}	$f_{Tran\_SO4\_dm\_sm} + f_{Mix\_SO4\_dm\_sm} + f_{pyrw} + f_{gypw} + f_{sulfO\_sm} + f_{SironR\_sm} - f_{Tran\_SO4\_sm\_s} - f_{gypb} - 0.5(f_{sulfR\_sm} / Red_{C:O2}) - f_{water\_pyF\_sm} - f_{seds\_pyF\_sm}$	(SE42)

SO_{4_dm}	$f_{Tran\_SO4\_d\_dm} + f_{sulfO\_dm} + f_{SironR\_dm} - f_{Tran\_SO4\_dm\_sm} - f_{Mix\_SO4\_dm\_sm} - 0.5(f_{sulfR\_dm} / Red_{C:O2}) - f_{water\_pyF\_dm} - f_{seds\_pyF\_dm}$	(SE43)
SO_{4_s}	$f_{Tran\_SO4\_sm\_s} + f_{Tran\_SO4\_dm\_s} + f_{Mix\_SO4\_d\_s} + f_{sulfO\_s} + f_{SironR\_s} - f_{Tran\_SO4\_s\_h} - 0.5(f_{sulfR\_s} / Red_{C:O2}) - f_{water\_pyF\_s}$	(SE44)
SO_{4_h}	$f_{Tran\_SO4\_s\_h} + f_{Mix\_SO4\_d\_h} + f_{sulfO\_h} + f_{SironR\_h} - f_{Tran\_SO4\_h\_d} - 0.5(f_{sulfR\_h} / Red_{C:O2}) - f_{water\_pyF\_h}$	(SE45)
SO_{4_d}	$f_{Tran\_SO4\_h\_d} + f_{pyrdeg} + f_{gypdeg} + f_{sulfO\_d} + f_{SironR\_d} - f_{Tran\_SO4\_d\_dm} - f_{Tran\_SO4\_d\_s} - f_{Mix\_SO4\_d\_h} - 0.5(f_{sulfR\_d} / Red_{C:O2}) - f_{water\_pyF\_d} - f_{seds\_pyF\_d}$	(SE46)
H_sS_{sm}	$f_{Tran\_H2S\_dm\_sm} + f_{Mix\_H2S\_dm\_sm} + 0.5(f_{sulfR\_sm} / Red_{C:O2}) - f_{Tran\_H2S\_sm\_s} - f_{sulfO\_sm} - f_{SironR\_sm}$	(SE47)
H_sSd_m	$f_{Tran\_H2S\_d\_dm} + 0.5(f_{sulfR\_dm} / Red_{C:O2}) - f_{Tran\_H2S\_dm\_sm} - f_{Mix\_H2S\_dm\_sm} - f_{sulfO\_dm} - f_{SironR\_dm}$	(SE48)
H_sS_s	$f_{Tran\_H2S\_sm\_s} + f_{Tran\_H2S\_d\_s} + f_{Mix\_H2S\_d\_s} + 0.5(f_{sulfR\_s} / Red_{C:O2}) - f_{Tran\_H2S\_s\_h} - f_{sulfO\_s} - f_{SironR\_s}$	(SE49)
H_sS_h	$f_{Tran\_H2S\_s\_h} + f_{Mix\_H2S\_d\_h} + 0.5(f_{sulfR\_h} / Red_{C:O2}) - f_{Tran\_H2S\_h\_d} - f_{sulfO\_h} - f_{SironR\_h}$	(SE50)
H_sS_d	$f_{Tran\_H2S\_h\_d} + 0.5(f_{sulfR\_d} / Red_{C:O2}) - f_{Tran\_H2S\_d\_dm} - f_{Tran\_H2S\_d\_s} - f_{Mix\_H2S\_d\_s} - f_{Mix\_H2S\_d\_h} - f_{sulfO\_d} - f_{SironR\_d}$	(SE51)
O_{2_sm}	$f_{Tran\_O2\_dm\_sm} + f_{Mix\_O2\_dm\_sm} + f_{AirSeaO2\_sm} + [(15 / 8) * (f_{water\_pyF\_sm} + f_{seds\_pyF\_sm})] + f_{O2\_primprod\_sm} - f_{Tran\_O2\_sm\_s} - (f_{AR\_sm} / Red_{C:O2}) - f_{O2benthic\_sm} - f_{methanogenesis\_sm} - 0.5(f_{ironO\_sm}) - 2(f_{sulfO\_sm})$	(SE52)
O_{2_dm}	$f_{Tran\_O2\_d\_dm} + [(15 / 8) * (f_{water\_pyF\_dm} + f_{seds\_pyF\_dm})] - f_{Tran\_O2\_dm\_sm} - f_{Mix\_O2\_dm\_sm} - (f_{AR\_dm} / Red_{C:O2}) - f_{O2benthic\_dm} - f_{methanogenesis\_dm} - 0.5(f_{ironO\_dm}) - 2(f_{sulfO\_dm})$	(SE53)
O_{2_s}	$f_{Tran\_O2\_sm\_s} + f_{Tran\_O2\_d\_s} + f_{Mix\_O2\_d\_s} + f_{AirSeaO2\_s} + [(15 / 8) * f_{water\_pyF\_s}] + f_{O2\_primprod\_s} - f_{Tran\_O2\_s\_h} - (f_{AR\_s} / Red_{C:O2}) - 0.5(f_{ironO\_s}) - 2(f_{sulfO\_s})$	(SE54)
O_{2_h}	$f_{Tran\_O2\_s\_h} + f_{Mix\_O2\_d\_h} + f_{AirSeaO2\_h} + [(15 / 8) * f_{water\_pyF\_h}] + f_{O2\_primprod\_h} - f_{Tran\_O2\_h\_d} - (f_{AR\_h} / Red_{C:O2}) - 0.5(f_{ironO\_h}) - 2(f_{sulfO\_h})$	(SE55)

O_{2_d}	$f_{Tran\_O2\_h\_d} + [(15 / 8) * (f_{water\_pyF\_d} + f_{seds\_pyF\_d})] - f_{Tran\_O2\_d\_dm} - f_{Tran\_O2\_d\_s} - f_{Mix\_O2\_d\_s} - f_{Mix\_O2\_d\_h} - (f_{AR\_d} / Red_{C:O2}) - [(15 / 8) * f_{pyrdeg}] - f_{O2benthic\_d} - f_{methanogenesis\_d} - 0.5(f_{ironO\_d}) - 2(f_{sulfO\_d})$	(SE56)
$DPhos_{sm}$	$f_{Tran\_DPhos\_dm\_sm} + f_{Mix\_DPhos\_dm\_sm} + f_{psea} + f_{phosbenthic\_sm} + f_{POP\_water\_remin\_sm} + f_{P\_dust\_sm} - f_{Tran\_DPhos\_sm\_s} - f_{POP\_primprod\_sm}$	(SE57)
$DPhos_{dm}$	$f_{Tran\_DPhos\_d\_dm} + f_{phosbenthic\_dm} + f_{POP\_water\_remin\_dm} - f_{Tran\_DPhos\_dm\_sm} - f_{Mix\_DPhos\_dm\_sm}$	(SE58)
$DPhos_{s}$	$f_{Tran\_DPhos\_sm\_s} + f_{Tran\_DPhos\_d\_s} + f_{Mix\_DPhos\_d\_s} + f_{POP\_water\_remin\_s} + f_{P\_dust\_s} - f_{Tran\_DPhos\_s\_h} - f_{POP\_primprod\_s}$	(SE59)
$DPhos_{h}$	$f_{Tran\_DPhos\_s\_h} + f_{Mix\_DPhos\_d\_h} + f_{POP\_water\_remin\_h} + f_{P\_dust\_h} - f_{Tran\_DPhos\_h\_d} - f_{POP\_primprod\_h}$	(SE60)
$DPhos_{d}$	$f_{Tran\_DPhos\_h\_d} + f_{phosbenthic\_d} + f_{POP\_water\_remin\_d} - f_{Tran\_DPhos\_d\_dm} - f_{Tran\_DPhos\_d\_s} - f_{Mix\_DPhos\_d\_s} - f_{Mix\_DPhos\_d\_h} - f_{phos\_hydro}$	(SE61)
POP_{sm}	$f_{POP\_primprod\_sm} - f_{Tran\_POP\_sm\_s} - f_{Sink\_POP\_sm\_dm} - f_{POP\_water\_remin\_sm} - f_{P\_water\_seds\_export\_sm}$	(SE62)
POP_{dm}	$f_{Tran\_POP\_d\_dm} + f_{Sink\_POP\_sm\_dm} - f_{POP\_water\_remin\_dm} - f_{P\_water\_seds\_export\_dm}$	(SE63)
POP_{s}	$f_{POP\_primprod\_s} + f_{Tran\_POP\_sm\_s} - f_{Tran\_POP\_s\_h} - f_{Sink\_POP\_s\_d} - f_{POP\_water\_remin\_s}$	(SE64)
POP_{h}	$f_{POP\_primprod\_h} + f_{Tran\_POP\_s\_h} - f_{Sink\_POP\_h\_d} - f_{POP\_water\_remin\_h}$	(SE65)
POP_{d}	$f_{Sink\_POP\_s\_d} + f_{Sink\_POP\_h\_d} - f_{Tran\_POP\_d\_dm} - f_{POP\_water\_remin\_d} - f_{P\_water\_seds\_export\_d}$	(SE66)
POC_{sm}	$f_{POC\_primprod\_sm} - f_{Tran\_POC\_sm\_s} - f_{Sink\_POC\_sm\_dm} - f_{POC\_water\_remin\_sm} - f_{C\_water\_seds\_export\_sm}$	(SE67)
POC_{dm}	$f_{Tran\_POC\_d\_dm} + f_{Sink\_POC\_sm\_dm} - f_{POC\_water\_remin\_dm} - f_{C\_water\_seds\_export\_dm}$	(SE68)
POC_{s}	$f_{POC\_primprod\_s} + f_{Tran\_POC\_sm\_s} - f_{Tran\_POC\_s\_h} - f_{Sink\_POC\_s\_d} - f_{POC\_water\_remin\_s}$	(SE69)
POC_{h}	$f_{POC\_primprod\_h} + f_{Tran\_POC\_s\_h} - f_{Sink\_POC\_h\_d} - f_{POC\_water\_remin\_h}$	(SE70)
POC_{d}	$f_{Sink\_POC\_s\_d} + f_{Sink\_POC\_h\_d} - f_{Tran\_POC\_d\_dm} - f_{POC\_water\_remin\_d} - f_{C\_water\_seds\_export\_d}$	(SE71)

$FeIII_{sm}$	$f_{Tran\_FeIII\_dm\_sm} + f_{Mix\_FeIII\_dm\_sm} + f_{FeIIIw} + f_{Fe\_dust\_sm} + (f_{POC\_water\_remin\_sm} / Red_{C:Fe}) + f_{ironO\_sm} - f_{Tran\_FeIII\_sm\_s} - (f_{POC\_primprod\_sm} / Red_{C:Fe}) - 4(f_{ironR\_sm}) - 8(f_{SironR\_sm}) - f_{Fe\_scav\_sm} - f_{seds\_pyF\_sm}$	(SE72)
$FeIII_{dm}$	$f_{Tran\_FeIII\_d\_dm} + (f_{POC\_water\_remin\_dm} / Red_{C:Fe}) + f_{ironO\_dm} - f_{Tran\_FeIII\_dm\_sm} - f_{Mix\_FeIII\_dm\_sm} - 4(f_{ironR\_dm}) - 8(f_{SironR\_dm}) - f_{Fe\_scav\_dm} - f_{seds\_pyF\_dm}$	(SE73)
$FeIII_{s}$	$f_{Tran\_FeIII\_sm\_s} + f_{Tran\_FeIII\_d\_s} + f_{Mix\_FeIII\_d\_s} + f_{Fe\_dust\_s} + (f_{POC\_water\_remin\_s} / Red_{C:Fe}) + f_{ironO\_s} - f_{Tran\_FeIII\_s\_h} - (f_{POC\_primprod\_s} / Red_{C:Fe}) - 4(f_{ironR\_s}) - 8(f_{SironR\_s}) - f_{Fe\_scav\_s}$	(SE74)
$FeIII_{h}$	$f_{Tran\_FeIII\_s\_h} + f_{Mix\_FeIII\_d\_h} + f_{Fe\_dust\_h} + (f_{POC\_water\_remin\_h} / Red_{C:Fe}) + f_{ironO\_h} - f_{Tran\_FeIII\_h\_d} - (f_{POC\_primprod\_h} / Red_{C:Fe}) - 4(f_{ironR\_h}) - 8(f_{SironR\_h}) - f_{Fe\_scav\_h}$	(SE75)
$FeIII_{d}$	$f_{Tran\_FeIII\_h\_d} + (f_{POC\_water\_remin\_d} / Red_{C:Fe}) + f_{ironO\_d} - f_{Tran\_FeIII\_d\_dm} - f_{Tran\_FeIII\_d\_s} - f_{Mix\_FeIII\_d\_s} - f_{Mix\_FeIII\_d\_h} - 4(f_{ironR\_d}) - 8(f_{SironR\_d}) - f_{Fe\_scav\_d} - f_{seds\_pyF\_d}$	(SE76)
$FeII_{sm}$	$f_{Tran\_FeII\_dm\_sm} + f_{Mix\_FeII\_dm\_sm} + 4(f_{ironR\_sm}) + 8(f_{SironR\_sm}) - f_{Tran\_FeII\_sm\_s} - f_{ironO\_sm} - f_{water\_pyF\_sm} - f_{SideP\_sm}$	(SE77)
$FeII_{dm}$	$f_{Tran\_FeII\_d\_dm} + 4(f_{ironR\_dm}) + 8(f_{SironR\_dm}) - f_{Tran\_FeII\_dm\_sm} - f_{Mix\_FeII\_dm\_sm} - f_{ironO\_dm} - f_{water\_pyF\_dm} - f_{SideP\_dm}$	(SE78)
$FeII_{s}$	$f_{Tran\_FeII\_sm\_s} + f_{Tran\_FeII\_d\_s} + f_{Mix\_FeII\_d\_s} + 4(f_{ironR\_s}) + 8(f_{SironR\_s}) - f_{Tran\_FeII\_s\_h} - f_{ironO\_s} - f_{water\_pyF\_s}$	(SE79)
$FeII_{h}$	$f_{Tran\_FeII\_s\_h} + f_{Mix\_FeII\_d\_h} + 4(f_{ironR\_h}) + 8(f_{SironR\_h}) - f_{Tran\_FeII\_h\_d} - f_{ironO\_h} - f_{water\_pyF\_h}$	(SE80)
$FeII_{d}$	$f_{Tran\_FeII\_h\_d} + f_{Fe\_hydro} + 4(f_{ironR\_d}) + 8(f_{SironR\_d}) - f_{Tran\_FeII\_d\_dm} - f_{Tran\_FeII\_d\_s} - f_{Mix\_FeII\_d\_s} - f_{Mix\_FeII\_d\_h} - f_{ironO\_d} - f_{water\_pyF\_d} - f_{SideP\_d}$	(SE81)
N	$f_{nfix} - f_{denit\_total} - f_{monb}$	(SE82)
G	$f_{locb} + f_{mocb\_total} - f_{ocdeg} - f_{oxidw}$	(SE83)

C	$f_{mccb\_total} - f_{ccdeg} - f_{carbw}$	(SE84)
PYR	$f_{pyrb\_total} - f_{pyrdeg} - f_{pyrw}$	(SE85)
GYP	$f_{gypb} - f_{gypdeg} - f_{gypw}$	(SE86)

Table S4: Present-day flux sizes

Flux	Model abbreviation	Size (mol/yr)	Reference
Carbonate weathering	k_{carbw}	8.00×10^{12}	(Mills, Donnadieu and Goddéris, 2021)
Carbonate degassing	k_{ccdeg}	1.20×10^{13}	This work
Whole ocean carbonate burial	k_{mccb}	1.95×10^{13}	(Lenton, Daines and Mills, 2018) - k_{sfw}
Seafloor weathering	k_{sfw}	5.00×10^{11}	This work
Silicate weathering	k_{silw}	1.50×10^{13}	This work: k_{mccb} - k_{carbw}
Granite weathering	k_{gran}	8.05×10^{12}	0.7x k_{silw}
Basalt weathering	k_{bas}	3.45×10^{12}	0.3x k_{silw}
Organic carbon degassing	k_{ocdeg}	1.25×10^{12}	(Mills, Donnadieu and Goddéris, 2021)
Oxidative weathering	k_{oxidw}	7.35×10^{12}	This work, mass balance

Terrestrial organic carbon burial	k_{locb}	4.50×10^{12}	(Bergman, 2004; Lenton, Daines and Mills, 2018)
Whole ocean organic carbon burial	k_{mocb}	4.50×10^{12}	(Bergman, 2004; Lenton, Daines and Mills, 2018)
Reductant input	$k_{reductant\_input}$	0.40×10^{12}	(Schopf and Klein, 1992)
Gypsum weathering	k_{gypw}	2.00×10^{12}	(Mills, Donnadieu and Goddéris, 2021)
Gypsum degassing	k_{gypdeg}	0.50×10^{12}	(Mills, Donnadieu and Goddéris, 2021)
Gypsum burial	k_{gypb}	2.50×10^{12}	(Mills, Donnadieu and Goddéris, 2021)
Pyrite weathering	k_{pyrw}	4.50×10^{11}	(Mills, Donnadieu and Goddéris, 2021)
Pyrite degassing	k_{pyrdeg}	2.50×10^{11}	(Mills, Donnadieu and Goddéris, 2021)
Whole ocean pyrite burial	k_{pyrb}	7.00×10^{11}	(Mills, Donnadieu and Goddéris, 2021)
Phosphorus weathering^	k_{phosw}	1.06×10^{11}	This work, mass balance
Hydrothermal input of phosphorus	k_{P_hydro}	1.30×10^{10}	(Wallmann *et al.*, 2019)
Total dust input of phosphorus	k_{P_dust}	1.60×10^{9}	(Moore *et al.*, 2013)
Whole ocean Fe-P burial^	k_{PFe}	2.25×10^{10}	(Alcott, Mills and Poulton, 2019)
Whole ocean authigenic phosphorus burial^	k_{Pauth}	4.75×10^{10}	(Alcott, Mills and Poulton, 2019)

Iron weathering	$k_{Fe(III)w}$	2.50×10^{11}	This work
Hydrothermal input of iron	$k_{Fe(II)\_hydro}$	5.50×10^{11}	This work
Total dust input of iron	k_{Fe_dust}	3.75×10^{10}	(Tagliabue, Aumont and Bopp, 2014)
Nitrogen fixation	k_{nfix}	8.67×10^{12}	(Mills, Donnadieu and Goddéris, 2021)
Denitrification	k_{denit}	4.30×10^{12}	(Mills, Donnadieu and Goddéris, 2021)
Rate constant for primary production of organic carbon^	$k_{pp\_x\ (0)}$	Shallow margin = 2.47×10^{17} Low-latitude surface = 1.60×10^{18} High-latitude surface = 1.33×10^{18}	This work, based on (Alcott, Mills and Poulton, 2019) but altered to reflect the concentration of P and the effect of temperature on primary production
Sinking of particulate organic carbon from surface boxes to the deeper boxes^	$POC_{sink\_x\ (0)}$	Shallow to deep margin = 5.65×10^{13} Low-latitude surface to deep = 3.67×10^{14} High-latitude surface to deep = 7.47×10^{13}	This work, based on (Sarmiento and Toggweiler, 1984; Costello, Smith and Fraczek, 2015; Alcott, Mills and Poulton, 2019)

Particulate organic carbon remineralisation in the water column^	$k_{POCwr\_x\ (0)}$	Shallow margin = 4.30×10^{14} Deep margin = 5.88×10^{13} Low-latitude surface = 2.81×10^{15} High-latitude surface to deep = 6.05×10^{14} Deep = 4.22×10^{14}	(Sarmiento and Toggweiler, 1984; Costello, Smith and Fraczek, 2015; Middelburg, 2019)
Particulate organic carbon export from the water column to sediments^	$k_{watsed\_x\ (0)}$	Shallow margin = 8.51×10^{13} Deep margin = 2.84×10^{13} Deep = 2.84×10^{13}	This work, mass balance (primary productivity = water remineralisation + export) after taking into account other electron acceptors
Sinking of particulate organic phosphorus from surface boxes to the deeper boxes^	$POP_{sink\_x\ (0)}$	Shallow to deep margin = 5.33×10^{11} Low-latitude surface to deep = 3.46×10^{12} High-latitude surface to deep = 7.04×10^{11}	This work: $POC_{sink\_x\ (0)} / Red_{C:P}$

^Sizes given to two decimal places for clarity; see model code for exact sizes.

Table S5: Non-carbonate system model constants

Constant	Model abbreviation	Size (units)	Reference
Erosion rate scaling parameter	$k_{erosion}$	3.30×10^{-3}	(Maffre *et al.*, 2018)
Silicate weathering scaling factor	$silw_{scale}$	6.50×10^{8}	(Merdith *et al.*, 2025)
Carbonate weathering scaling factor	$carbw_{scale}$	200	(Mills, Donnadieu and Goddéris, 2021)
Mass fraction of chemically mobile material in the bedrock	χ_m	0.1	(West, 2012)
Inherent characteristics of mineral weathering and dependence on grain size	k_{grain}	6.00×10^{-5}	(West, 2012; Mills, Donnadieu and Goddéris, 2021)
Role of water flow	k_{wflow}	1.00×10^{-3}	(West, 2012; Mills, Donnadieu and Goddéris, 2021)
Activation energy for terrestrial silicate weathering	E_a	20 kJ/mol	(Maffre *et al.*, 2018)
Activation energy for seafloor weathering	E_{a_sfw}	42 kJ/mol equivalent to 0.0608	(Mills, Daines and Lenton, 2014; Lenton, Daines and Mills, 2018)

Effective depth of the weathering zone	z	10	(West, 2012; Mills, Donnadieu and Goddéris, 2021)
Weathering reaction time	$\sigma+1$	0.9	(West, 2012; Mills, Donnadieu and Goddéris, 2021)s
Reference temperature for erosion	$T0$	286°K	(Mills, Donnadieu and Goddéris, 2021)
Assumed ice temperature	T_{crit}	-10°C	(Mills, Donnadieu and Goddéris, 2021)
Weathering enhancement factor for arcs	*arcfactor*	7	(Merdith *et al.*, 2025)
Weathering enhancement factor for sutures	*suturefactor*	20	(Merdith *et al.*, 2025)
Present day ocean oxic fraction	k_{oxfrac}	0.9975	(Lenton, Daines and Mills, 2018)
Fire feedback	k_{fire}	3	(Lenton, Daines and Mills, 2018)
Fraction of the shallow margin ocean interacting with the atmosphere	$area_{sm}$	0.1138	This work / (Costello, Smith and Fraczek, 2015)
Fraction of the low-latitude surface ocean interacting with the atmosphere	$area_{s}$	0.7362	This work / (Costello, Smith and Fraczek, 2015)

Fraction of the high-latitude surface ocean interacting with the atmosphere	$area_h$	0.15	This work / (Sarmiento and Toggweiler, 1984; Costello, Smith and Fraczek, 2015)
Global thermohaline speed	*circ_TH_Sv*	20 Sv	(Toggweiler, 1999)
Coastal thermohaline speed	*circ_coastal_Sv*	4 Sv	(Toggweiler, 1999; Zhao *et al.*, 2023)
Mixing coefficient deep margin to shallow margin	*mixcoeff_dmsm*	40 Sv	This work, based on: (Toggweiler, 1999; Wallmann, 2003)
Mixing coefficient deep ocean to low-latitude surface	*mixcoeff_ds*	20 Sv	This work, based on: (Toggweiler, 1999; Wallmann, 2003)
Mixing coefficient deep ocean to high-latitude surface	*mixcoeff_dh*	60 Sv	This work, based on: (Toggweiler, 1999; Wallmann, 2003)
Conversion factor for thermohaline circulation and ocean mixing coefficients (Sv to m^3/yr)	*Sv_to_m3yr*	3.1536×10^{13} m^3/yr	1 Sv = 10^6 m^3/s
Pre-industrial global average surface temperature	$T_{(0)}$	288°K	~average Quaternary: (Scotese *et al.*, 2021; Judd *et al.*, 2024)
Average deep ocean temperature	$T_{d\,(0)}$	278°K	(Walker and Kasting, 1992)

e-folding temperature for biological rates in the ocean	$temp_{biota}$	15.65°C	(Wallmann *et al.*, 2019)
Fraction of total silicate weathering from basalts	bas_{frac}	0.30	(Lenton, Daines and Mills, 2018)
Fraction of phosphorus from weathering retained on land	$k_{landfrac}$	0.0588	(Lenton, Daines and Mills, 2018)
C:P Redfield ratio	$Red_{C:P}$	106	(Redfield, 1958)
C:N Redfield ratio	$Red_{C:N}$	$\frac{106}{16}$	(Redfield, 1958)
C:O_2 Redfield ratio	$Red_{C:O2}$	$\frac{106}{138}$	(Redfield, 1958)
Fe:P ratio	$Red_{Fe:P}$	$\frac{0.0075}{1}$	(Bristow *et al.*, 2017)
C:Fe ratio	$Red_{C:Fe}$	$\frac{106}{0.0075}$	(Bristow *et al.*, 2017)
C:N ratio for marine N burial	CN_{sea}	37.50	(Lenton, Daines and Mills, 2018)
Monod constant for phosphorus limitation on primary productivity	Mon_{P_pp}	1.90×10^{-3} mol/m^3	This work, based on: (Parker, Mock and Armbrust, 2008; Munkes, Löptien and Dietze, 2021)

Monod constant for O_2 limitation on aerobic respiration and other reactions	Mon_{O2}	$1.00x10^{-5}$ mol/m^3	This work, based on: (Tiano *et al.*, 2014)
Monod constant for limitation and inhibition of Fe	Mon_{Fe_resp}	10 mol/m^3	(Thamdrup, 2000)
Limitation constant for dissimilatory sulfate reduction	Mon_{SO4_resp}	0.5 mol/m^3	(Olson, Reinhard and Lyons, 2016)
Inhibition constant for dissimilatory sulfate reduction	Mon_{SO4_inhib}	1 mol/m^3	(Ridgwell *et al.*, 2007)
A scaling coefficient for determining temperature effect on net primary productivity	kt_{scale}	0.37	This work, based on new $temp_{biota}$
An attenuation factor for sulfate reduction and methanogenesis	k_{Ψ}	0.075	(Reed, Slomp and Gustafsson, 2011)
CO_2 level at which primary productivity halves	$CO_{2\_pp\_half}$	183.6 ppm	(Lenton, Daines and Mills, 2018)
Minimum CO_2 level for primary productivity to occur	$CO_{2\_pp\_min}$	10 ppm	(Lenton, Daines and Mills, 2018)

Terrestrial net primary productivity constant	$k_{npp\_terrestrial}$	2	(Lenton, Daines and Mills, 2018)
Weiss equation constants	*A1-A4, B1-B3*	A1 = -173.4292 A2 = 249.6339 A3 = 143.3483 A4 = -21.8492 B1 = -0.033096 B2 = 0.014259 B3 = -0.0017	(Weiss, 1970)
Molar volume of O_2 at standard temperature and pressure	k_{mv}	22.3859	(Weiss, 1970)
Piston velocity	k_{pv_x}	Shallow margin = 3.572831×10^{14} Low-latitude surface = 1.476284×10^{15} High-latitude surface = 2.210798×10^{16}	(Zhao *et al.*, 2023)

Pyrite formation constant	k_{py}	3.2504328 mol/m^3/yr	(Rickard, 1997)
Iron oxidation constant	k_{ironO}	1.40x10^4 mol/m^3/yr	(Wang and Van Cappellen, 1996; Zhao *et al.*, 2020)
Sulfide oxidation constant	k_{sulfO}	100 mol/m^3/yr	(Millero *et al.*, 1987)
Sulfide mediated iron reduction constant	k_{SironR}	8 mol/m^3/yr	(Wang and Van Cappellen, 1996; Zhao *et al.*, 2020)
Siderite precipitation constant	k_{Side}	4x10^3 mol/m^3/yr	(Wang and Van Cappellen, 1996)
Solubility constant for siderite	$K_{sp\_siderite}$	0.004 mol/m^3/yr	(Wang and Van Cappellen, 1996)
Solubility constant for aqueous FeS	$K_{spFeS(aq)}$	0.0083 mol/m^3/yr	(Van De Velde *et al.*, 2021)
Solubility threshold for aqueous FeS	$ST_{FeS(aq)}$	0.002 mol/m^3/yr	(Van De Velde *et al.*, 2021)
Present day global average Fe(III) bound to ligands	k_{Fe_ligand}	6.00x10^{-7} mol/m^3/yr	(Lefèvre and Watson, 1999)
Fraction of P coming from silicate weathering	$p_{frac\ silw}$	0.8	(Lenton, Daines and Mills, 2018)
Fraction of P coming from carbonate weathering	$p_{frac\ carbw}$	0.14	(Lenton, Daines and Mills, 2018)

Fraction of P coming from oxidative weathering	$p_{frac\ oxidw}$	0.06	(Lenton, Daines and Mills, 2018)
Burial efficiency of organic carbon^	CBE_x	Shallow margin = 0.024 Deep margin = 0.056 Deep = 0.032	This work, based on total marine C_{org} burial of $4.5x10^{12}$ mol/yr C split as 45% shallow margin, 35% deep margin, 20% deep, such that when the CBE is multiplied by the water to sediment export flux, the overall marine C_{org} burial flux value is recovered
Burial efficiency of phosphorus^	PBE_x	Shallow margin = 0.025 Deep margin = 0.056 Deep = 0.033	This work, based on total marine POP burial of ~$1.858x10^{10}$ mol/yr P split as ~46% shallow margin, ~34% deep margin, 20% deep, such that when the PBE is multiplied by the water to sediment export flux, the overall marine POP burial flux value is recovered

^In the model these need a high level of precision (to 15 decimal places), but for simplicity have rounded to three decimal places here – see model code for more details.

References

Alcott, L.J., Mills, B.J.W. and Poulton, S.W. (2019) 'Stepwise Earth oxygenation is an inherent property of global biogeochemical cycling', *Science*, 366(6471), pp. 1333–1337. Available at: https://doi.org/10.1126/science.aax6459.

Bergman, N.M. (2004) 'COPSE: A new model of biogeochemical cycling over Phanerozoic time', *American Journal of Science*, 304(5), pp. 397–437. Available at: https://doi.org/10.2475/ajs.304.5.397.

Bristow, L.A. *et al.* (2017) 'Nutrients that limit growth in the ocean', *Current Biology*, 27(11), pp. R474–R478. Available at: https://doi.org/10.1016/j.cub.2017.03.030.

Costello, M.J., Smith, M. and Fraczek, W. (2015) 'Correction to Surface Area and the Seabed Area, Volume, Depth, Slope, and Topographic Variation for the World's Seas, Oceans, and Countries', *Environmental Science & Technology*, 49(11), pp. 7071–7072. Available at: https://doi.org/10.1021/acs.est.5b01942.

Judd, E.J. *et al.* (2024) 'A 485-million-year history of Earth's surface temperature', *Science*, 385(6715), p. eadk3705. Available at: https://doi.org/10.1126/science.adk3705.

Lefèvre, N. and Watson, A.J. (1999) 'Modeling the geochemical cycle of iron in the oceans and its impact on atmospheric CO_2 concentrations', *Global Biogeochemical Cycles*, 13(3), pp. 727–736. Available at: https://doi.org/10.1029/1999GB900034.

Lenton, T.M., Daines, S.J. and Mills, B.J.W. (2018) 'COPSE reloaded: An improved model of biogeochemical cycling over Phanerozoic time', *Earth-Science Reviews*, 178, pp. 1–28. Available at: https://doi.org/10.1016/j.earscirev.2017.12.004.

Maffre, P. *et al.* (2018) 'Mountain ranges, climate and weathering. Do orogens strengthen or weaken the silicate weathering carbon sink?', *Earth and Planetary Science Letters*, 493, pp. 174–185. Available at: https://doi.org/10.1016/j.epsl.2018.04.034.

Merdith, A.S. *et al.* (2025) 'Phanerozoic icehouse climates as the result of multiple solid-Earth cooling mechanisms', *Science Advances*, 11(7), p. eadm9798. Available at: https://doi.org/10.1126/sciadv.adm9798.

Middelburg, J.J. (2019) 'Carbon Processing at the Seafloor', in J. J. Middelburg, *Marine Carbon Biogeochemistry*. Cham: Springer International Publishing (SpringerBriefs in Earth System Sciences), pp. 57–75. Available at: https://doi.org/10.1007/978-3-030-10822-9_4.

Millero, F.J. *et al.* (1987) 'Oxidation of H_2S in seawater as a function of temperature, pH, and ionic strength', *Environmental Science & Technology*, 21(5), pp. 439–443. Available at: https://doi.org/10.1021/es00159a003.

Mills, B., Daines, S.J. and Lenton, T.M. (2014) 'Changing tectonic controls on the long-term carbon cycle from Mesozoic to present', *Geochemistry, Geophysics, Geosystems*, 15(12), pp. 4866–4884. Available at: https://doi.org/10.1002/2014GC005530.

Mills, B.J.W., Donnadieu, Y. and Goddéris, Y. (2021) 'Spatial continuous integration of Phanerozoic global biogeochemistry and climate', *Gondwana Research*, 100, pp. 73–86. Available at: https://doi.org/10.1016/j.gr.2021.02.011.

Moore, C.M. *et al.* (2013) 'Processes and patterns of oceanic nutrient limitation', *Nature Geoscience*, 6(9), pp. 701–710. Available at: https://doi.org/10.1038/ngeo1765.

Munkes, B., Löptien, U. and Dietze, H. (2021) 'Cyanobacteria blooms in the Baltic Sea: a review of models and facts', *Biogeosciences*, 18(7), pp. 2347–2378. Available at: https://doi.org/10.5194/bg-18-2347-2021.

Olson, S.L., Reinhard, C.T. and Lyons, T.W. (2016) 'Limited role for methane in the mid-Proterozoic greenhouse', *Proceedings of the National Academy of Sciences*, 113(41), pp. 11447–11452. Available at: https://doi.org/10.1073/pnas.1608549113.

Parker, M.S., Mock, T. and Armbrust, E.V. (2008) 'Genomic Insights into Marine Microalgae', *Annual Review of Genetics*, 42(1), pp. 619–645. Available at: https://doi.org/10.1146/annurev.genet.42.110807.091417.

Redfield, A.C. (1958) 'The Biological Control of Chemical Factors in the Environment', *American Scientist*, pp. 205–221.

Reed, D.C., Slomp, C.P. and Gustafsson, B.G. (2011) 'Sedimentary phosphorus dynamics and the evolution of bottom-water hypoxia: A coupled benthic–pelagic model of a coastal system', *Limnology and Oceanography*, 56(3), pp. 1075–1092. Available at: https://doi.org/10.4319/lo.2011.56.3.1075.

Rickard, D. (1997) 'Kinetics of pyrite formation by the H_2S oxidation of iron (II) monosulfide in aqueous solutions between 25 and 125°C: The rate equation', *Geochimica et Cosmochimica Acta*, 61(1), pp. 115–134. Available at: https://doi.org/10.1016/S0016-7037(96)00321-3.

Ridgwell, A. *et al.* (2007) 'Marine geochemical data assimilation in an efficient Earth System Model of global biogeochemical cycling', *Biogeosciences*, 4, pp. 87–104. Available at: https://doi.org/https://doi.org/10.5194/bg-4-87-2007.

Sarmiento, J.L. and Toggweiler, J.R. (1984) 'A new model for the role of the oceans in determining atmospheric pCO_2', *Nature*, 308(5960), pp. 621–624. Available at: https://doi.org/10.1038/308621a0.

Schopf, J.W. and Klein, C. (eds) (1992) 'The Proterozoic Biosphere', *The Proterozoic Biosphere*. 1st edn. Cambridge University Press, pp. 1–2. Available at: https://doi.org/10.1017/CBO9780511601064.002.

Scotese, C.R. *et al.* (2021) 'Phanerozoic paleotemperatures: The earth's changing climate during the last 540 million years', *Earth-Science Reviews*, 215, p. 103503. Available at: https://doi.org/10.1016/j.earscirev.2021.103503.

Tagliabue, A., Aumont, O. and Bopp, L. (2014) 'The impact of different external sources of iron on the global carbon cycle', *Geophysical Research Letters*, 41(3), pp. 920–926. Available at: https://doi.org/10.1002/2013GL059059.

Thamdrup, B. (2000) 'Bacterial Manganese and Iron Reduction in Aquatic Sediments', in B. Schink (ed.) *Advances in Microbial Ecology*. Boston, MA: Springer US (Advances in Microbial Ecology), pp. 41–84. Available at: https://doi.org/10.1007/978-1-4615-4187-5_2.

Tiano, L. *et al.* (2014) 'Oxygen distribution and aerobic respiration in the north and south eastern tropical Pacific oxygen minimum zones', *Deep Sea Research Part I: Oceanographic Research Papers*, 94, pp. 173–183. Available at: https://doi.org/10.1016/j.dsr.2014.10.001.

Toggweiler, J.R. (1999) 'Variation of atmospheric CO_2 by ventilation of the ocean's deepest water', *Paleoceanography*, 14(5), pp. 571–588. Available at: https://doi.org/10.1029/1999PA900033.

Van De Velde, S.J. *et al.* (2021) 'Iron and sulfur cycling in the cGENIE.muffin Earth system model (v0.9.21)', *Geoscientific Model Development*, 14(5), pp. 2713–2745. Available at: https://doi.org/10.5194/gmd-14-2713-2021.

Walker, J.C.G. and Kasting, J.F. (1992) 'Effects of fuel and forest conservation on future levels of atmospheric carbon dioxide', *Palaeogeography, Palaeoclimatology, Palaeoecology*, 97(3), pp. 151–189. Available at: https://doi.org/10.1016/0031-0182(92)90207-L.

Wallmann, K. (2003) 'Feedbacks between oceanic redox states and marine productivity: A model perspective focused on benthic phosphorus cycling', *Global Biogeochemical Cycles*, 17(3), p. 2002GB001968. Available at: https://doi.org/10.1029/2002GB001968.

Wallmann, K. *et al.* (2019) 'Periodic changes in the Cretaceous ocean and climate caused by marine redox see-saw', *Nature Geoscience*, 12(6), pp. 456–461. Available at: https://doi.org/10.1038/s41561-019-0359-x.

Wang, Y. and Van Cappellen, P. (1996) 'A multicomponent reactive transport model of early diagenesis: Application to redox cycling in coastal marine sediments', *Geochimica et Cosmochimica Acta*, 60(16), pp. 2993–3014. Available at: https://doi.org/10.1016/0016-7037(96)00140-8.

Weiss, R.F. (1970) 'The solubility of nitrogen, oxygen and argon in water and seawater', *Deep Sea Research and Oceanographic Abstracts*, 17(4), pp. 721–735. Available at: https://doi.org/10.1016/0011-7471(70)90037-9.

West, A.J. (2012) 'Thickness of the chemical weathering zone and implications for erosional and climatic drivers of weathering and for carbon-cycle feedbacks', *Geology*, 40(9), pp. 811–814. Available at: https://doi.org/10.1130/G33041.1.

Zhao, M. *et al.* (2020) 'The role of calcium in regulating marine phosphorus burial and atmospheric oxygenation', *Nature Communications*, 11(1), p. 2232. Available at: https://doi.org/10.1038/s41467-020-15673-3.

Zhao, M. *et al.* (2023) 'Oxygenation of the Earth aided by mineral–organic carbon preservation', *Nature Geoscience*, 16(3), pp. 262–267. Available at: https://doi.org/10.1038/s41561-023-01133-2.